***Projektarbeit***

*ILR-RSN PA 11-01*

# *Development of deployable structures and mechanism for a faster passive deorbiting of satellites using drag sails*

**Florian Prochnow**

**Betreuer:**

**Dr.-Ing. Patric Seefeldt, Institut für Raumfahrtsysteme, DLR**

**Dr.-Ing. Tino Schmiel, Institut für Luft- und Raumfahrttechnik, TU Dresden**

April 2019

# Aufgabenstellung

Topic:

“Development of deployable structures and mechanism for a faster passive de-orbiting of satellites using drag sails”

Goal description:

Drag sails are devices that increase the drag area of satellite at its end of life in order to reduce the de-orbit time. This shall prevent that non-functional satellites stay in orbit for a long time as space debris that has a potential risk of colliding with operational space crafts. Developments of drag sails were investigated in several precursor projects at DLR. The latest development was carried out within the ESA-Project ADEO. This development left several open questions regarding a suitable deployment strategy for the sail membrane including mechanisms.

The goal of this work is to provide a sail membrane and deployment mechanism design that can be integrated in the ADEO subsystem. In particular, this requires an adaptation of the deployment strategy, membrane material selection as well as design and sizing of the membrane and its corresponding deployment mechanism.

Individual tasks:

- Prepare a state of the art review including a description of the ADEO1 design (precursor project that defines the baseline design for the current development).
- Describe the theoretic principle on which drag sails are based.
- Selection of membrane material under consideration of the space environment.
- Design and sizing of drag sail membrane including a possible stowing concept based on folding and coiling of the membrane.
- Design and sizing of the corresponding spool mechanism for the stowing and deployment of the membrane.
- Prepare a conclusion and outlook for future work.

# Selbständigkeitserklärung

Hiermit erkläre ich, dass ich die von mir dem Institut für Luft- und Raumfahrttechnik der Fakultät Maschinenwesen eingereichte Projektarbeit zum Thema „Development of deployable structures and mechanism for a faster passive deorbiting of satellites using drag sails“ selbständig verfasst und keine anderen als die angegebenen Quellen und Hilfsmittel benutzt sowie Zitate kenntlich gemacht habe.

Datum: _____ Unterschrift: _____

# Table of Contents

# List of Acronyms

| | |
|---|---|
| LEO | Low Earth orbit |
| ADEO | Architectural Design and Testing of a De-Orbiting Subsystem |
| CFRP | Carbon fiber reinforced polymer |
| S/C | Space craft |
| ATOX | Atomic oxygen |
| VUV | Vacuum ultra violet |
| ESA | European Space Agency |
| ADR | Active Debris Removal |
| ISS | International Space Station |
| CoM | Centre of mass |
| CoA | Centre of area |
| FEP | Fluorinated ethylene propylene |
| PFM | Preliminary flight model |
| AIV | Assembly, integration and verification |
| AIT | Assembly, integration and testing |
| MGSE | Mechanical ground support system |
| TRL | Technology readiness level |

# List of Symbols

Latin symbols

| symbol | unit | description |
|---|---|---|
| $a_i$ | $[-]$ | Fixed factor of the power function (variable unit) |
| $A$ | $[\mathrm{m}^2]$ | Surface area of the sail |
| $A_{average}$ | $[\mathrm{m}^2]$ | Average sail surface area |
| $A_B$ | $[\mathrm{m}^2]$ | Area between booms |
| $A_i$ | $[\mathrm{m}^2]$ | Effective surface area of each sail segment |
| $A_{norm}$ | $[\mathrm{m}^2]$ | Total surface area of each sail segment |
| $b_i$ | [1] | Fixed factor of the power function |
| $c$ | $\left[\frac{\mathrm{m}}{\mathrm{s}}\right]$ | Speed of light |
| $C_i$ | $[-]$ | Fix value (sum of several constants; variable unit) |
| $C_D$ | [1] | Drag coefficient |
| $d$ | [m] | Inner spool diameter |
| $d_0$ | [m] | Diameter without any thermal influence |
| $d_A$ | [m] | Axis diameter |
| $d_{B,a}$ | [m] | Outer diameter of the journal bearing |
| $d_{B,i}$ | [m] | Inner diameter of the journal bearing |
| $d_S$ | [m] | Spool sliding surface diameter |
| $d_{SH}$ | [m] | Inner diameter of the spring holder |
| $d_{So}$ | [m] | Outer diameter of the socket |
| $d_{+/-}$ | [m] | Diameter with thermal influence |
| $D$ | [m] | Outer spool diameter |
| $D_{measured}$ | [m] | Measured outer spool diameter |

| | | |
|---|---|---|
| $E$ | [Pa] | Young's modulus of copper-beryllium |
| $E_K$ | $\left[\frac{\mathrm{cm}^3}{\mathrm{atom}}\right]$ | Erosion yield of Kapton |
| $E_P$ | [J] | Potential orbital energy |
| $f$ | [1] | Correlation factor due to the atmospherically speed |
| $F$ | [1] | Filling factor |
| $F_a$ | [N] | Aerodynamic drag force |
| $F_{a,i}$ | [N] | Aerodynamic force caused by each sail segment |
| $F_{ATOX}$ | $\left[\frac{\mathrm{atom}}{\mathrm{cm}^2 \cdot \mathrm{s}}\right]$ | Atomic oxygen flux |
| $F_{d,max}$ | [N] | Maximum deployment force at the brake |
| $F_{e,s_c,1}$ | [1] | View factor hot case |
| $F_{e,s_c,2}$ | [1] | View factor cold case |
| $F_{max}$ | [N] | Maximum brake bending force |
| $F_{measured}$ | [N] | Measured coiling force during coiling tests |
| $F_{min}$ | [N] | Minimum brake bending force |
| $F_{s,i}$ | [N] | Solar pressure force caused by each sail segment |
| $G$ | $\left[\frac{\mathrm{m}^3}{\mathrm{s}^2\mathrm{kg}}\right]$ | Gravitational constant |
| $h$ | [m] | Orbital altitude |
| $i$ | [°] | Orbital inclination |
| $I_y$ | [$\mathrm{m}^4$] | Moment of inertia of the spring |
| $j$ | [m] | Clearance |
| $k$ | [m] | Folding width |
| $l_{A1}$ | [m] | Axis length |
| $l_{A2}$ | [m] | Thickness of the axis crank |
| $l_B$ | [m] | Boom deployment length |

| | | |
|---|---|---|
| $l_{Be}$ | [m] | Thickness of the bearing crank |
| $l_{blue}; l_{red}$ | [m] | Total vertical boom-membrane interface lengths |
| $l_{blue,i}; l_{red,i}$ | [m] | Divided vertical boom-membrane interface lengths |
| $l_{Bo}$ | [m] | Boom length |
| $l_e$ | [m] | Erosion length |
| $l_i$ | [m] | Lever between the CoM of the satellite and the CoA of each sail segment |
| $l_{real}$ | [m] | Real interface length |
| $l_{req}$ | [m] | Required interface length |
| $l_S$ | [m] | Spool length |
| $l_{SH}$ | [m] | Distance between the outer spring edge and the central axis of the Membrane spool |
| $l_{So,1}$ | [m] | Socked drilling hole depth |
| $l_{So,2}$ | [m] | Socked length |
| $l_{Sp}$ | [m] | Spring length |
| $l_{Spr}$ | [m] | Spring length (bending length) |
| $l_{total}$ | [m] | Total length of the membrane spool assembly |
| $m$ | [kg] | Mass of the satellite |
| $M$ | [kg] | Mass of the Earth |
| $M_{b,max}$ | [Nm] | Maximum bending moment |
| $n_s$ | [1] | Number of springs |
| $n_z$ | [1] | Number of gear teeth's |
| $p_G$ | [m] | Circular pitch |
| $P_A$ | $\left[\frac{\mathrm{W}}{\mathrm{m}^2}\right]$ | Earth's albedo |
| $P_{IR}$ | $\left[\frac{\mathrm{W}}{\mathrm{m}^2}\right]$ | Infra-red emission caused by the Earth |
| $P_S$ | $\left[\frac{\mathrm{W}}{\mathrm{m}^2}\right]$ | Solar constant (near Earth region) |

| | | |
|---|---|---|
| $r$ | [m] | Orbital radius |
| $r_0$ | [m] | Orbital radius at the beginning of the deorbit process (during ADEO deployment) |
| $r_a$ | [m] | Radius of the apogee |
| $r_i$ | [m] | Inner spool radius |
| $r_P$ | [m] | Radius of the perigee |
| $R$ | [m] | Gear outer radius |
| $R_{min}$ | [m] | Effective gear radius at minimum brake bending force |
| $R_{p0,2}$ | [Pa] | Yield strength |
| $R_{Sp}$ | [m] | Spool radius |
| $q$ | [1] | Reflectance factor |
| $s$ | [m] | Sail segment height |
| $S_F$ | [1] | Safety factor |
| $t$ | [s] | Time |
| $t_{DO}$ | [s] | Mission time for the deorbit process |
| $t_{foil}$ | [m] | Thickness of the sail membrane |
| $t_s$ | [m] | Spring thickness |
| $T_0$ | [K] | Temperature of the cosmological radiation |
| $T_a$ | [Nm] | Aerodynamic torque |
| $T_{b,max}$ | [Nm] | Maximum brake bending torque |
| $T_{b,min}$ | [Nm] | Minimum brake bending torque |
| $T_{coil}$ | [Nm] | Measured coil torque |
| $T_E$ | [K] | Earth's surface temperature |
| $T_{max}$ | [K] | Maximum sail temperature |
| $T_{min}$ | [K] | Minimum sail temperature |

| | | |
|---|---|---|
| $T_s$ | [Nm] | Solar pressure torque |
| $\Delta T$ | [K] | Temperature change |
| $\Delta T^+$ | [K] | Positive temperature change |
| $\Delta T^-$ | [K] | Negative temperature change |
| $u_{max}$ | [m] | Maximum arc length |
| $u_{min}$ | [m] | Minimum arc length |
| $v$ | $\left[\frac{\mathrm{m}}{\mathrm{s}}\right]$ | Orbital velocity |
| $v_{eff}$ | $\left[\frac{\mathrm{m}}{\mathrm{s}}\right]$ | Effective velocity |
| $V_{material}$ | [$\mathrm{m}^3$] | Volume of one sail segment material |
| $V_{measured}$ | [$\mathrm{m}^3$] | Packaging volume based on the measured outer spool diameter |
| $w_s$ | [m] | Spring width |
| $W_{by}$ | [$\mathrm{m}^3$] | Modulus of resistance against bending |
| $W_{max}$ | [m] | Maximum deformation path |
| $W_{min}$ | [m] | Minimum deformation path |
| $x$ | [m] | Distance of the inner sail tip to the CoM of the satellite |
| $y$ | [m] | Interface slack span |
| $\Delta z$ | [m] | Gear engaging depth |
| $\Delta z_{1,min}$ | [m] | Gear engaging depth at minimum brake bending force |

Greek symbols

| symbol | unit | description |
|---|---|---|
| $\alpha$ | [°] | Pitch angle of the sail segment |
| $\alpha_{max}$ | [°] | Maximum bending angle |
| $\alpha_{min}$ | [°] | Minimum bending angle |
| $\alpha_S$ | [1] | Adsorption coefficient of the sail |
| $\alpha_T$ | $\left[\frac{1}{\mathrm{K}}\right]$ | Thermal expansion coefficient |
| $\beta$ | [°] | Angle between the longitudinal axis of the satellite and the solar radiation direction |
| $\gamma$ | [°] | Deployment angle |
| $\delta$ | [°] | Deployment angle |
| $\varepsilon$ | [1] | Emission coefficient of the sail |
| $\eta$ | [1] | Efficiency of the used area between the booms for generating a drag force |
| $\mu$ | $\left[\frac{\mathrm{m}^3}{\mathrm{s}^2}\right]$ | Gravitational parameter of the Earth |
| $\rho$ | $\left[\frac{\mathrm{kg}}{\mathrm{m}^3}\right]$ | Density of the atmosphere |
| $\sigma$ | $\left[\frac{\mathrm{W}}{\mathrm{m}^2\mathrm{K}^4}\right]$ | Boltzmann constant |
| $\sigma_{b,max}$ | [Pa] | Bending stress |
| $\tau$ | [1] | Correlation coefficient of the power function regression |
| $\varphi$ | [°] | Angle between velocity vector and longitudinal axis of the satellite |
| $\omega_e$ | $\left[\frac{\mathrm{rad}}{\mathrm{s}}\right]$ | Angular velocity of the Earth |

# 1 Introduction

Space travel becomes more and more important in today's world. The number of lunches and satellites which are flying around the Earth is as high as never before. As shown in [1], there are about 5450 rocket launches (including failures) which were starting since the year 1957. Thereby, about 8950 satellites were launched in an Earth orbit. About 5000 of them are still in space while just 1950 satellites are functioning. This causes problems in highly frequented orbits. The rising amount of space debris is one of these difficulties. According to the European Space Agency (ESA) [1], the estimated number of space debris are 128 million objects from 1 mm to 1 cm, 900000 objects from 1 cm to 10 cm and 34000 objects greater than 10 cm.

Such debris consists of manmade objects like upper stages of rockets, debris from satellite collisions and old/non-used satellites. The high amount of space debris causes a "snowball effect" also called Kessler syndrome. The collision of space debris parts causes more smaller parts which would rise the amount of space debris. There is a critical point at which the rising number of space debris, only caused by random collisions, is equal to the number of parts which have a reentry. This border line was overshoot in the past. Therefore, the current number of space debris would rise even without launching additional spacecrafts.

One of the main goals for the whole space community is to stop the rising numbers of space debris and to make the future spaceflight safer. There are many ideas how to avoid and reduce space debris. In this work, a drag sail as passive de-orbiting device developed in the ADEO (Architectural Design and Testing of a De-Orbiting Subsystem) project is discussed. In particular, the main themes of this topic are the design and sizing of the membrane (Section 6) and membrane spool (Section 0) of the ADEO-2 project including the stowing and deployment strategy (Section 5). Additionally, the basic principle of a drag sail in a low Earth orbit (LEO) (Section 3) as well as the selection of the membrane materials (Section 4) will be discussed.

Drag sails, like the ADEO subsystem, consists of a light weight sail and deployment structures mounted on the satellite. It will be deployed at the end of life of the satellite. The deployed sail increases the total area of the satellite which causes a higher drag resistance in the residual atmosphere.

The main goals of drag sails are to decrease the altitude and reduce the deorbit time of the satellite. Because of the decreasing deorbit time of non-used or damaged satellites, the number of big space debris parts flying in a low Earth orbit will be reduced. Furthermore, drag sails are a passive deorbit device. After its deployment, the drag sail stays in the deployed position for the rest of the deorbit time. This device should replace heavy and expensive active deorbit solutions like thrusters. Without requiring extra fuel or attitude control, the effort and energy during the lifetime of the satellite will be reduced. To make drag sails more attractive they should cost and weight less than other passive or active deorbit devices.

# 2 State of the art review including the ADEO-1 design

The idea of using drag sails as a low weight deorbit device is investigated in various projects around the world. The ESA established the Active Debris Removal (ADR) project in which technologies are invented to reduce the amount of space debris. One subproject is RemoveDEBRIS. This mission consists of a technology which uses a deploy structure launched from the International Space Station (ISS). This structure made several tests and experiments concerning the capturing of space debris. The Surrey Space Centre (UK) develops a drag sail which is used for this mission. [2]

Other missions are originally based on solar sailing in LEO like some CubeSail missions. A nano-solar sail cube satellite, developed by Surrey Space Centre, is used to demonstrate solar sailing in LEO with an inclination change. After the satellite's lifetime, this solar sail shall be used as a drag sail for a faster deorbit. [3]

Additional solar sails deployment demonstrators are the Nano Sail D and D 2 missions. According to [4], Nano Sail D was not successful due to a failed launch of a Falcon 1 rocket. Another solar sail demonstrator is the LightSail founded by the Planetary Society [5].

Solar sail technologies were developed by the DLR since the 1990´s. This resulted in the Gossamer-1 protect perused from 2012 to 2016 [6]. Based on the Gossamer-1 project knowledge, the Deployable Membrane project was made which also investigated drag sails.

The generated information from both projects was used in the ADEO-1 project. This project was invented to make a first design of a drag sail which was used as a breadboard design for testing these innovations. The stowed version of ADEO-1 looks like a cuboid which is mounted behind the satellite in reference to the fight direction. "As a reference mission a satellite with a mass of around 1000 kg at a 650 km mean orbital altitude corresponding to period ~98 minutes with an eccentricity smaller then 0.01 was considered" [7, p. 3]. These values are related to the main requirement which is to deorbit the satellite within 25 years.

The subsystem consists of four booms, presented in Figure 1, which are located at the corners of the cuboid. These structures have a double Ω-shape for stability reasons and are made of carbon fiber reinforced polymer (CFRP) [7].

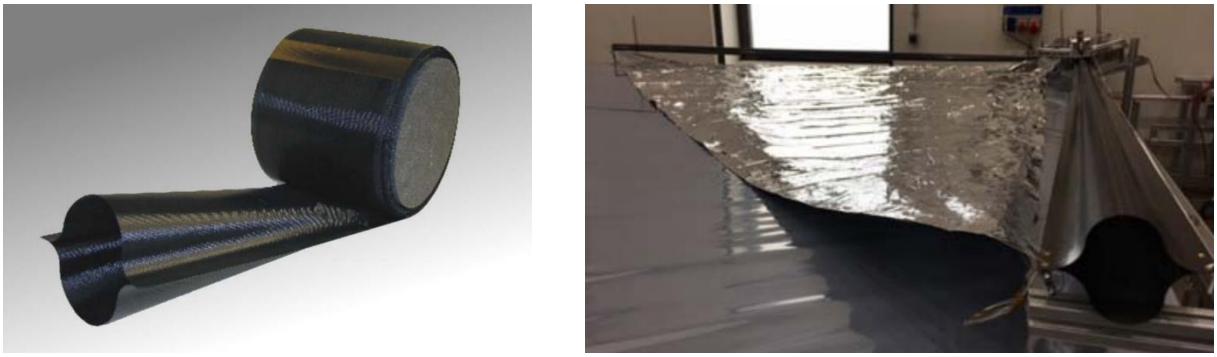

Figure 1: Partially deployed boom (left, [7, p. 6]) and deployed boom with one sail segment (right, [8, p. 5]).

Each boom is coiled on its own boom spool in the stowed configuration. In the middle of the edges, between the booms, four membrane spools are mounted horizontally on the bottom plate of the ADEO-1 subsystem shown in Figure 2. Each of them holds a membrane segment which was zig-zig folded before rolling it on the spool.

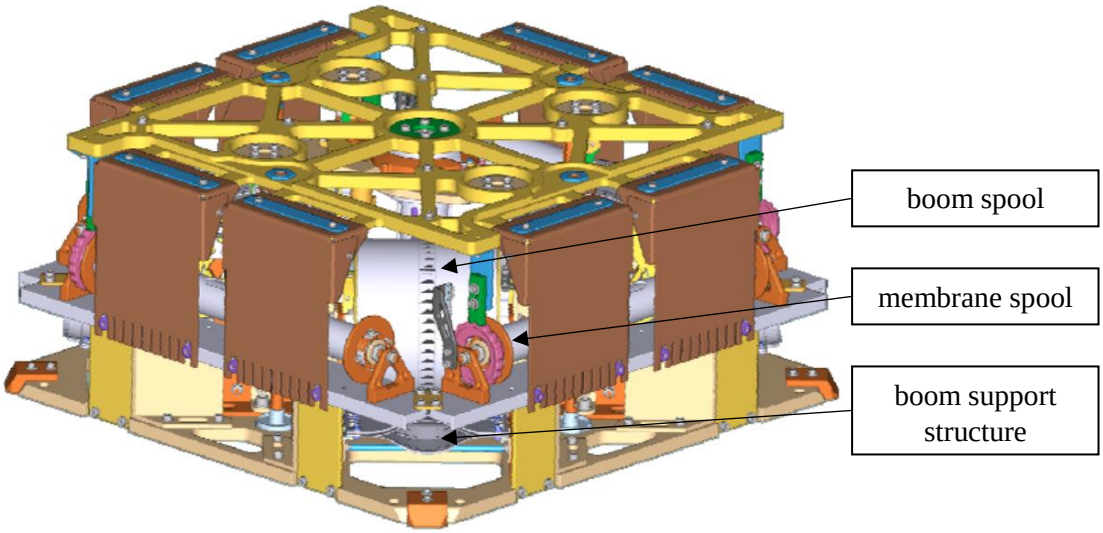


Figure 2: ADEO-1 subsystem without cover [7, p. 4].

As a result, four membrane segments with a triangle shape were used to generate the drag sail area. The boom spools are driven by a motor which produces the deployment force. The membrane segments are connected to the boom via a cable interface. Thereby, the boom is pulling out the membrane during the deployment. All deploy structures (booms and membrane segments) are angled at the ADEO-1 configuration. This results in a pyramidal shape of the deployed subsystem which is shown in Figure 3.

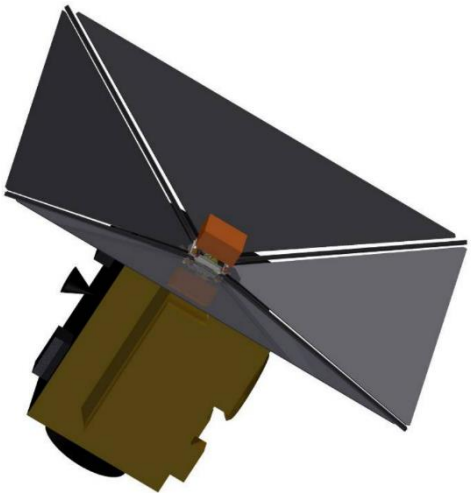

Figure 3: Pyramidal shape design of the ADEO-1 drag sail mounted on the back of a satellite [7, p. 3].

The pyramidal shape design was assumed to be the best design for a better passive stabilization through the orbit decent. A detailed investigation of it can be found in the Section 3.2.

At the end of the satellite lifetime, which is assumed to be 15 years after launch, a hold down and release mechanism will lift a cover, which protects the inner structure of the ADEO-1 subsystem, in front of the boom and membrane spool. The motor will be activated. Thereby, the boom and the membrane will be pulled off the spools like described above.

After the deployment is done, this configuration will not be changed during the deorbit time. Therefore, the membrane, booms and other deployment structures must withstand the LEO space environment from at least a storage time of 15 years and 25 years deployed during the deorbit. The biggest difficulties during the deorbit time are the resistance against atomic oxygen (ATOX), the vacuum ultra violet (VUV) radiation and the amount of the thermal cycles as well as thermal differences between these cycles.

For the membrane, “Upilex S, a 12.5 µm thick Polyimide film, coated with 500 nm aluminum is evaluated as the most suitable Material to withstand the 15 years storage and 25 years deployed in orbit” [7, p. 6]. Because of the restriction that a standardized product needs to be used, the aluminum layer was set to 100 nm. This combination of materials should withstand long enough in this harsh environment. Most of the deployment mechanism, like spools, are made of aluminum.

Various tests with the ADEO-1 breadboard design were made. For example, a deployment test of one sail segment, a partially deployment in vacuum under LEO environmental conditions and vibration tests. These tests and their results are not part of this work and will be not further investigated.

In the ADEO-2 project the drag sail design is further developed. Nevertheless, various changes were made. There will be just one boom spool in the middle of the subsystem. In the first view seconds of the deployment of the ADEO-1 subsystem, the boom - sail interface angle is extremely high compared to the deployment orientation. Therefore, the loads are very high at the beginning of the deployment. To reduce this angle and with that the deployment forces at the beginning, the rotation (longitudinal) axis of the membrane spools and the boom spool are now orientated vertical regarding the ADEO subsystem.

Additionally, the angle of the deployed structures (membrane and boom) is set to 0°. Therefore, the drag area is rectangular to the flight direction if no tumbling of the satellite is considered.

# 3 Basic principles of drag sail

Drag sails like ADEO are used to increase the drag area of the satellite. Thereby, the potential energy of the spacecraft and the deorbit time are decreasing. For ADEO-2 more precise assumptions concerning the altitude and mass of the satellite were made. The altitude should be between 400 km and 750 km with a satellite mass of about 500 kg. The sail surface area should be about 25 $m^2$. With these values the deorbit time is estimated in Section 3.1.

Additionally, for a passive stabilization it is possible that the sail segments have a pitch angle to the flight direction. The limitations of such passive stabilization are analyzed in Section 3.2.

## 3.1 Deorbiting time calculation

In this section the deorbit time of the satellite including the ADEO-2 subsystem will be determined. At first the potential orbital energy of the satellite must be known, it is

$$E_P = -G \cdot \frac{M \cdot m}{r_A + r_P} \quad . \tag{1}$$

Here, $G$ is the gravitational constant, $M$ is the mass of the Earth, $m$ the mass of the satellite (500 kg) and $r_A/r_P$ is the radius of the apogee/perigee. To simplify the energy equation the gravitational parameter of the Earth can be added. Additionally, it can be assumed that the orbit is nearly circular. Therefore, the radius of the apogee/perigee can be replaced with the radius of the circular orbit as

$$\mu = G \cdot M \quad , \tag{2}$$

$$E = -\mu \cdot \frac{m}{2r} \quad . \tag{3}$$

According to [9, p. 150], the power equation is achieved by time derivation of the energy as

$$\frac{dE}{dt} = -\mu \cdot m \cdot \frac{d\left(\frac{1}{2r}\right)}{dt} = \frac{\mu \cdot m}{2r^2} \cdot \frac{dr}{dt} \quad . \tag{4}$$

The influence of the atmospheric drag force is considered as energy dissipation. The force is multiplied with the relative velocity of the space craft (S/C) to the atmosphere. Therefore, the energy change due to the drag force is

$$\frac{dE}{dt} = F_a \cdot v_{eff} \quad \text{with } v_{eff} = v \cdot f \quad . \tag{5}$$

As shown in [10, p. 353], $F_a$ is the drag force which influences the satellites orbit and can be described by

$$F_a = \frac{1}{2} \cdot C_D \cdot \rho \cdot A \cdot {v_{eff}}^2 \quad . \tag{6}$$

In this calculation, only the atmospherically influence of the deorbit time will be studied. The drag coefficient $C_D$ is between 2 and 2.5 for a plate [10, p. 353]. Here this factor is set to 2.2. $A$ is the surface area of the sail. It is assumed that the sail flat. According to the ADEO design, $A$ is set to 25 $m^2$. An average surface area during tumbling of the satellite for the planar and pyramidal shape design is not investigated in this calculation. This average drag area would make the deorbit calculation more precise and should be considered in the next design phases. The density of the atmosphere $\rho$ and the effective velocity $v_{eff}$ depend on the altitude. Here the correlation factor $f$ stands for the difference between the orbital velocity and the atmospherically speed. This factor influences the drag force and thereby the deorbit time. Considering an atmosphere that rotates with the Earth shown in [9, p. 150], $f$ is calculated as

$$f = 1 - \frac{\omega_e \cdot r_p}{v_p} \cdot \cos(i) \quad . \tag{7}$$

The angular velocity of the Earth $\omega_e$ is $7.292 \cdot 10^{-5}$ rad/s [9, p. 150]. Additionally, the factor depends on the orbit radius at the perigee $r_p$ and the orbit inclination $i$. $v_p$ is the velocity of the satellite on the perigee. The orbital velocity can be determined with the vis visa equation for a circular orbit which is

$$v = \sqrt{\frac{\mu}{r}} \quad . \tag{8}$$

The Earth radius is set to 6378.136 km (equatorial radius; [11, p. 107]). The gravitational parameter of the Earth $\mu$ is $3.986 \cdot 10^{14} \left[\frac{m^3}{s^2}\right]$ [12, p. 83]. With the vis visa equation for a circular orbit the factor $f$ can be calculated as

$$f = 1 - \frac{\omega_e \cdot r^{\frac{3}{2}}}{\sqrt{\mu}} \cdot \cos(i) \quad . \tag{9}$$

Table 1 provides some solutions for $f$. It can be seen that $f$ does not change that much in different altitudes in LEO. The inclination has a huge influence on the factor $f$. An orbit inclination of 0° means that the satellite is fling in the same direction as the atmosphere. Thereby, the spacecraft will decrease its altitude not so fast compared to an inclination of 180° (a retrograde orbit) where the satellite is fling against the atmospheric speed. $f$ will not influence the drag force when the inclination is 90° (polar orbit).

Table 1: Factor $f$ with different orbit radii and inclinations

| Orbital radius [km] | $f$ with $i = 0°$ | $f$ with $i = 90°$ | $f$ with $i = 180°$ |
|---|---|---|---|
| 7128.136 | 0.927631 | 1 | 1.07237 |
| 6878.136 | 0.931405 | 1 | 1.0686 |
| 6628.136 | 0.93511 | 1 | 1.06489 |

To investigate the worst case, the inclination is set to 0°. In order to avoid numeric simulations, $f$ is calculated at an average factor between the altitude of 200 km and 750 km as

(10)

$$f \approx \frac{1}{\Delta r} \cdot \int_{6578.136\,\mathrm{km}}^{7128.136\,\mathrm{km}} \left(1 - \frac{\omega_e \cdot r^{\frac{3}{2}}}{\sqrt{\mu}}\right) = 0.934461 \quad .$$

Applying the velocity on Equation (5) and using Equation (4) leads to

$$\frac{\mu \cdot m}{2r^2} \cdot \frac{dr}{dt} = \frac{1}{2} \cdot f^3 \cdot A \cdot \left(\frac{\mu}{r}\right)^{\frac{3}{2}} \cdot C_D \cdot \rho(h) \tag{11}$$

and further simplified to

$$m \cdot \frac{dr}{\sqrt{r}} = f^3 \cdot A \cdot \sqrt{\mu} \cdot C_D \cdot \rho(h) \cdot dt \quad . \tag{12}$$

To decrease the calculation effort, a Taylor series is made for the section $\frac{1}{\sqrt{r}}$ which is

$$\frac{1}{\sqrt{r}} \approx \frac{1}{\sqrt{r_0}} - \frac{1}{2} \cdot \frac{1}{r_0^{\frac{3}{2}}} \cdot (r - r_0) \text{ with } (r - r_0) = \Delta r \quad . \tag{13}$$

The parameter $r_0$ is the orbital radius of the satellite at the beginning of the deorbit ($t$ = 0 s). Because this calculation is just a rough assumption, the series is stopped after the second term. After putting the Taylor series into the differential equation and simplifying the $dr$ into $\Delta r$, Equation (12) is transformed to

$$m\left(\frac{\Delta r}{\sqrt{r_0}} - \frac{1}{2} \cdot \frac{1}{r_0^{\frac{3}{2}}} \cdot \Delta r^2\right) = f^3 \cdot A \cdot \sqrt{\mu} \cdot C_D \cdot \rho(h) \cdot dt \quad . \tag{14}$$

To simplify the left equation side, it is assumed that

$$\frac{\Delta r}{\sqrt{r_0}} \gg \frac{\Delta r^2}{r_0^{\frac{3}{2}}} \quad . \tag{15}$$

Therefore, the left side is abridged to

$$m \cdot \frac{\Delta r}{\sqrt{r_0}} = f^3 \cdot A \cdot \sqrt{\mu} \cdot C_D \cdot \rho(h) \cdot dt \tag{16}$$

For the density, a regression analysis with a power function is made. The used values for the regression are between 200 km and 760 km altitude (in 20 km steps) and with a low solar activity [11, pp. 138-139]. The values from [11, pp. 138-139] are shown in Table 8 in the appendix. The low solar activity is

used because the density of the atmosphere is extremely changing through the solar cycle. It will be the worst-case scenario for the drag force and the deorbit time. The used power function for the density is

$$\rho = a_i \cdot h^{b_i} \tag{17}$$

where $a_i$ and $b_i$ are the fixed factors and $h$ the altitude. The solution of the regression is

$$a_1 = 5.296659566 \cdot 10^9 \left[\frac{\text{kg} \cdot \text{km}^{8.4839}}{\text{m}^3}\right] \ ,$$

$$b_1 = -8.4839 \ .$$

The inaccuracies of the result for the power function for the low solar activity is very small which is shown by the correlation coefficient which is

$$|\tau| = 0.998367 \ .$$

Considering that the radius and the altitude depending on each other with

$$h = r - r_E \tag{18}$$

as well as using Equation (17) and changing $\Delta r$ to $dr$ (infinite small deorbit steps), Equation (16) can be transformed to

$$\frac{dr}{(r - r_E)^{b_i}} = \frac{\sqrt{r_0} \cdot f^3 \cdot A \cdot \sqrt{\mu} \cdot C_D \cdot a_i}{m} \cdot dt \ . \tag{19}$$

$r_E$ is the radius of the Earth. Furthermore, some constant parameters will be put into one factor which is named $C_i$. Thereby, the Equation (19) is written to

$$\frac{dr}{(r - r_E)^{b_i}} = C_i \cdot dt \tag{20}$$

with

$$C_i = \frac{\sqrt{r_0} \cdot f^3 \cdot A \cdot \sqrt{\mu} \cdot C_D \cdot a_i}{m} \ . \tag{21}$$

This equation can be solved through integration as

$$\int_{r_0 - \Delta r}^{r_0} \frac{dr}{(r - r_E)^{b_i}} = C_i \cdot \int_0^t dt \ \Leftrightarrow \ \frac{(r_0 - r_E)^{1-b_i}}{1 - b_i} - \frac{(r_0 - \Delta r - r_E)^{1-b_i}}{1 - b_i} = C_i \cdot t \ . \tag{22}$$

The $\Delta r$ is the altitude change during the deorbit. Replacing the radii with the expression for the altitude from Equation (18) and transform it provides an analytical solution for the orbital altitude as function of time as

$$h(t) = \left({h_0}^{1-b_i} - C_i \cdot (1 - b_i) \cdot t\right)^{\frac{1}{1-b_i}} \quad . \tag{23}$$

To calculate the deorbit time, the maximum altitude of 750 km is used. Regarding the low solar activity, the deorbit time is assumed to be 243.865 years.

The satellite including the ADEO-2 subsystem should deorbit within 25 years. The deorbit time of about 243.865 years completely overshoots this requirement. It must be considered that in such time duration, there will be a low as well as a medium and high solar activity. Therefore, a second calculation with a medium solar activity is made. For that another regression is necessary with the atmosphere density values of the medium solar activity [11, pp. 138-139]. Here the boundary conditions are the same. The altitude for the regression is between 200 km up to 760 km in 20 km steps. The new fixed parameters are

$$a_2 = 104605862 \left[\frac{\mathrm{kg} \cdot \mathrm{km}^{7.46247922}}{\mathrm{m}^3}\right] \quad ,$$

$$b_2 = -7.46247922 \quad .$$

With these parameters the second deorbit time calculation is made. The deorbit time for a medium solar activity is decreasing strongly to 16.012 years. This shows how important the investigation of different atmosphere densities is. Additionally, the calculations consider no tumbling of the satellite. The solar activity has a cycle of 11 years [13]. Depending on the launch date and the satellite life time after which the sail is deployed, the satellite is starting the deorbit in a low, medium or high solar activity. This extremely changes the deorbit duration in a different altitude. Figure 4 shows the deorbit process of the satellite. The satellite is slowly descending through the bigger part of its lifetime. Only in the last view months the altitude is decreasing rapidly. The main reason is the ever-increasing density of the atmosphere and with that an always increasing drag force. Because these factors are influencing each other, the deorbit process will be speeded up. The graph in Figure 4 stops shortly over 300 km altitude. This is caused by the resolution of the diagram. In this case the graph will nearly follow a vertical line, if the altitude is less than 300 km.

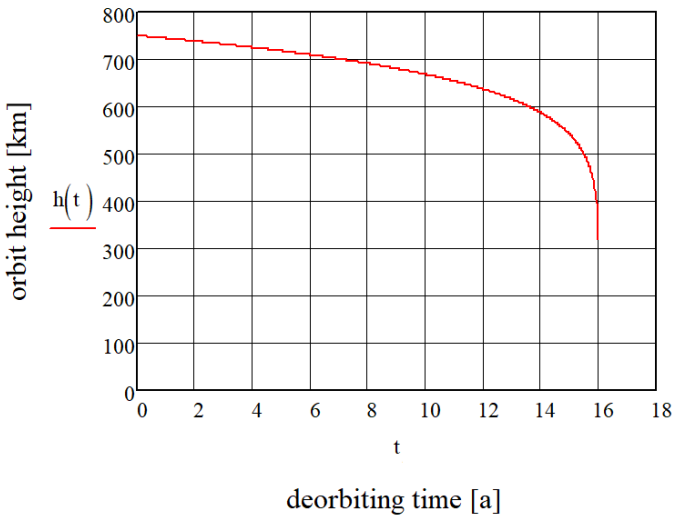


Figure 4: Altitude of the satellite compared to the deorbit duration with a medium solar activity calculated with the second method.

A satellite, without drag sail, with an average effective surface area rectangular to the flight direction of about 1.5 $m^2$, a satellite mass of 500 kg, a start altitude of 750 km and an inclination of 0° as well as a medium solar activity during the whole deorbit process would need about 267 years for the deorbit. With the consequence of a faster deorbit of bigger space debris parts like used satellites, the risk of impacts on these bigger parts as well as splintering into more smaller parts is decreasing. The total impact risk does not change that much, but the impacts on the membrane will cause no or less splintering.

## 3.2 Passive stabilization

In LEO there are different disturbance torques caused by the gravity gradient, solar radiation and magnetic field. Because of the light weight sail structure, the moment of inertia is changing only slightly during the deployment. Furthermore, no assumptions of the geometry and the mass distribution of the satellite will be made. Thereby, the disturbances produced by the gravity gradient and magnetic field are not further investigated in this work. Additionally, the very light weight sail has no big influence on the gravity gradient compared to the satellite. In this calculation all four sides of the ADEO membrane and the center of mass (CoM) of the whole satellite but not the satellite itself will be investigated. The requirement for the passive stabilized satellite using drag sails in this configuration is

$$T_{a,max} > T_{s,max} \tag{24}$$

with $T$ as the torque around the CoM of the satellite.

In Figure 5 the satellite with all four sail segments is shown. Each sail segment got its own number which will be used for the further calculations. If the satellite is not pointing towards the flight direction, the effective areas of the sail segments are differently changing. These areas are calculated to determine the drag force of each sail segment.

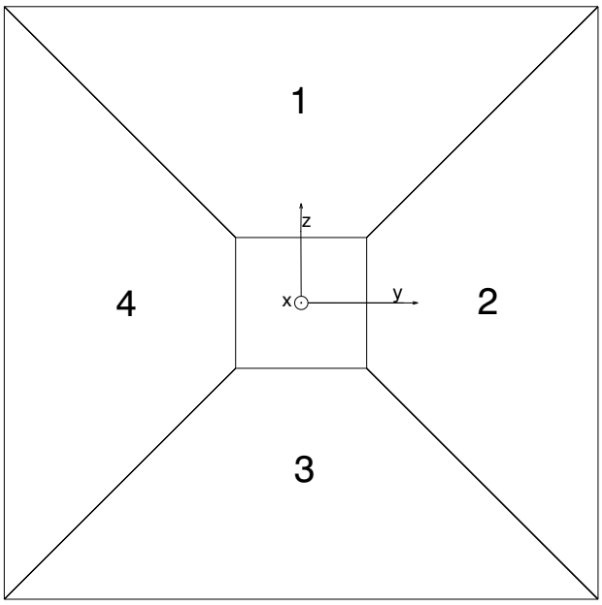


Figure 5: Front view of the satellite including the ADEO subsystem. The numbers show the indices of the sail segments as well as the forces, surface area, levers and torques.

First, the aerodynamic influence will be discussed. In this consideration only one torque direction (around the Y - axis) will be investigated. The aerodynamic torque can be calculated with

$$T_a = \sum_{i=1}^{4} F_{a,i} \cdot l_i \quad . \tag{25}$$

The force $F_{a,i}$ is caused by the aerodynamic drag with the lever arms $l_i$ the force generated a moment around the CoM. Figure 6 shows the geometry values which will be necessary for the calculation of the lever arms as well as the aerodynamic and solar radiation forces. According to [10, p. 353], the aerodynamic force can be described as

$$F_{a,i} = 0.5 \cdot \rho \cdot C_D \cdot A_i \cdot v^2 \cos(\varphi \pm \alpha) \quad . \tag{26}$$

The drag coefficient $C_D$ is set to 2.2, like in the abstract 3.1. The force is always rectangular to the surface. The density of the atmosphere $\rho$ and the velocity $v$ between the satellite and the atmosphere depend on the altitude. A regression analysis for the density was made in Section 3.1 with a low solar activity. The calculated values of this power function are used in the passive stabilization. The low solar activity with less density of the atmosphere is used because of the smaller aerodynamic torque (lower righting moment) which is the worst case for the passive stability. For the velocity, the standard equation for a circular orbit is used with $f$ as an additional parameter which includes the influence of the atmosphere velocity. $f$ is calculated at an average factor shown in Equation (10). The velocity $v$ is

$$v = \sqrt{\frac{\mu}{r_E + h}} \cdot f \quad . \tag{27}$$

The radius of the Earth $r_E$ is chosen to 6378.136 km (equatorial radius; [11, p. 107]). The gravitational parameter $\mu$ is $3.986 \cdot 10^{14}$ $m^3/s^2$ [12, p. 83].

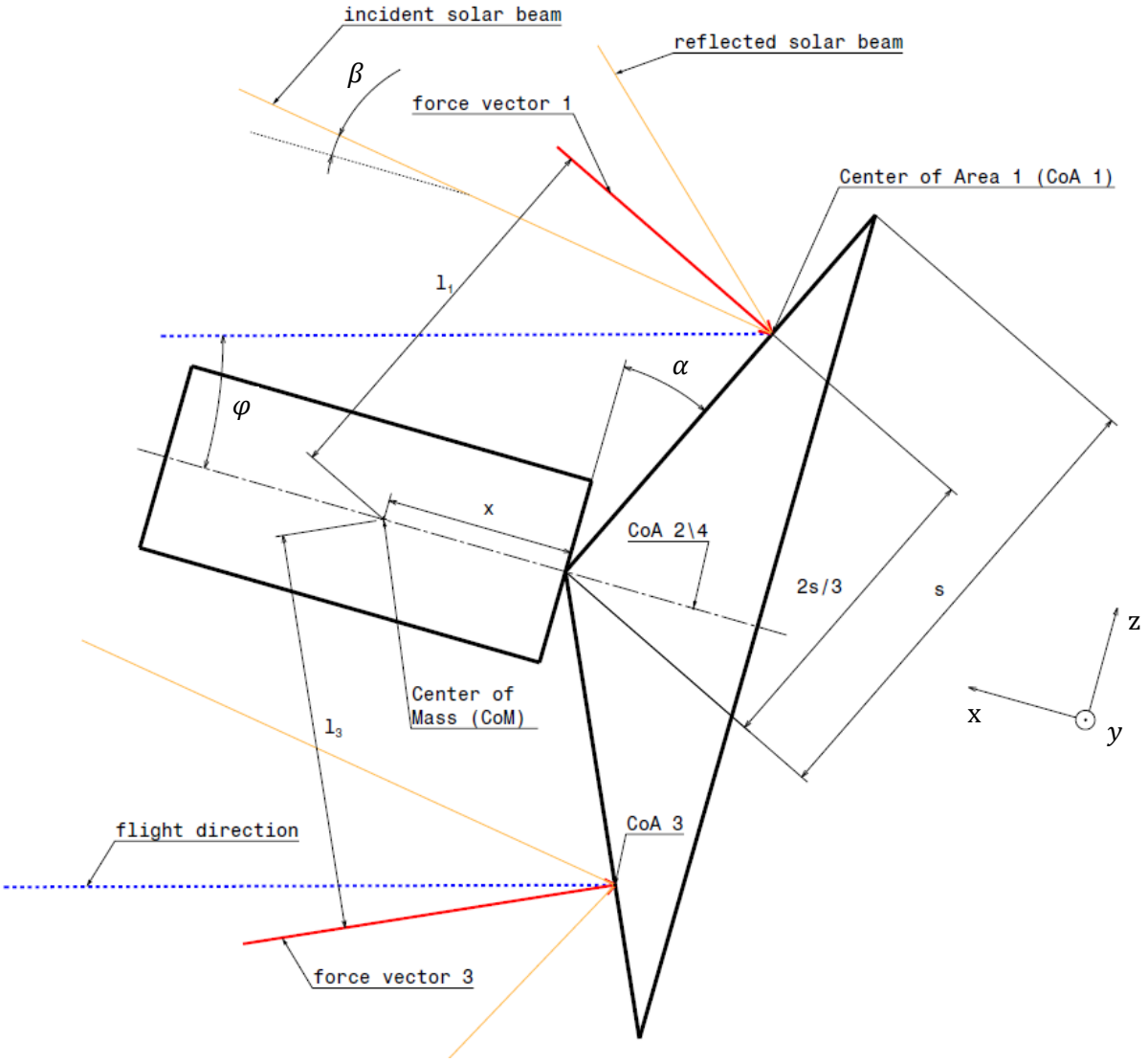


Figure 6: Satellite including the ADEO subsystem. Influence of the aerodynamic and solar disturbance.

Because of the angled membrane segments, which is shown in Figure 6, with the value of $\alpha$ and the angle between velocity vector and longitudinal axis of the satellite, $\varphi$, in ADEO-1 three of four surfaces have different effective drag areas. They can be calculated as

$$A_1 = A_{norm} \cdot \cos(\varphi + \alpha) \quad , \tag{28}$$

$$A_3 = A_{norm} \cdot \cos(\varphi - \alpha) \quad , \tag{29}$$

$$A_{2/4} = A_{norm} \cdot \cos(\varphi) \cdot \cos(\alpha) \quad . \tag{30}$$

The surface area of each segment $A_{norm}$ is 6.25 $m^2$ (25 $m^2$ in total). Both angles, $\varphi$ and $\alpha$, can affect the drag area if the areas are not fully in the aerodynamic shadow. This is considered by

$$|\varphi| + \alpha \leq 90° \text{ with } \alpha \geq 0° \quad . \tag{31}$$

Furthermore, the lever arms of all aerodynamic forces, shown in Figure 6, need to be determined:

$$l_1 = l_3 = \sin(\alpha) \cdot x + \frac{2}{3} \cdot s \quad , \tag{32}$$

$$l_2 = l_4 = 0 \text{ m (in reference to the Y} - \text{axis)} \quad . \tag{33}$$

The length $s$ is the height of one membrane segment triangle and $x$ is the distance between the center of mass and the tip of the sail "pyramid". The indices which are used in the force, area and lever calculation indicate which sail segment is investigated. The first one is the membrane segment which is "more" pointing away from the fight direction. The second and fourth indice are the segments which were symmetrical to each other regarding the $\varphi$ angle. The third one is the membrane segment with the highest effective area towards the aerodynamically drag. These assumptions were made based on a positive $\varphi$. If $\varphi$ is negative the properties of the indices 1 and 3 are changing.

All in all, the torque based on the aerodynamic is

$$T_a = F_{a,3} \cdot l_3 - F_{a,1} \cdot l_1 \quad . \tag{34}$$

Moreover, the solar pressure needs to be investigated. While the aerodynamic torques try to eliminate the difference in orientation between velocity vector and satellite longitudinal axis (X - axis), if the pitch angle $\alpha$ is not 0°, the solar pressure will try to increase the $\varphi$ angle, if the solar radiation is not parallel to the velocity vector of the satellite. The torque caused by the solar pressure can be calculated by

$$T_s = \sum_{i=1}^{4} F_{s,i} \cdot l_i \quad . \tag{35}$$

Here, $F_{s,i}$ stands for the resulting force which is caused by the solar pressure and $l_i$ are the levers between the point where the force effected the satellite and the center of mass. According to [10, p. 353], the solar pressure force is calculated by

$$F_{s,i} = \frac{P_S}{c} \cdot A_i \cdot (1 + q) \cdot \cos(\alpha \pm \beta) \quad . \tag{36}$$

$P_S$, the solar constant is set to 1366.1 W/m$^2$ [11, p. 121] and $c$ the speed of light with $2.998 \cdot 10^8$ m/s. To study the highest force (for the worst case), the reflectance factor $q$ is set to 1 (total reflection). The angle $\beta$ is positioned between the longitudinal axis of the satellite and the solar radiation direction shown in Figure 6. To investigate the highest solar radiation torques, $\beta$ changes its orientation compared to the global coordinate system depending on $\varphi$. Thereby, the solar radiation torque is independent from $\varphi$. The effective area $A_i$, which would be rectangular to the incident solar beam, of each sail segment can be calculated with

$$A_i = A_{norm} \cdot \cos(\alpha \pm \beta) \tag{37}$$

The surface area $A_{norm}$ of each sail segment is 6.25 m$^2$. The effect of the pitch angle $\alpha$ is considered in the cosines. With these values the forces can be calculated as

$$F_{s,1} = \frac{P_S}{c} \cdot A_{norm} \cdot (1+q) \cdot (\cos(\alpha - \beta))^2 \quad , \tag{38}$$

$$F_{s,3} = \frac{P_S}{c} \cdot A_{norm} \cdot (1+q) \cdot (\cos(\alpha + \beta))^2 \quad . \tag{39}$$

A positive $\beta$ will cause a higher force on sail segment one. The segments two and four will be not considered because both torques caused by these surfaces will cancel each other out. The levers of sail segment one and three are calculated by

$$l_1 = l_3 = \sin(\alpha) \cdot x + \frac{2}{3} \cdot s \quad . \tag{40}$$

All in all, the torque caused by the solar radiation is

$$T_{solar} = F_{solar,1} \cdot l_1 - F_{solar,3} \cdot l_3 \quad . \tag{41}$$

The torque caused by the solar radiation strongly depends on the illumination angle ($\alpha \pm \beta$). Seen by Equation (40), the solar force lever arms reach their maximum at $\alpha = 45°$. If this value is used, the force $F_{s,1}$ from Equation (38) would reach its maximum at $\beta = 45°$ and $F_{s,3}$ reaches its minimum. Therefore, the resulting torque has its maximum at $\beta = \alpha = 45°$ which is shown in Figure 7.

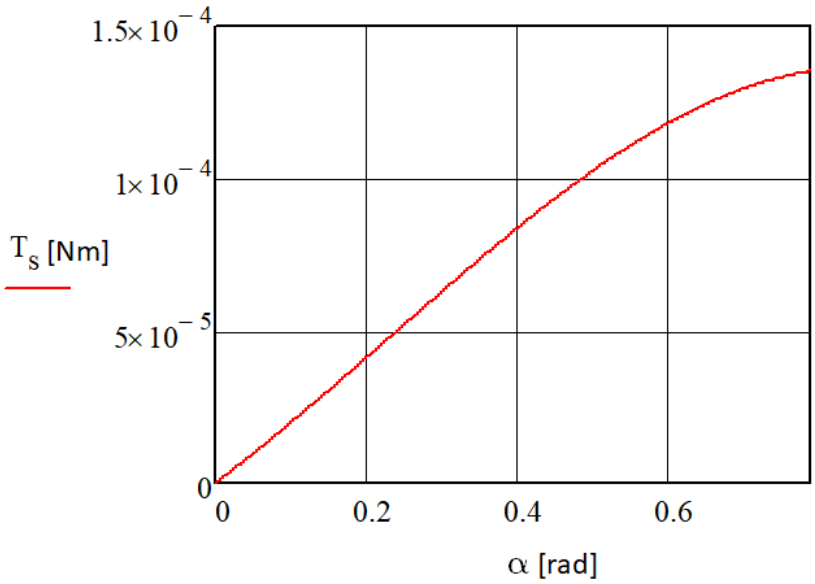


Figure 7: Solar torque over the pitch angle $\alpha$ with $\beta = 45°$.

As a result, the value of the solar radiation torque is $1.352 \cdot 10^{-4}$ Nm. With these assumptions the calculation of the aerodynamic torque is made. Because $\alpha$ was set to 45° the maximum torque for a particular $\varphi$ must be investigated. In Figure 8, the aerodynamic torque reaches its maximum at a $\varphi$ angle

of 45°. Higher $\varphi$ angles will not be studied based on the boundary conditions by Equation (31). With a higher $\varphi$ one sail side will not have influence for the aerodynamic torque anymore.

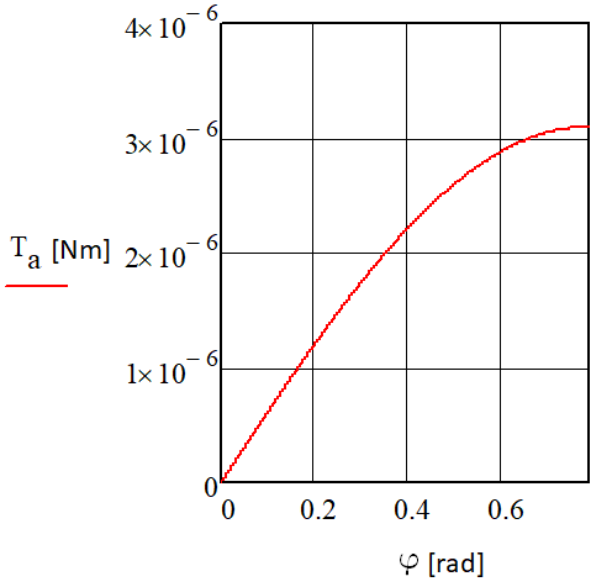


Figure 8: Aerodynamic torque over the angle $\varphi$ with $\alpha = 45°$.

With these values the aerodynamic torque only depends on the altitude. In Figure 9 is shown the influence of the altitude to the aerodynamic torque. Additionally, the given solar radiation torque is presented. $T_a$ is smaller than $T_s$ above an altitude of about 450 km with an $\alpha = \beta = \varphi = 45°$. Above 450 km the satellite would tumble due to a lack of passive stabilization torque.

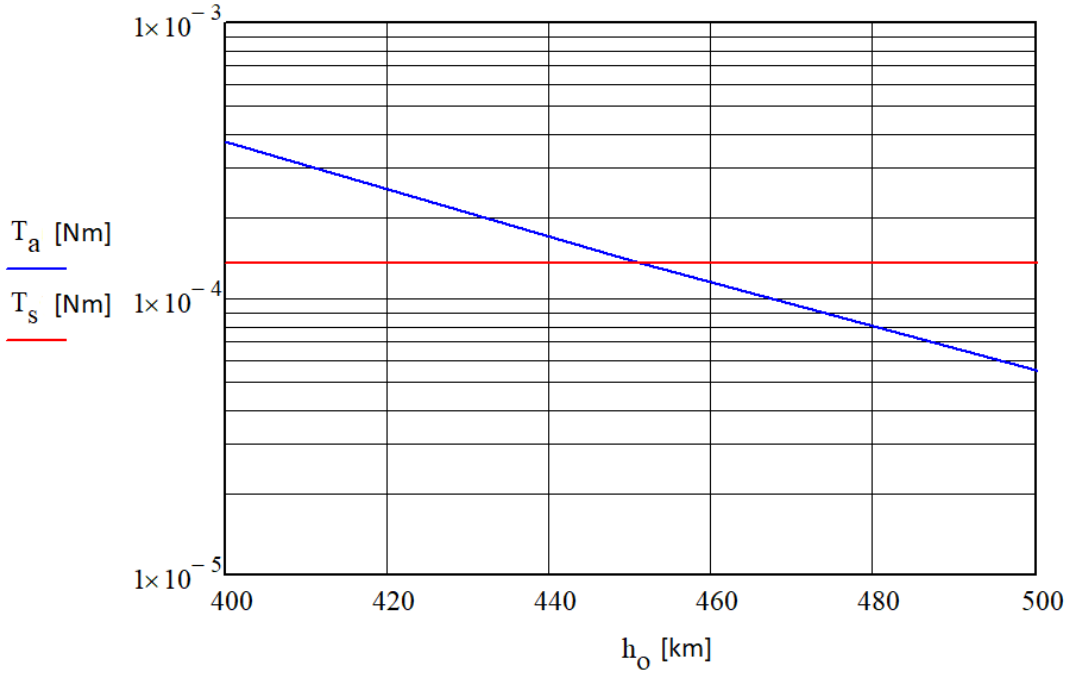


Figure 9: Aerodynamic and solar torque over the altitude.

Figure 10 shows the values of the aerodynamic and solar torque over the pitch angle at an altitude of 400 km. The torques are depending on the pitch angle but the difference between both torques is always the same caused by the identical levers from both disturbances. Additionally, the angle between the longitudinal axis of the satellite and the flight direction ($\varphi$) can be seen as a border value of 45°. With

this value a boundary condition is made which describes maximum angle which the satellite will be tumble at a given altitude. Only the altitude can be changed to reach an equal between the solar and aerodynamic torque which would describe the maximum $\varphi$ angle for this specific configuration.

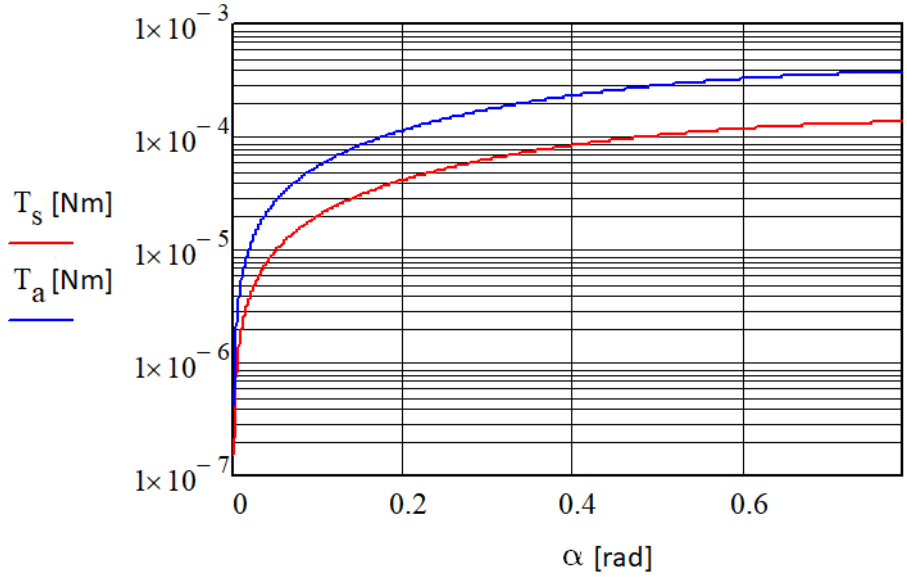


Figure 10: Aerodynamic and solar torque at 400 km altitude over the pitch angle with $\varphi = 45°$.

When the allowed $\varphi$ angle decreases the maximum altitude at which the aerodynamic torque is higher than the solar radiation torque is decreasing too which is shown in Figure 11.

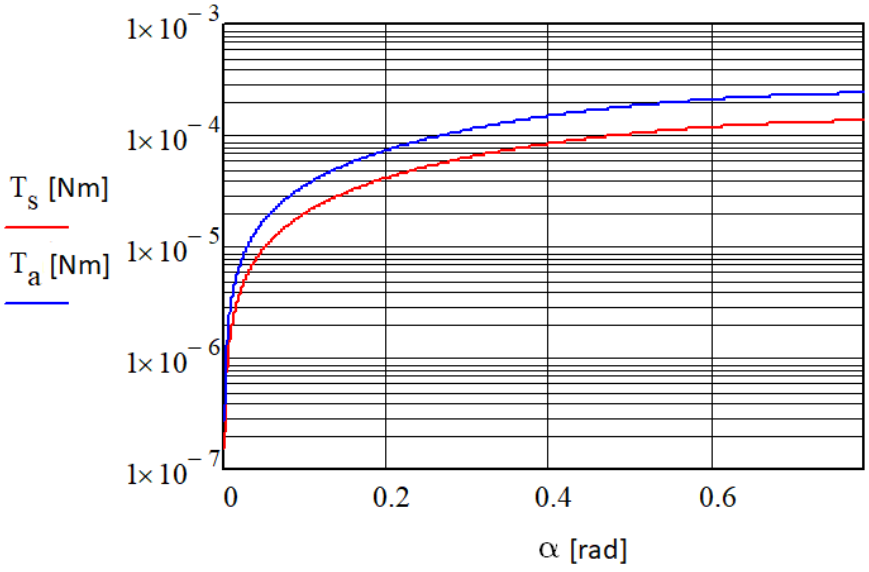


Figure 11: Aerodynamic and solar torque at 400 km altitude over the pitch angle with $\varphi = 20°$.

Here, the aerodynamic torque is still a bit higher than the solar torque, but the difference is decreasing with smaller $\varphi$. The solar pressure is always rectangular to the membrane segment one to investigate a worst-case scenario. Therefore, the force caused by the solar pressure is not influenced by $\varphi$.

Figure 12 shows the dependence of the different torques to $\varphi$. With an altitude of 400 km, the satellite will have a maximum tumbling angle of nearly 10.6°, without considering dynamics. During the deorbit and below an altitude of 450 km, the tumble angle will decrease caused by the continues decreasing altitude and the increasing atmosphere density.

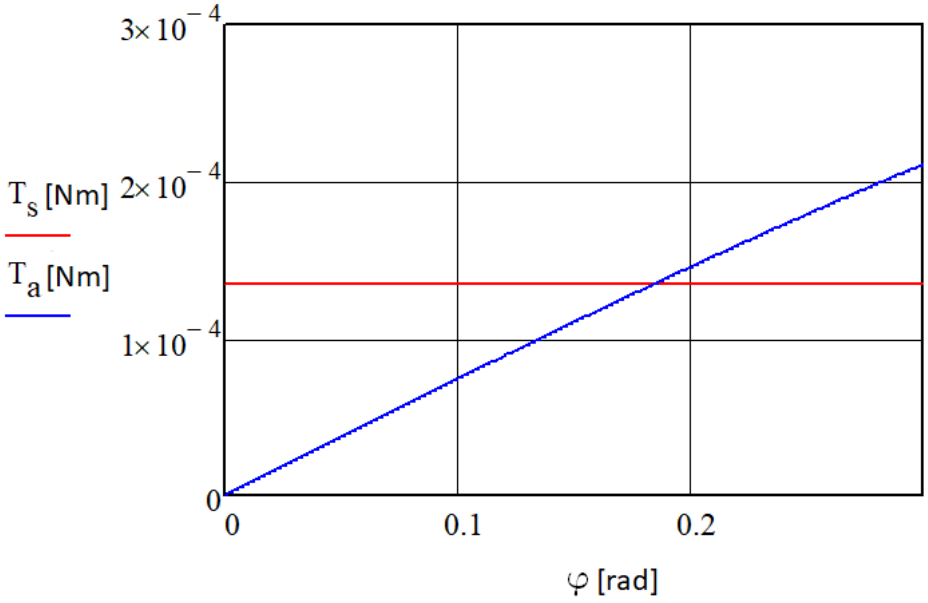


Figure 12: Aerodynamic and solar torque over $\varphi$ with $\alpha = 45°$ and $h = 400$ km.

All in all, the angled sail (pyramidal shape) has a positive effect on the passive stabilization of the satellite but only in the low altitude sections. If $\alpha$ is set to 0°, the solar radiation torque as well as the aerodynamic forces will not have any influence on the passive stabilization. This assumption is just valid for a perfect reflection of the solar radiation ($q = 1$) and a transparent satellite. Nevertheless, the pitch angle $\alpha$ is set to 0° in the ADEO-2 configuration because an altitude below 450 km will occur in the last view months. Regarding the deorbit time of the satellite including the ADEO-2 subsystem, the spacecraft will be about 15.6 years over the altitude of 450 km and about 3 months under that borderline before the reentry starts. So, the most time the satellite tumbles anyways. Furthermore, an angled sail would decrease the effective surface area or raise the required sail area and the mass of the satellite as well as increase the complexity of the ADEO subsystem. Therefore, the design and sizing of the membrane spool is done for a flat sail.

Due to the steady tumbling of the satellite during the orbit decent, a new average effective surface area which is rectangular to the flight direction needs to be calculated. As an assumption, the satellite will tumble with the same angular velocity around all three axes. The rotation around the longitudinal axis does not has any influence on the effective surface area. The rotation around Y- and Z-axis influence this surface area. Due to the assumption of the same angular speed, the new average effective surface area is calculated as

$$A_{average} = A \cdot \frac{2}{\pi} \cdot \int_0^{\frac{\pi}{2}} (\cos(\varphi))^2 \, d\varphi = \frac{A}{2} = 12.5 \text{ m}^2 \quad . \tag{42}$$

According to Equation (22) and due to the reduction of the effective surface area to the half, the deorbit time rises to the doubled value. Thereby, the deorbit time is 32 years which would overshoot the maximum possible deorbit duration of 25 years. The mass of the satellite or the starting altitude at which the orbit decent starts needs to be decreased otherwise the sail surface has the be increased. The sail surface area should be held by 25 m$^2$ and the mass of the satellite should stay at 500 kg. To reduce the deorbit time to 25 years, the maximum altitude at the beginning of the deorbit process needs to be reduced to about 728 km. This is calculated by iteration because changing the maximum altitude varies the factor $f$ in Equation (10) as well as the deorbit time in Equation (22).

# 4 Selection of the membrane material

The sail in the ADEO subsystem is made of a thin foil material with 100 nm aluminum coating on both sides of the membrane. The materials must withstand the space environmental conditions for more than 15 years in stowed configuration and 25 years deployed during the deorbit process. The ATOX and the VUV radiation as well as the high temperature cycles and its range are the most challenging environmental conditions in LEO.

In the ADEO-1 project different types of polyimides were investigated such like Kapton or Upilex-S. "Upilex-S is a heat resistant polyimide film… With a glass transition temperature above 500°C and a tensile strength of 657 MPa…" at room temperature. "DuPont Kapton is available in various modifications. Widely used is Kapton HN, which has good thermal and mechanical properties. The ultimate tensile strength at room temperature is 231 MPa, and its glass transition is at 360°C." [16, p. 26]

To be able to evaluate these temperatures, the maximum and minimum temperature in LEO for the sail must be investigated. The radiation which has an impact on drag sails originated from the solar radiation with the solar constant $P_S$ of about 1366.1 W/m$^2$ [11, p. 121], the Earth's albedo $P_A$ which is about 35% [16, p. 23] of $P_S$ and the infrared emission from the Earth $P_{IR}$ of about 200 W/m$^2$ [16, p. 23]. At first, the hot case will be investigated. According to [17, p. 9], a view factor for the investigation of the infrared emission of the Earth is calculated by

$$F_{e,s_c,1} = \left(\frac{r_E}{r}\right)^2 \quad . \tag{43}$$

Here, $r$ is the orbital radius and $r_E$ is the radius of the Earth with 6378.136 km (equatorial radius; [11], p. 107). For the hot case, the sail is placed rectangular to the ecliptic and between the Earth and Sun. The Stefan Boltzmann law can be used to calculate the radiated heat. In an equilibrium, absorbed and emitted heat must be equal. Therefore, the equilibrium temperature is calculated by

$$\sigma \cdot 2 \cdot A \cdot \varepsilon \cdot \left({T_{max}}^4 - \frac{{T_E}^4}{2} - \frac{{T_0}^4}{2}\right) = \left(P_S + P_A + P_{IR} \cdot F_{e,s_c,1}\right) \cdot \alpha_S \cdot A \quad , \tag{44}$$

$$T_{max} = \left(\frac{\alpha_S}{\varepsilon} \cdot \frac{\left(P_S + P_A + P_{IR} \cdot F_{e,s_c,1}\right)}{2 \cdot \sigma} + \frac{{T_E}^4}{2}\right)^{\frac{1}{4}} = 527.8\ \text{K} = 254.7\ °\text{C} \quad . \tag{45}$$

$\sigma$ is the Boltzmann constant ($5.6704 \cdot 10^{-8}\ \left[\frac{\text{W}}{\text{m}^2\text{K}^4}\right]$), $\varepsilon$ is the emission coefficient (0.035) and $\alpha_S$ the adsorption coefficient (0.14) of the sail [19, p. 23], $A_s$ is the sail surface (25 m$^2$). It needs to be considered that the Earth's radiation, the solar radiation as well as the albedo is only adsorbed on one side of the sail, while both sides radiate heat according to the temperature of the sail. Thereby, the left side of equation (44) is multiplied with 2. The Earth-facing side of the sail radiates to the Earth which has a temperature $T_E$ of about 330 K which roughly corresponds to the temperature in deserts. The sail side which is facing away from the Earth radiates to the space environment which is estimated with a temperature $T_0$ of 3 K [18]. Because of this small value $T_0$ has no high influence and therefore it is negligible. The altitude influences the temperature of the sail. With a smaller altitude, the view factor is rising. Thereby, the temperature is rising, too. The altitude for the maximum temperature investigation is set to 200 km.

The cold case appears when the sail is in the Earth shadow. Only the infrared radiation from the Earth needs to be considered. Additionally, the sail is now placed parallel to the ecliptic (nadir orientation

towards the Earth). Because of the new positioning a new view factor, according to [17, p. 9], is calculated by

$$F_{e,s_c,2} = \frac{1}{\pi} \cdot \left[ \tan^{-1}\left( \frac{1}{\sqrt{\left(\frac{r}{r_E}\right)^2 - 1}} \right) - \frac{\sqrt{\left(\frac{r}{r_E}\right)^2 - 1}}{\left(\frac{r}{r_E}\right)^2} \right] \tag{46}$$

In this position, both sail surfaces receive infrared radiation from the Earth. The maximum orbit altitude of 750 km is used (worst-case). The minimum temperature is calculated by

$$T_{min} = \left( \frac{\alpha_S}{\varepsilon} \cdot \frac{P_{IR} \cdot F_{e,s_c,2}}{\sigma} + \left( F_{e,s_c,2} \cdot T_E \right)^4 \right)^{\frac{1}{4}} = 168.3\ \text{K} = -104.9\ °\text{C} \quad . \tag{47}$$

with a roughly estimated temperature $T_E$ of the Earth of about 225 K. $T_E$ is multiplied with the view factor to get an average surrounding temperature. Additionally, the cosmological radiation with the temperature $T_0$ of about 3 K is negligible because $T_0$ does not influence $T_{min}$ that much. Here the denominator is not multiplied by the factor 2 because both sail sides "see" the Earth's surface which influences the radiation behavior of the sail.

Regarding the glass transition temperature of Upilex-S and Kapton HN, presented in [16, p. 26], both materials would withstand this temperature environment. Therefore, the requirement (PFM-ENV6), from Section 6.1, is confirmed. Because of the good mechanical and thermal properties, Upilex-S is the favor used material. The problem is, that the aluminized coated Upilex-S is not produced anymore. Therefore, Kapton is used as membrane substrate in the ADEO-2 project. Depending on the results of the on-going material investigation it could be considered to use the more atomic oxygen resistant fluorinated ethylene propylene (FEP) foils.

It must be considered, that the foil has a thickness in the µm range. Because of the small thickness of the membrane, it needs a layer which is high in resistance against ATOX and VUV radiation. Furthermore, the membrane cannot be thicker, because it needs to be folded for stowing which is just possible with a thin and flexible material. A thicker membrane would cause a higher stowed volume and a higher mass.

For the membrane coating aluminum, titan dioxide and silicon dioxide were investigated. The aluminum has a higher binding energy of the atoms compared to oxygen atoms which leads to a good resistance against ATOX. "Aluminum provides limited shielding against VUV radiation." To shield 99% of the radiation the aluminum needs a thickness of 1.5 µm. Furthermore, the influence of ATOX to silicon oxide is very low. "$SiO_2$ is an electrical non-conductive material and cannot provide suitable antistatic properties…". Electrical conductivity is important to avoid charged surface areas and the risk of high potentials. High potentials can cause lightning and thereby destruction of sensitive components like electronics. The titan dioxide has a better resistant against VUV radiation compared to the aluminum. Furthermore, titan dioxide is a semiconductor. Therefore, it can avoid charged surface areas. The electrical "…resistance strongly depends on type of the substrate." For ADEO a non-conductive polyimide is used which would increase the electrical resistance of the sail. [16, pp. 27-28]

Because of the high resistance against ATOX and the good conductivity, aluminum is used coating on the substrate. To produce such thin layers, the aluminum is sputtered on the Kapton. The thickness of the aluminum layer is 100 nm on each side of the membrane as this is a standardized product. The Kapton itself is 7.6 µm thick. In total the membrane has a thickness of 7.8 µm. To ensure well functioned sail without cracks, crack stoppers and reinforced edges are used which are presented in Section 6.3.

# 5 Stowing and deployment strategy

In the following sections, the stowing and the deployment strategy of the ADEO-2 drag sail is presented. Because ADEO-2 is currently in the preliminary design phase (status: February 2019), only this design can be shown.

## 5.1 Stowing and deployment of the drag sail

The ADEO-2 drag sail is divided in four triangle membrane segments and is stowed based on zig-zag folding, presented in Figure 13. The sail segments are folded parallel to the triangle height and coiled on a spool. The membrane spool is integrated vertical in the ADEO-2 accommodation. This is achieved by an additional folding that is along the triangle height. The distance between these lines is 120 mm except the folding lines next to the triangle height line. They have a distance of 47.5 mm due to the position of the membrane plain on the spool in the deployed configuration. Higher distances between these folding lines cannot be realized caused by the requirement of the maximum accommodation height of 200 mm of the ADEO-2 subsystem presented in Section 6.1 (PFM-DF3). According to the venting requirement PFM-ENV4 in Section 6.1, the zig-zag folding is a good stowing method also concerning to the depressurization of the membrane which was investigated in recent DLR projects. The air between the folded membrane layers only needs to go through the distance of maximum 120 mm before leaving the membrane (folding width).

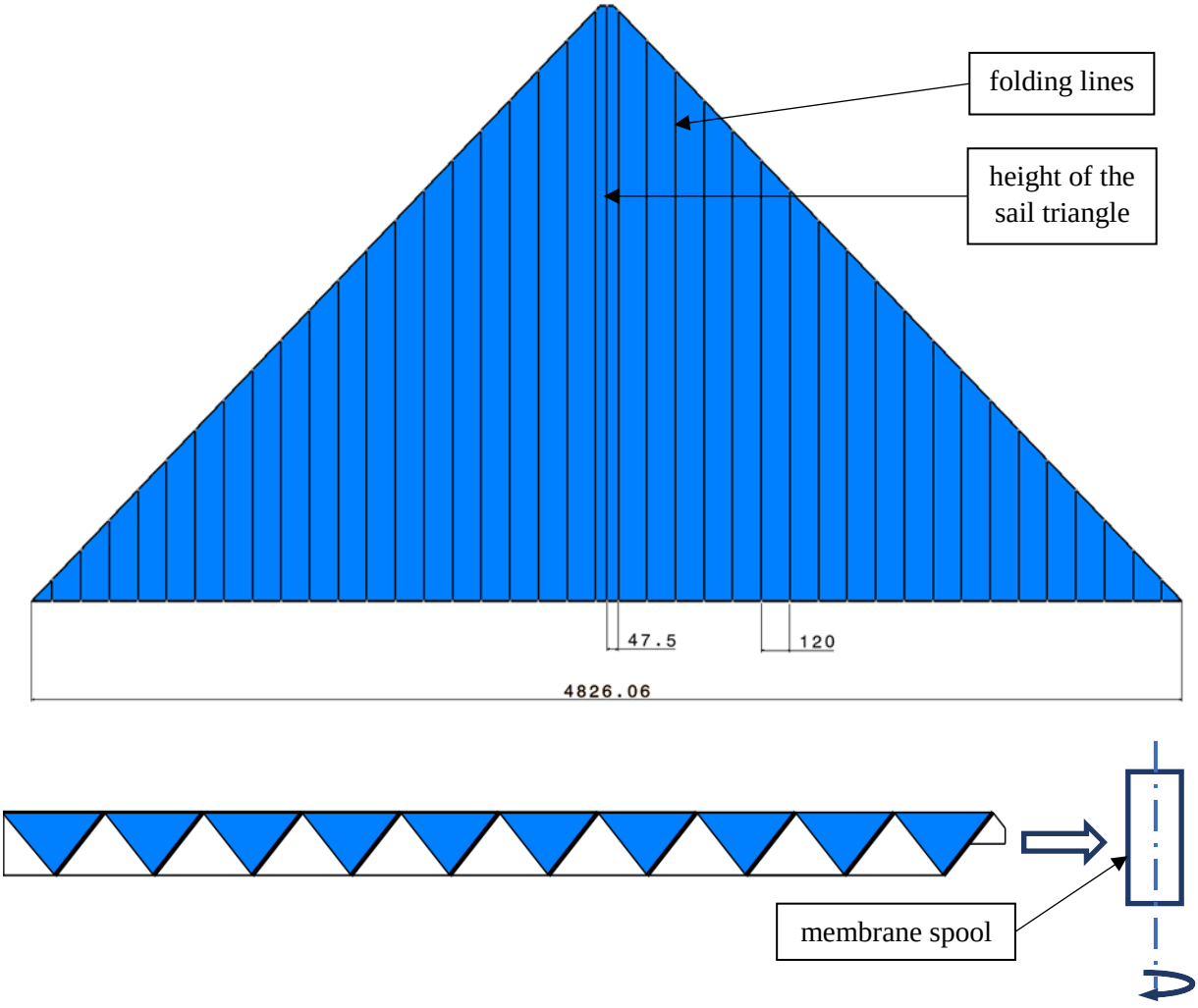


Figure 13: Stowing and deployment strategy. Folding Lines of one Membrane Segment (top) and coiling (bottom).

During the deployment, four booms are deployed by a motor. The shape of the boom structure is shown in Figure 1. The booms and membrane segments are connected via interfaces which transport loads. Thereby, the membrane is pulled off the sail spool.

## 5.2 Design variants of the membrane spool

Two different membrane spool variants are briefly investigated. In Figure 14, the Four-Sail-Spool design (left) and the One-Sail-Spool design (right) are presented. These designs are described and evaluated in the following subsections.

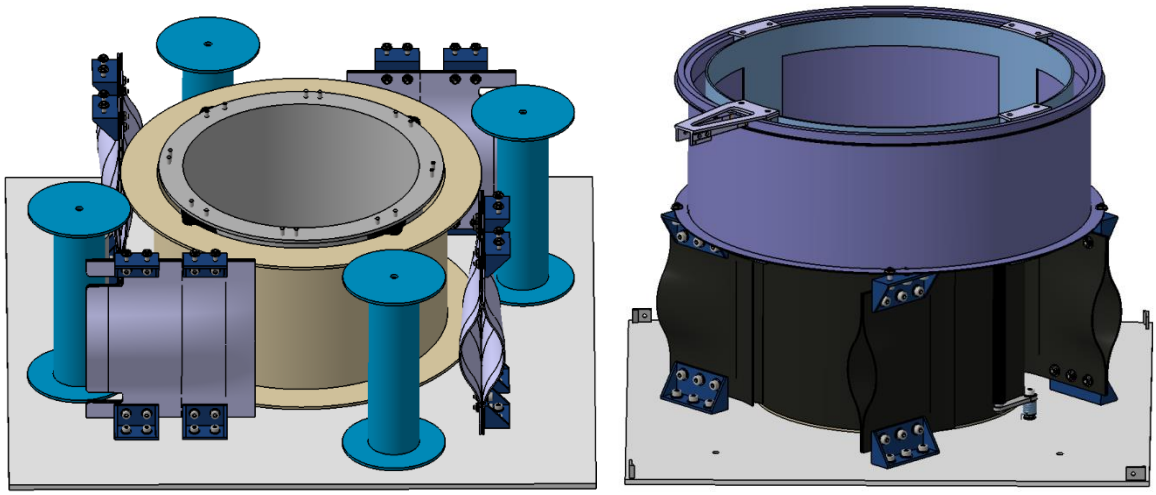

Figure 14: Variants with different number of spools. Design with four sail spools, one for each segment (left) and a design with one sail spool (on top of the boom spool) is shown in on the right.

### 5.2.1 Four-sail-spool design

A design with four sail spools is shown in Figure 14 on the left-hand side. In this case the spools are nearly in the same plane as the boom spool and positioned around the boom spool. The small offset between the boom and membrane plane causes only low bending moments in the boom structure during the deployment. This design provides the smallest height of the ADEO-2 subsystem which is an important parameter (see Section 6.1, PFM-DF3). The four spools will not or only marginal increase the height of ADEO-2. Furthermore, the mass of the four small sail spools would be smaller or at least comparable to the one with one bigger spool.

### 5.2.2 One-sail-spool design

The design with one sail spool on top of the boom spool is illustrated in Figure 14 on the right. All four sail segments are coiled onto the same spool. On the one hand this design has the advantages that the sail segments can be coiled on a larger diameter of about 250 mm and interface length between booms and sails could be smaller. The outer diameter of the spool would be about 320 mm.

On the other hand, the sail spool would significantly increase the height of ADEO-2, the large diameter of the spool results in high mass (comparable to the one of four single smaller sail spools) and more structural mass would be required to carry the acceleration loads of the sail spool during launch. In addition, the limitations in accommodation height (200 mm, Section 6.1 (PFM-DF3)) of the ADEO-2 subsystem lead to a maximal width of the folding of 50 mm which results in approximately 100 folded layers per segment. This number of folding layers is very difficult to fold, especially without any special tools. The offset between boom and membrane plain would increase significantly. Thereby, the boom structure must withstand high bending moments. The boom would have high non-predictable deformations.

### 5.2.3 Conclusion

Considering the disadvantages of the one-sail spool design with respect to height of the ADEO-2 system, the huge number of required folds, the high bending moments in the booms and the higher structural mass, the design is based on the Four-Sail-Spool concept.

# 6 Membrane

In Section 6.1 relevant system requirements are listed followed by assumptions under which the development is carried out. The membrane design aspects of ADEO-2 are described in Section 6.2. Furthermore, the current preliminary membrane design is presented in Section 6.3.

## 6.1 Requirements and assumptions

In the following section relevant system requirements and assumptions for the design of the membrane are listed and explained. Relevant requirements, stated in the ADEO-2 PFM Requirements document [20, p. 16-20], are:

- „The ADEO subsystem shall withstand…" the rapid decompression during the lunch "…without any damage" (PFM-ENV4).
- "The ADEO subsystem shall be compatible with the following storage requirements: 3year storage on ground, 6 months storage during launch phase, and 15 year storage in-orbit" (PFM-ENV5).
- "The ADEO subsystem shall withstand the maximum sun illumination/eclipse of the mission in stowed and deployed configuration" (PFM-ENV6).
- "The mass of the ADEO subsystem shall be not greater than 5% of reference mission S/C" (PFM-DF2).
- "The size of the ADEO subsystem shall not be larger than 500 mm x 500 mm x 200 mm (H x W x L)" (PM-DF3).
- "The subsystem shall provide launch locks" (PFM-DF11).
- "All parts and materials used in the ADEO subsystem should be ITAR free" (PFM-DF14).

As baseline, the membrane material is a 7.6 µm thick polyimide (Kapton) coated with 100 nm aluminium on both sides. A higher thickness of the membrane is not recommended due to the required flexibility, restricted volume for stowing and mass (PFM-DF2). The mass of the membrane is 11 $g/m^2$. Investigations of the total mass of the membrane spool are made in Section 7.4. This material combination is provided by the company Sheldahl, is ITAR free (PFM-DF14) and should have enough resistance against ATOX and VUV radiation for a duration of 15 years stowed and 25 years deployed in the LEO, which is necessary for the requirement in PFM-ENV5. Further material investigations are described in Section 4.

The interface lengths are influenced by the position of the membrane spool and the interface connection points at the boom. These lengths must be calculated for the stowed version of ADEO-2 to ensure a certain preload on the rolled sail segments. A launch lock is used to prevent the spool from rotating during the launch and lifetime of the satellite (PFM-DF11). This ensures the tensioning of the interfaces from the spool side. For the preliminary design the position of the spool provided by the overall accommodation is shown in Figure 15. The interface point between boom and membrane is 10 mm in front of the boom guide edge and has 40 mm distance to the boom longitudinal axis as presented in Figure 16.

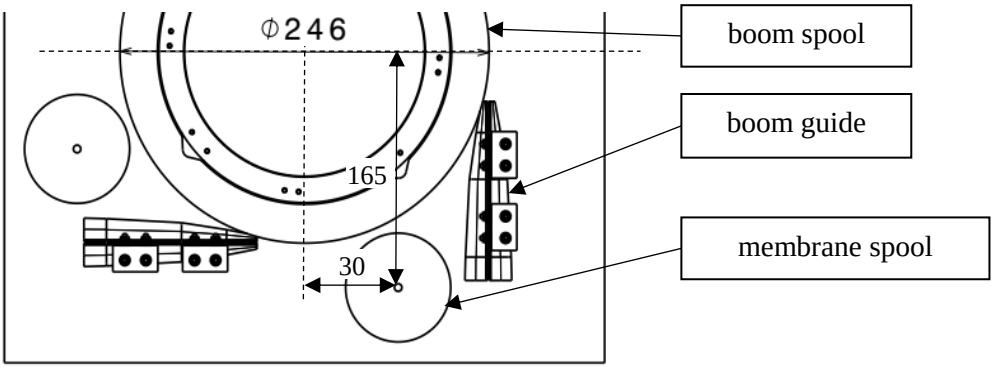


Figure 15: Position of the membrane spool.

## 6.2 Membrane design aspects

This section presents different design aspects for the implementation of the Four-Sail-Spool design in the ADEO-2 system. It is described why the chosen design is selected and what principle design decisions are made.

First, a decision of the rotation direction is made. Both directions are investigated. The main aspect that needs to be considered is to ensure tensioning of the interface during deployment or at least ensure that only a small slack during deployment is present. Furthermore, the positioning of the spool is chosen such that a direct connection between the membrane and the boom is possible, such that further components e.g. pulleys are not required.

The two connection points from the interface to the membrane are in the same position on the spool. From that point the interfaces extend to the mounting point on the boom side. The rotation direction is defined as clockwise and counter clockwise when looking to the spool from the top.

### 6.2.1 Clockwise deployment

In this case, the uncoiled length of the blue interface, shown in Figure 16, is very short with about 39.85 mm which is the distance of the upper boom interface point to the uncoiling point of the short boom – membrane interface. With 177.99 mm, the uncoiled length of the red interface is much longer. The interfaces reach several millimetres into the membrane segment and an additional length is coiled on the spool. This also protects the folded segments when subjected to vibration loads and during assembly, integration and verification (AIV) and assembly, integration and testing (AIT) as well as handling during transport. During the deployment, the boom will deploy parallel to the boom axis.

One of the benefits of this rotation direction is that the interfaces are nearly always tensioned during the deployment process. The different interface orientations have dissimilar angels to the boom deployment direction in the stowed configuration. Furthermore, $\gamma$ and $\delta$, shown in Figure 16, are decreasing differently during the deployment process and this leads to a reduction of tension in the long interface while the shorter interface will always be under tension. Another advantage is that the interfaces between boom and membrane have some space to the boom and boom support structure to ensure that the sail and interface do not get entangled.

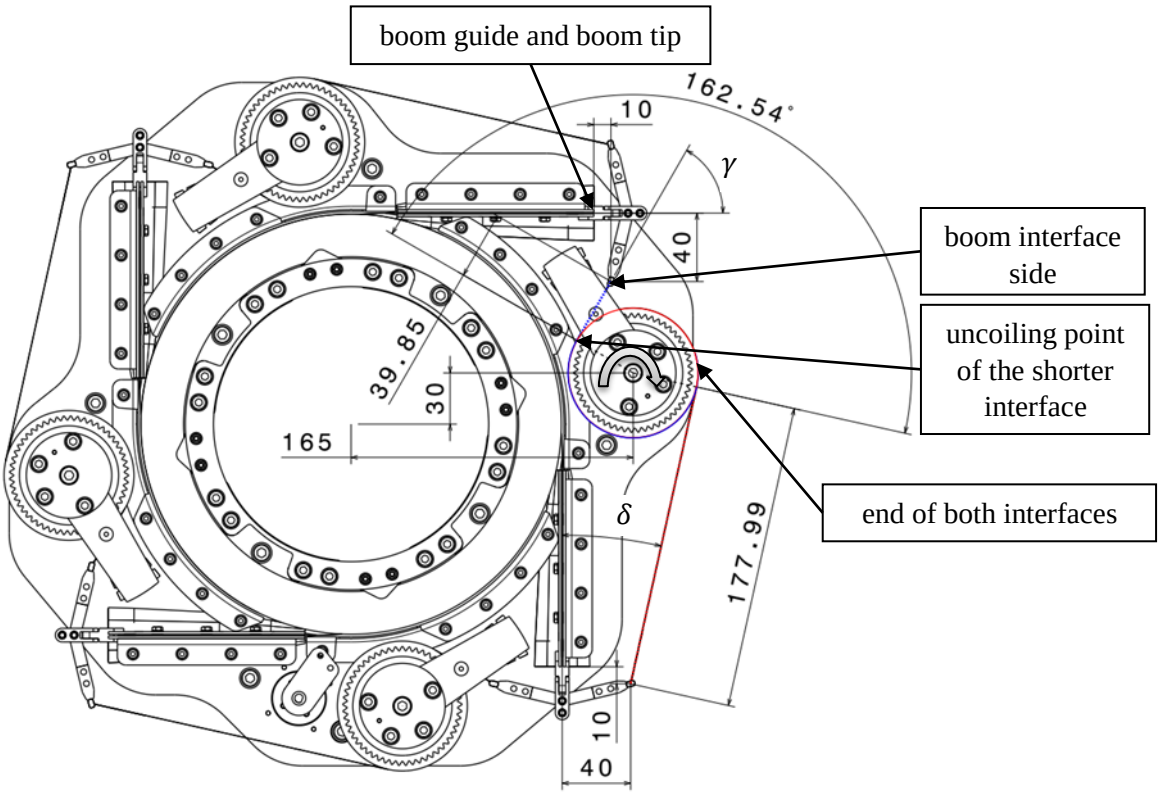


Figure 16: Clockwise rotation of the membrane spool.

### 6.2.2 Counter clockwise deployment

The counter clockwise rotation of the membrane spool would result in interfaces that have nearly the same lengths. The benefit is that the length of the long interface (blue line) is decreased while the shorter interface (red line) length is increased as shown in Figure 17 (compared to the clockwise deployment lengths). Overall this results in a slightly larger membrane area.

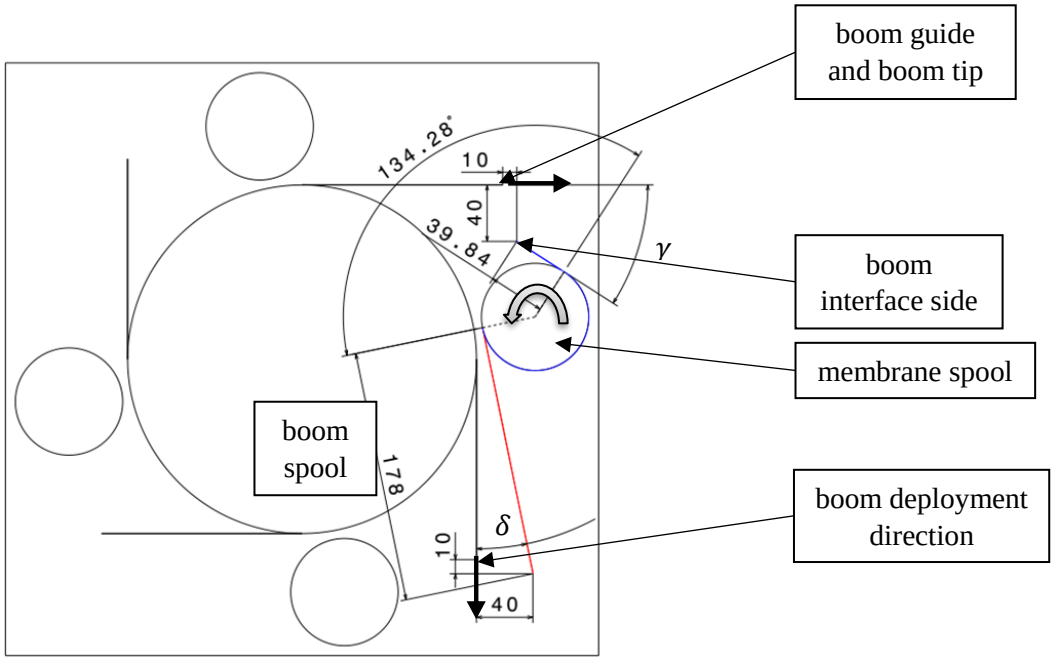


Figure 17: Geometry for the counter clockwise rotation of the membrane spool.

A big disadvantage is the loss of interface tension at the beginning of the deployment process. On the upper interface (blue line), the difference in deployed length compared to the distance between boom interface and uncoiling point on the sail spool significantly increases at the beginning of the deployment. This problem accurses because of the change of the relative position of the uncoiling point at the spool and the upper boom interface point (first strait section of the blue line (uncoiled), Figure 17). Looking in the direction of deploy, the boom interface is at first behind and then in front of the uncoiling point. The angle $\gamma$ changes during the deployment from a value under 90° to nearly 180° while $\delta$ is just decreasing a little bit.

The slack span $y$ is estimated as

$$y = l_{real} - l_{req} \quad . \tag{48}$$

Here, $l_{real}$ is the length of the upper deployed sail edge which is in the early deployment process just the upper interface length (blue line). The length $l_{req}$ is the length which can be tensioned during the deployment process. For $l_B > 13$ mm, it is calculated by

$$\begin{aligned} l_{req} = & \sqrt{|53.5^2 + (l_B - 13)^2| - R_{Sp}^2} + R_{Sp} \\ & \cdot \left[ 90° - \left| \tan^{-1}\left( \frac{182 + l_B}{2} \right) \right| + \cos^{-1}\left( \frac{R_{Sp}}{\sqrt{1.5^2 + (182 + l_B)^2}} \right) \right. \\ & \left. + 270° - \left| \tan^{-1}\left( \frac{53.5}{l_B - 13} \right) \right| - \cos^{-1}\left( \frac{R_{Sp}}{\sqrt{(l_B - 13)^2 + 53.5^2}} \right) \right] \end{aligned} \tag{49}$$

and for $0 \leq l_B \leq 13$ mm, it is calculated by

$$\begin{aligned} l_{req} = & \sqrt{|53.5^2 + (l_B - 13)^2| - R_{Sp}^2} + R_{Sp} \\ & \cdot \left[ 90° - \left| \tan^{-1}\left( \frac{182 + l_B}{2} \right) \right| + \cos^{-1}\left( \frac{R_{Sp}}{\sqrt{1.5^2 + (182 + l_B)^2}} \right) \right. \\ & \left. + 90° + \left| \tan^{-1}\left( \frac{53.5}{l_B - 13} \right) \right| - \cos^{-1}\left( \frac{R_{Sp}}{\sqrt{(l_B - 13)^2 + 53.5^2}} \right) \right] \quad . \end{aligned} \tag{50}$$

The outer membrane spool radius $R_{Sp}$ is about 38 mm (see also Section 7.1.3). Furthermore, $l_B$ is the distance which the boom tip moves during the deployment process. All other values are distances between the boom interface sides and the centre of the membrane spool. These additional geometry values are presented in Figure 18.

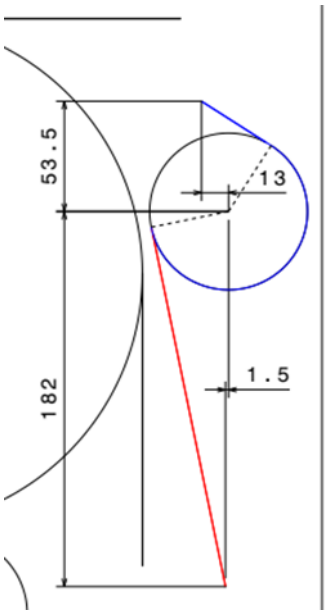


Figure 18: Geometry of the membrane spool and the interface connection point on boom side.

$l_{real}$ is calculated by

$$
\begin{aligned}
l_{real} &= l_{req}(l_B = 0) \\
&+ \left[\left(\sqrt{(182 + l_B)^2 + 1.5^2 - R_{Sp}^2} - \sqrt{182^2 + 1.5^2 - R_{Sp}^2}\right) \cdot \frac{1}{R_{Sp}}\right. \\
&- \left(\left|\tan^{-1}\left(\frac{182 + l_B}{2}\right)\right|\right. \\
&- \cos^{-1}\left(\frac{R_{Sp}}{\sqrt{(182 + l_B)^2 + 1.5^2}}\right) \\
&\left.\left. - \left\{\tan^{-1}\left(\frac{182}{2}\right) - \cos^{-1}\left(\frac{R_{Sp}}{\sqrt{1.5^2 + 182^2}}\right)\right\}\right)\right] \cdot R_{Sp} \quad .
\end{aligned}
\tag{51}
$$

Figure 19 shows an estimation of the slack span during the first 200 millimetres of the deployment. The slack during the first deployed millimetres is rising. This diagram shows only the first revolution because afterwards the membrane and the boom – membrane interface starts to unfold which would change the geometry.

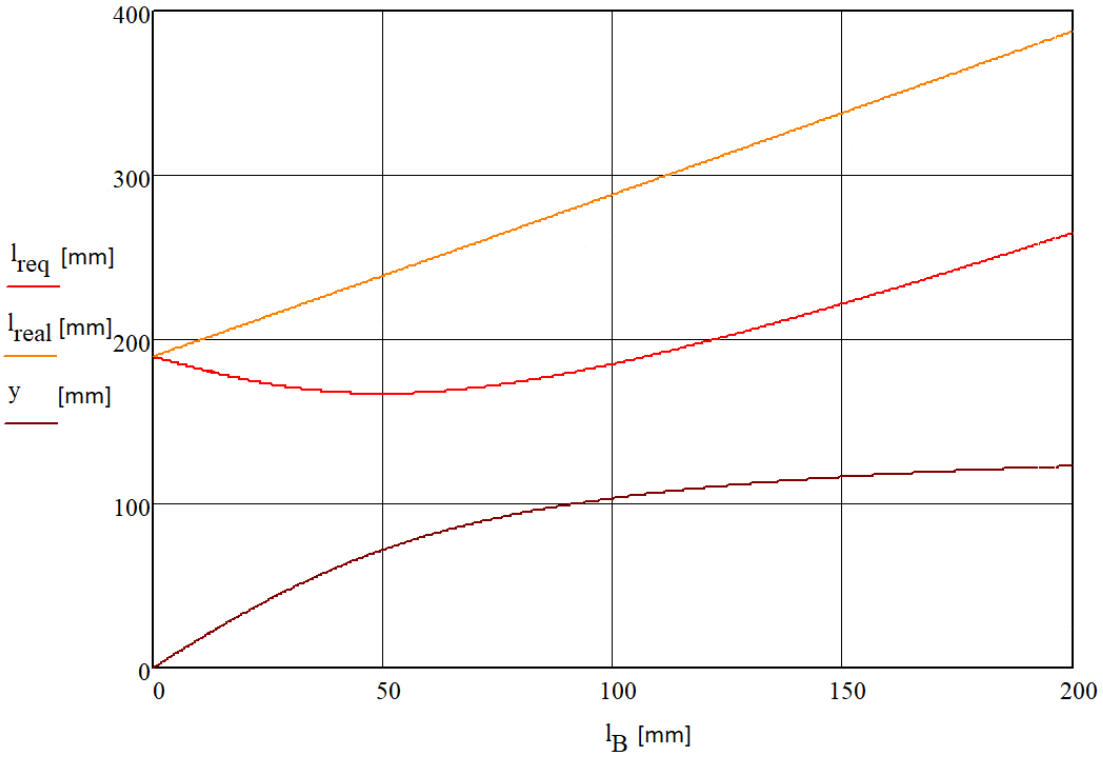


Figure 19: Interface length $l_{real}$, distance between the upper boom interface point and uncoiling point of the red interface line $l_{req}$ and the slack span $y$ as difference between these lengths.

### 6.2.3 Boom - membrane interface alignment

While the interface length is given by the accommodation in the stowed configuration, the alignment of the interface on the membrane is a further variable which needs to be investigated. This aspect is described in the following sections. The geometry of the membrane segment is shown in Figure 20. It must be considered, that the sail design has now slightly different geometrical values compared to the one which is presented in this evaluation of the interface orientation. This difference has no impact on the evaluation of the various sail designs and is caused by the steady iterations during the sail designing with other workplaces. The following design variants are differentiated:

- interfaces extend along the sail inner edge (the edge along the boom)
- interfaces extend along the outer edge of the membrane
- interface extends along the bisecting line
- interface extends along a line that intersects with the centre of the triangle area

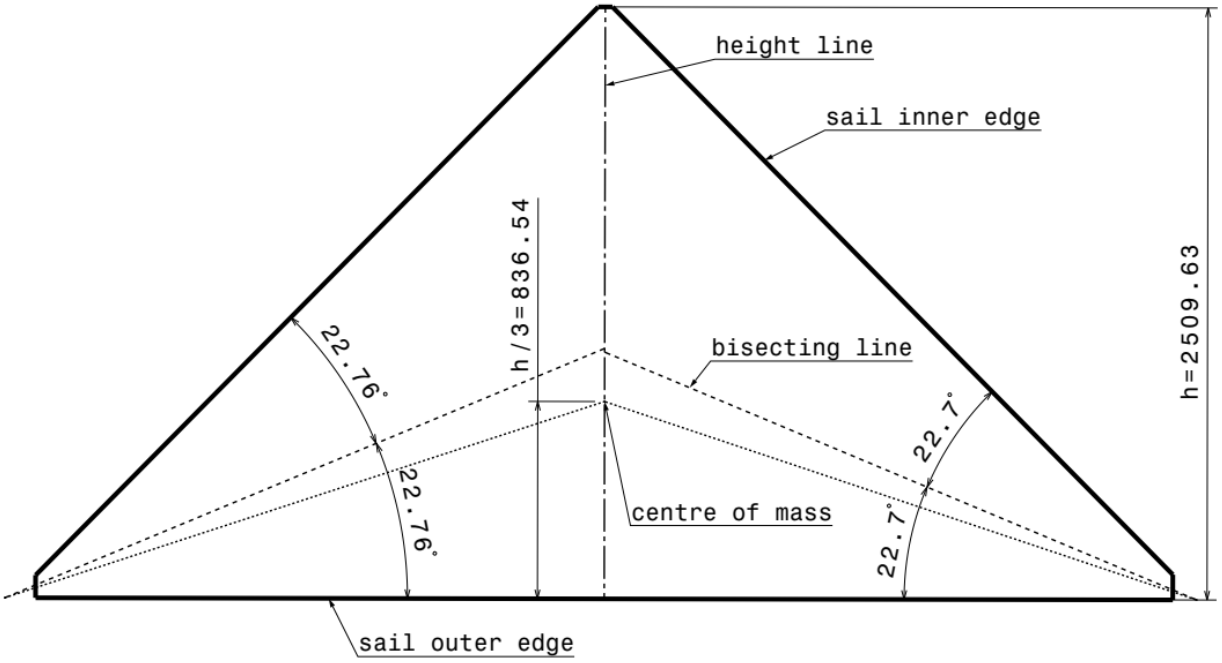


Figure 20: Membrane segment with description of used elements in all four designs.

The interfaces are also evaluated regarding the deployed boom length $l_{Bo}$ and the deployed sail area $A$. Furthermore, it was investigated how well the area between the booms $A_B$ is used for the deployment of sail area $A$ by calculating the fraction of areas and evaluate it with the parameter η. η is calculated by

$$\eta = \frac{A}{A_B} \quad . \tag{52}$$

The parameters are shown in Table 2. The area between the booms is calculated as

$$A_B = \frac{2 \cdot (l_{Bo} + 123\ \text{mm}) \cdot (l_{Bo} - 123\ \text{mm})}{10^6} \quad . \tag{53}$$

Table 2: Parameters for sail interface design evaluation

| | 1. Design | 2. Design | 3. Design | 4. Design |
|---|---|---|---|---|
| $l_{Bo}$ (boom length) [m] | 3729 | 3793 | 3776 | 3781 |
| $A$ (sail area) [m²] | 24,428 | 25,988 | 25,264 | 25,4 |
| $A_B$ (area between booms) [m²] | 27,781 | 28,743 | 28,486 | 28,562 |
| η (efficiency) [%] | 0,879 | 0,904 | 0,887 | 0,889 |

#### 6.2.3.1 Interfaces extends along the sail inner edge

The first idea is that the interface is parallel to the inner edges of the sail segments like it is shown in Figure 21.

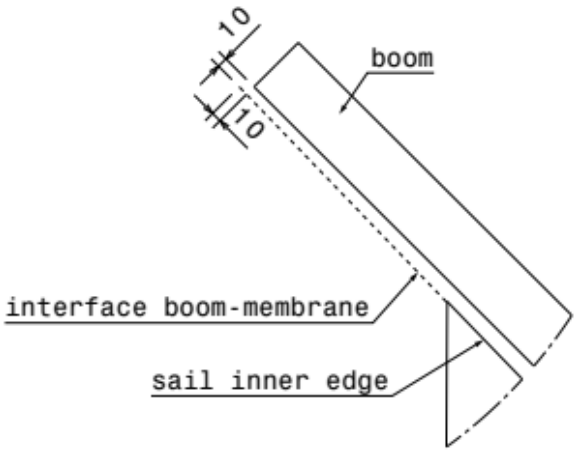


Figure 21: Boom – membrane interface parallel to the sail inner edge.

In this design, the boom is relatively long compared to the sail edge length and the sail will not get spanned very well because of the force direction which is parallel to the inner edge. This extra length increases the mass of the booms while the drag sail area decreases slightly. During the deployment, the booms are changing the geometrical values of width and height. In the deployed configuration the boom width is 60 mm (30 mm to the boom axis). Figure 21 shows, that the angle between the interface and the boom axis is very small. A boom interface point on the boom axis (in the middle of the boom) would cause an extremely long boom and interface to not have contact between boom and membrane which is not efficient in this configuration.

#### 6.2.3.2 Interfaces extends along the outer edge

The second idea is to position the interface parallel to the hypotenuses of the sail segment. This configuration is presented in Figure 22.

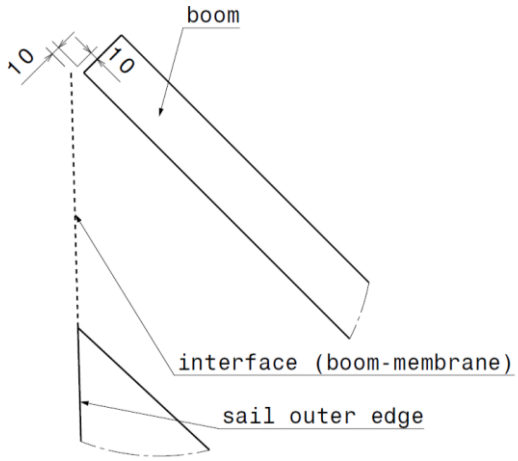


Figure 22: Boom – membrane interface parallel to the sail outer edge.

The sail area is slightly larger related to the first design which decreases the deorbit time. The boom length is decreasing, but the “dead space” between boom and membrane is rising extremely. Furthermore, the force distribution is not ideal for a good deployment and tensioning of the sail membrane.

#### 6.2.3.3 Interface extends along the bisecting line

In this design, the position of the interface is along the bisecting line of the outer corners of the triangular segments.

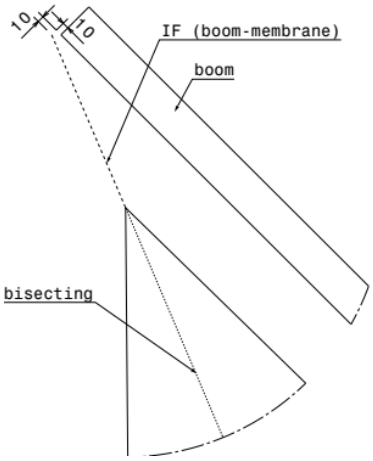


Figure 23: Boom – membrane interface parallel to the bisecting line.

This design balances the advantages and disadvantages of the first two concepts. Here the force distribution is better and the sail spanning will improved. The “dead space” between boom and membrane and the boom length compared to the membrane inner edge length is an approach between these first designs.

#### 6.2.3.4 Interface extends along a line that intersects with the centre of mass of the triangle

To improve the force distribution in the deployed position a fourth configuration in which the interfaces are orientated to one third of the height of the sail segment is investigated. The triangle is nearly symmetrical and the interfaces are approximately pointing to the centre of mass of the sail segment as shown in Figure 24. As a result, the force direction is nearly pointing on the centre of mass. This is assumed to be the best design to tension the sail in the deployed configuration while the impact on the deployed area and boom is minor. A disadvantage are the deployment forces which are passing the interfaces. Because the interfaces are not orientated to the sail spool after the deployment, the forces are rising at the end of the deployment.

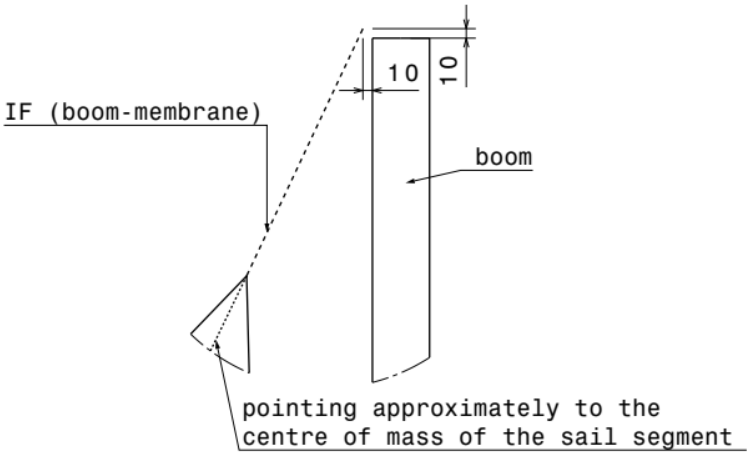


Figure 24: Boom – membrane interface pointing to the centre of mass.

### 6.2.4 Conclusion

The configuration with the clockwise rotation is used for the ADEO-2 deployment. The huge slack when using the counter clockwise spool rotation is a clear disadvantage. The large slack can lead to an entanglement of the interface.

Another disadvantage of the counter clockwise deployment is the small distance between the boom guide, the larger interface and membrane during the deployment process. In this configuration there is

a high risk of jamming between those parts. A solution could be to shift the interface connection point from the boom further away and/or change the position of the sail spool.

The change of deployed area, also compared to the area between the booms, is minor for the four different interface variants. The fourth variant is chosen, because it provides a good tensioning of the sail.

## 6.3 ADEO-2 membrane design

This section describes the preliminary design of the membrane that takes the above stated requirements, assumptions and general design decisions with respect to the stowing strategy, interfaces and spool rotation direction. It takes into account all interfaces (Section 6.3.1), joining lines (Section 6.3.2), crack stoppers (Section 6.3.3) and reinforced edges (Section 6.3.4). Due to the current membrane design the sail area is decreasing to 24.6 $m^2$. In this surface area no booms as well as other ADEO-2 structures except the sail itself are investigated. The whole effective surface area of the deployed structures is higher than 25 $m^2$ because just one boom has approximately 0.2 $m^2$ effective surface area.

### 6.3.1 Interface

The membrane needs interfaces or mounting points to the boom and the membrane spool. The latest development is an interface which consists of membrane material instead of the cables that were used in the precursor ADEO activity. The ADEO-1 interface design had several disadvantages with respect to the interface guidance which lead to an entanglement of the interface cable. In addition, these very thin cables were rolled up on to the membrane spool to a certain point on top of the membrane. This can damage the membrane coating, especially under vibration loads, which is crucial for the protection against the space environment.

#### 6.3.1.1 Membrane – membrane spool interface

The principle design of the interface is shown in Figure 25. The connection between interfaces and membrane or membrane spool is only based on gluing and consists of four interface sections. All are bonded to the membrane and are folded to 90° to be rectangular to the sail surface and parallel to the membrane spool longitudinal axis to ensure a well connection between the interface and membrane spool. The two interface sections on the upper sail surface are connected to each other with a transfer adhesive. These connected sections are rolled up and glued on the membrane spool to a certain length to avoid peeling off the interface from the spool. The same procedure is used on the other side of the sail surface with the other two interface parts.

In the stowed configuration, the interface membrane material is folded in line with the folding line that is along the height of the membrane to ensure good stowing properties. It is made from a flexible aluminized polyimide membrane comparable to the material of the sail membrane but with a thickness of 76 µm. The high flexibility is needed because the interface is flat folded and coiled on the spool in the stowed configuration and is unfolded into the configuration, shown in Figure 25, during the deployment. The interface is bonded throughout the surfaces. This increases the resistance against cracks e.g. due to space debris or micrometeoroids. Furthermore, the interfaces provide an internal four times redundancy because it consists out of four interface parts, two foils, left and right, on the top and two foils, left and right, on the bottom. Each of the interface parts is strong enough to mount the sail segment to the spool. The only differences between the upper and lower parts are the folding direction and the height of the interfaces. One is folded to +90° while the other one is folded to -90° like it is shown in Figure 25 (detail). As presented in Figure 31, the upper interface parts have a height of 47.5 mm and the lower ones a height of 72.5 mm. The different height values of the interfaces are caused by the final membrane plane position in the deployed configuration. This offset of 12.5 mm is initiated by the change of the boom shape during the deployment.

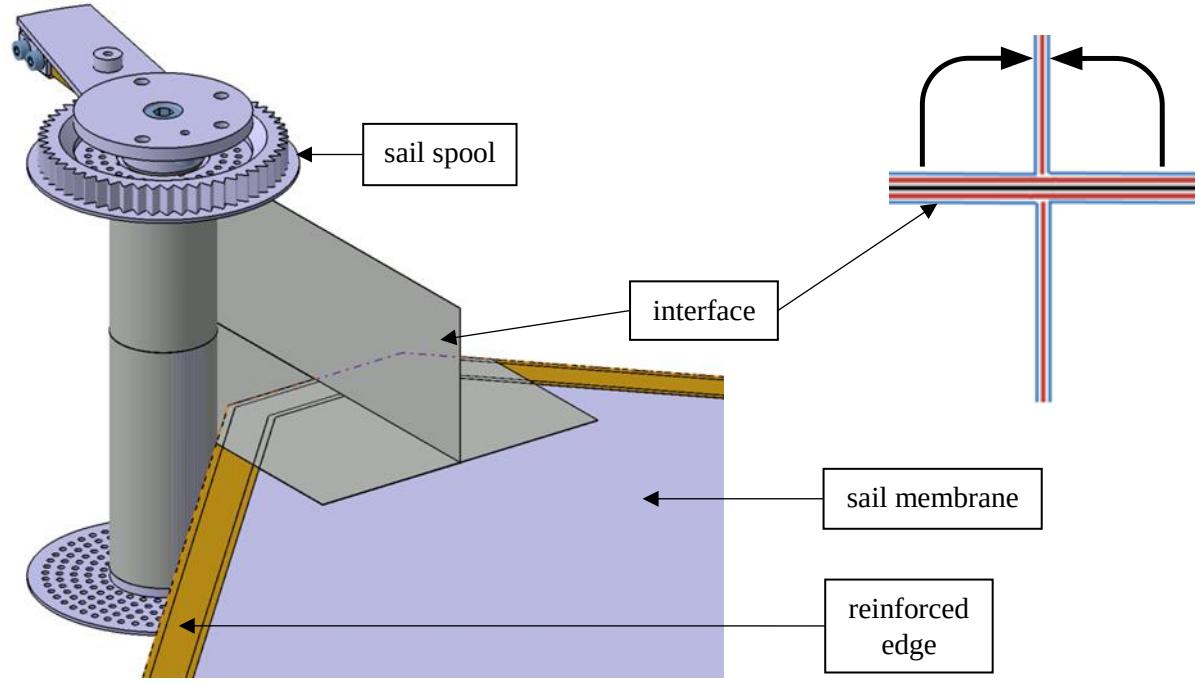


Figure 25: Illustration of the spool – membrane interface (deployed). The detail in the top-right corner shows the layer setup consisting out of the membrane base material (black), the foil material for the interfaces (blue) and the transfer adhesive (red).The curved arrows in the detail show the folding direction of the membrane and interface in the stowed configuration.

#### 6.3.1.2 Boom – membrane interface

The boom membrane interface is based on the same functional principle than the membrane-spool interface. The design is illustrated in Figure 26. The interface is symmetric to the sail membrane plane. These parts are on both outer membrane corners with just small geometrical differences and folded in the opposite directions. Because of the same general design of the right and left boom – membrane interface, only the right one will be described.

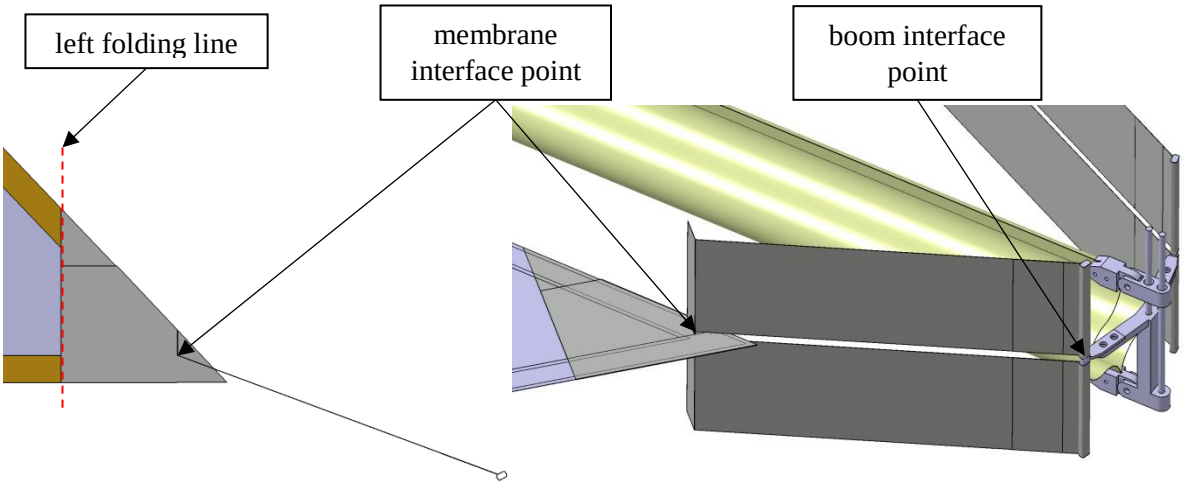


Figure 26: Top view of the right boom – membrane interface (left picture); view of the right boom – membrane interface (right picture).

The folding line of the interface is on the middle line between two folding lines of the sail. In Figure 26 is shown, that the right folding line of the membrane based on the interface does not exist due to the

geometrical values of the sail. This design provides an interface that fits to the spool height (or folding length) which allows a more even load introduction to the coiled membrane in the stowed configuration and the thicker interface foil provides also a protection cover for the coiled membrane.

The boom – membrane interface consists of three different parts, a left and a right part which forms the main interface design and an additional (U-shaped) part which is added to increase the stiffness of the corner as well as to have a good force distribution into the sail and good resistance against cracks. All three pars are shown in Figure 27 in an exploded view. The left and right parts are glued together and to the membrane surface. The U-shaped part is glued on the top of the left and right as well as on the membrane surface. The interface stripes are aligned so that the tension force acts along a line to the approximate CoA of the triangle area in the deployed configuration and are parallel to the folding lines in the stowed accommodation.

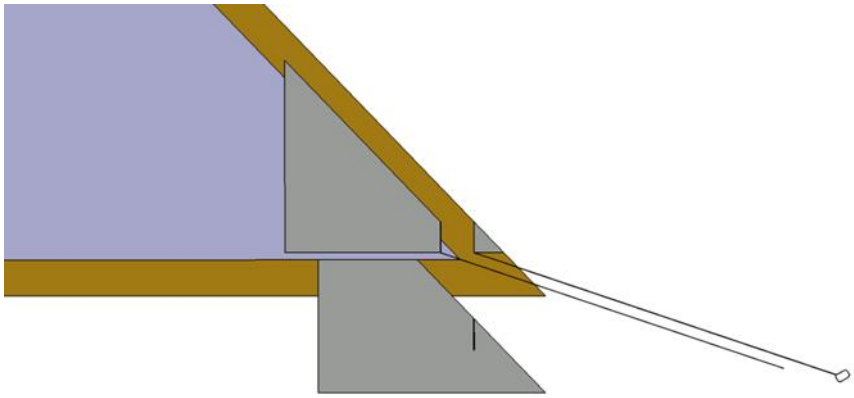

Figure 27: Exploded top view of the shorter interface.

The interface point to the boom is designed as an aluminium sleeve bonded to the interface with the transfer adhesive, presented in the right picture of Figure 26. The aluminium sleeve is mounted on the boom tip designed by DLR FA in Braunschweig.

The membrane interface point, presented in Figure 26, is the position of the vertical folding line on the interface. This point is the border between the glued interface section on the membrane and the moveable part and it needs to be positioned close to the sail inner edge. This is driven by the geometry during the deployment of the sail. During the deployment, the boom – membrane interface is tangential to the current coiling radius of the membrane spool, shown in Figure 28. Additionally, this interface is always pointing to the boom interface point (aluminium sleeve in Figure 26). These two boundary conditions influence the sail geometry. The right picture of Figure 28 shows the distance between the boom and inner sail edge. This distance is very small and thereby the design driver for the membrane interface point position with respect to the distance to the sail inner edge.

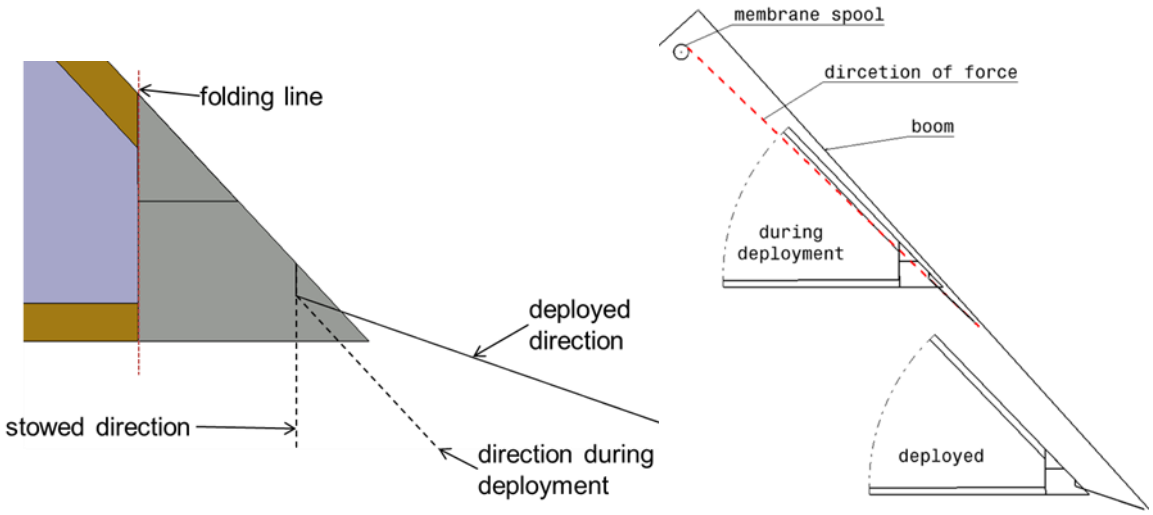


Figure 28: Deployment of the sail. Direction of the right boom – membrane interface.

#### 6.3.1.3 Calculation of the interface lengths

The length of the interfaces is given by the accommodation in the stowed configuration and it is the design driver for the shape of the sail membrane, which needs to ensure that tensioning in the stowed and deployed configuration is possible. For the design, it was assumed that the end of the folded membrane is behind the uncoiling point of the shorter interface (red line, Figure 16) to ensure that everything of the folded sail is coiled on the membrane spool. This leads to a design in which the interface foil covers the complete spool which is calculated in the next section. This is seen to be an advantage because this cover keeps the sail coil under tension and acts as a protection.

In principle it is possible to increase the length and coil this additional length on the spool, this would require increasing the boom length in the deployed configuration or to reduce the sail area.

##### 6.3.1.3.1 Boom – membrane interface

The interface length between the boom interface point and the membrane interface point (see Figure 16 and Figure 26) consist out of different parts, one that is coiled on the spool and one between the boom interface point and the uncoiling point on the sail spool.

The blue line, in Figure 16, is the shorter interface with an unrolled length of 39.85 mm. The lower interface (red line, Figure 16) has an unrolled length of 177.99 mm.

The coiled length of the interface can be calculated, knowing that the outer diameter of the spool is about 76 mm. The distances between the interface connection point at the boom side and the uncoiling point of the shorter interface is given by

$$l_{red,1} = 177.99\ \text{mm} + \pi \cdot 76\ \text{mm} \cdot \frac{162.54°}{360°} = 285.79\ \text{mm}\ , \tag{54}$$

$$l_{blue,1} = 39.85\ \text{mm}\ . \tag{55}$$

The indices, red and blue, are based on the interface colours in Figure 16. To ensure that the interface foil covers the whole membrane spool (plus a small margin), an additional interface length of 124 mm is added to both interfaces. Furthermore, the distance of the membrane interface points to the outer sail edge is set to 14 mm, presented in Figure 29. The distances between the boom connection points and the membrane interface point are calculated as

$$l_{red,2} = l_{red,1} + 14\ \text{mm} + 124\ \text{mm} = 423.79\ \text{mm}\ , \tag{56}$$

$$l_{blue,2} = l_{blue,1} + 14\ \text{mm} + 124\ \text{mm} = 177.85\ \text{mm} \quad . \tag{57}$$

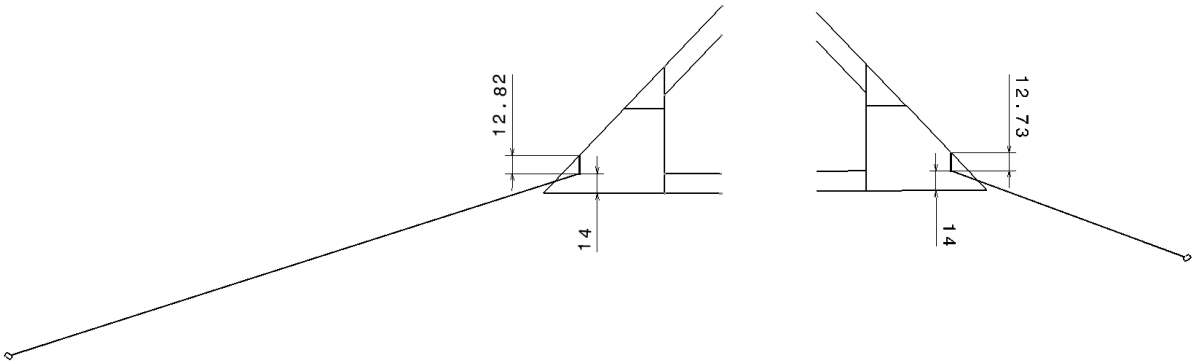


Figure 29: Boom – membrane interface position on the membrane segment including the vertical interface length which is glued on the membrane.

Due to the geometry of the interface design, small additional vertical interface lengths need to be added to the calculation. These small values are the lengths at which the left and right part of each boom – membrane interface are bonded together vertically, presented in Figure 29. The lengths of the interface which are positioned vertically compared to the sail plane in the deployed configuration are calculated by

$$l_{red} = l_{red,2} + 12.73\ \text{mm} = 436.52\ \text{mm} \quad , \tag{58}$$

$$l_{blue} = l_{blue,2} + 12.82\ \text{mm} = 190.67\ \text{mm} \quad . \tag{59}$$

The values from the Equations (58) and (59) are used to estimate how much of the membrane spool is covered by the interfaces in the stowed configuration. Regarding the current accommodation, the sail spool is fully covered with the boom – membrane interface. The long interface (red line in Figure 16) is wrapped 1.08 times around the membrane spool. The shorter one (blue line in Figure 16) in rapped 0.63 times around the spool. It needs to be reminded, that the shorter interface is shifted 162.54° counter clockwise on the spool. If this value is added to the length, the small interface ends up nearly on the same position on the spool which is shown in Figure 16 (“end of both interfaces”).

#### 6.3.1.3.2 Membrane – membrane spool interface

The geometry of the membrane – spool interface is illustrated in Figure 30. It shows the top view of the interfaces and how they are coiled onto the spool. The corner of the sail has 20 mm to the tangential point on the spool diameter. The interface is wrapped 810° around the spool. This ensures an additional interface length of 165 mm which can be rolled off. In case this additional length avoids high forces in the membrane which is caused by a non-exactly deployed length of the boom or a thermal compression of the sail which would decrease the sail length. The last 180° (47 mm) of the coiled interface onto the spool are bonded to the spool with an adhesive.

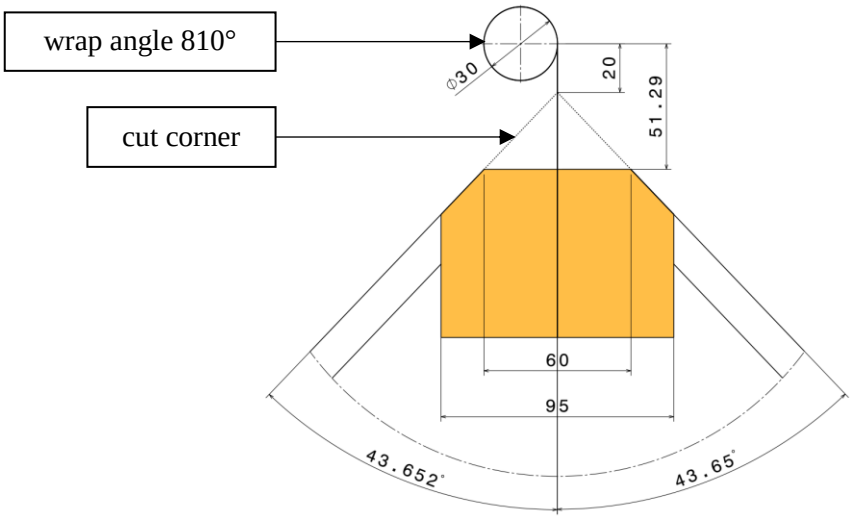


Figure 30: Geometrical values of the spool – membrane interface (orange).

In the deployed configuration of ADEO-2, the membrane plane is shifted 12.5 mm upwards concerning to the middle of the membrane spool height which can be used for coiling the membrane onto the spool, shown in Figure 31. The reason of that is the change of the boom shape during the deployment. To integrate this condition, the first folding line next to the height line of the membrane triangle is 47.5 mm away from the height line. This ensures that the sail can be rolled on the spool.

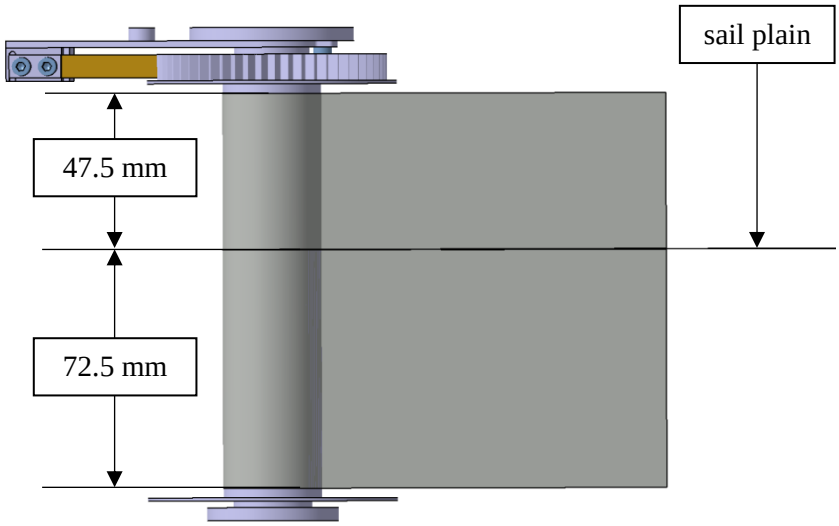


Figure 31: Position of the sail plain in the deployed ADEO-2 configuration.

### 6.3.2 Joining lines

All four sail segments are made of foil stripes. These stripes, depending on the manufacturer, have different widths. In the ADEO-2 project Sheldahl is selected as the supplier for membrane. The width of one foil stripe is 1200 mm as shown in Figure 32. In order to achieve the required sail size three stripes per segment need to be bonded together. These stripes are rectangular orientated to the right inner edge of the triangle. As a first assumption, the foils will have an overlap section with the width of 3 mm.

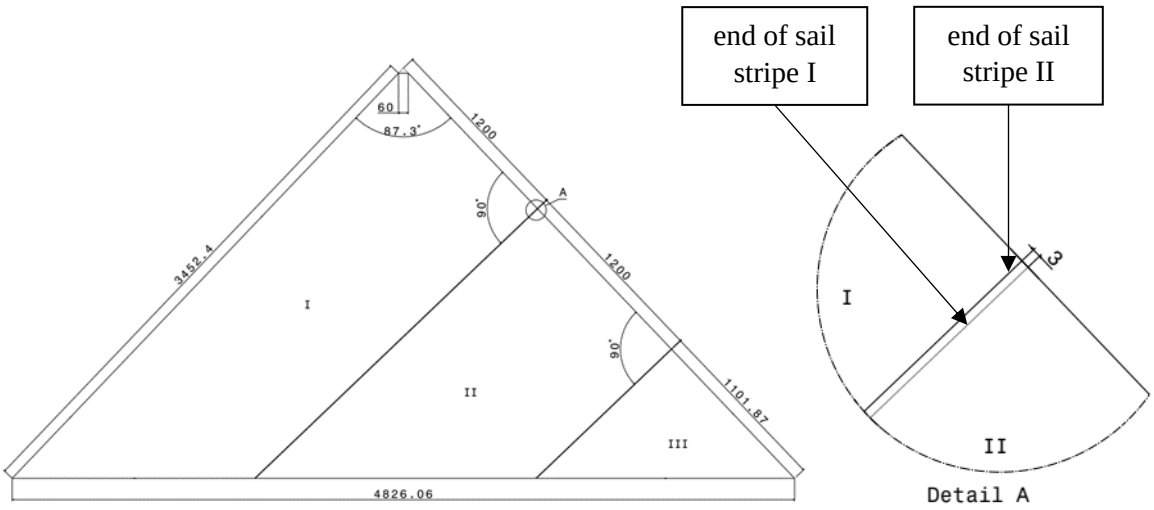


Figure 32: Design of one membrane segment consisting of three foil stripes (left picture); Description of the overlap area between two foil segments (right picture).

In the ADEO-1 design the foil on the top of the bonding area was flipped under the adhesive to ensure that cutting edges of the foil are not exposed to the ATOX and VUV radiation which can cause degradation on the material. Additionally, this bonding technique was used on both sides of the membrane. In contrast to the ADEO-1 design, the foil stripes are only bonded with a tape from one side of the membrane and without any flipping of the foil edges under the adhesive. The layer setup is shown in Figure 33. This change is only to reduce the manufacturing complexity and keep the thickness of the membrane and the coil to a minimum.

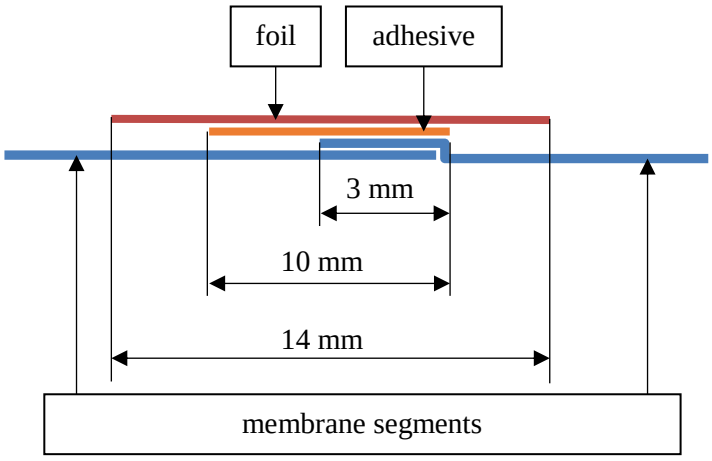


Figure 33: Design of the connection technique of the joining lines.

The high flexibility and small thickness of the joining area are strong benefits.

Furthermore, the aging of the Kapton is investigated. According to [21, p. 9], the erosion yield of Kapton $E_K$ is about $3 \cdot 10^{-24}$ $\left[\frac{\text{cm}^3}{\text{atom}}\right]$. To give a rough overview of the erosion length of the Kapton foil, the atomic oxygen flux $F_{ATOX}$ at an altitude of 500 km with a medium solar activity is about $2 \cdot 10^{13}$ $\left[\frac{\text{atom}}{\text{cm}^2 \cdot \text{s}}\right]$ shown in Figure 34.

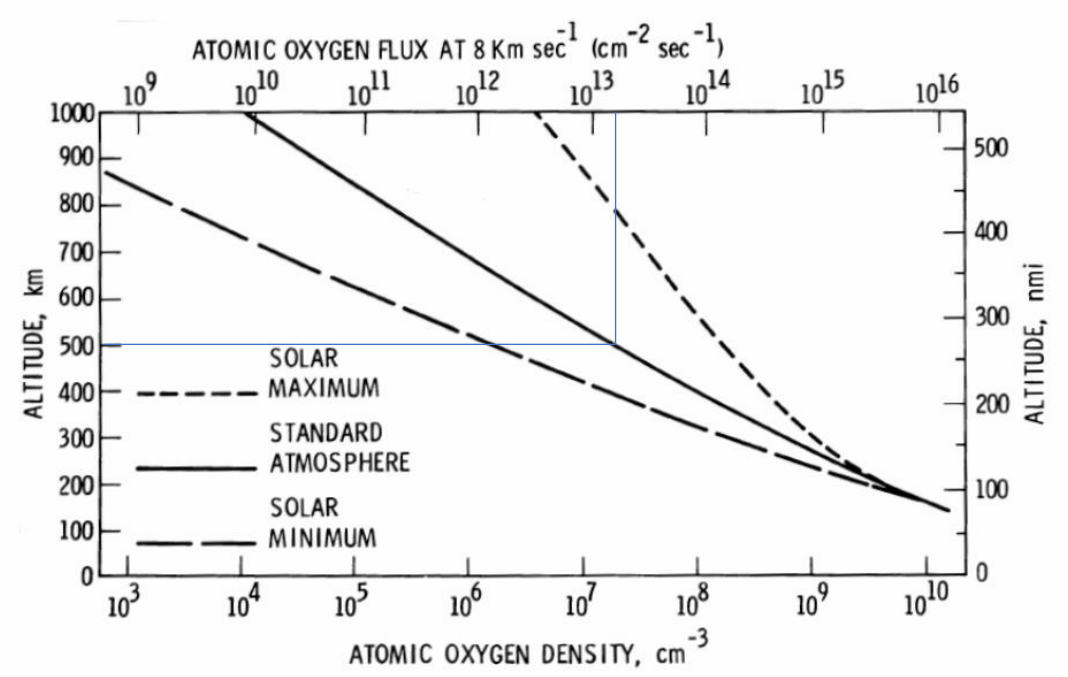


Figure 34: Atmospheric ATOX density and ATOX flux in LEO. [22, p. 13]

The mission time for the deorbit process $t_{DO}$ is set to its maximum of 25 years as a worst-case estimation. The erosion length $l_e$ of the Kapton foil is calculated as

$$l_e = F_{ATOX} \cdot E_K \cdot t_{DO} = 473.04\ \mu\text{m} \tag{60}$$

This value is only representative when no aluminium layer is surrounding the Kapton like it is present on the cut edges of the membrane foil. Additionally, this erosion length is also an estimation for the cut edges of the joining lines, crack stopper and reinforced edges. Due to the calculated erosion length of Kapton the ATOX will not cause much aging on the cutting. To increase the ATOX and VUV radiation resistance another transfer tape which is fixed on the other side of the membrane can be used, but this would decrease the flexibility due to a rise in thickness.

The foil on the top of the adhesive has a width of 14 mm with an adhesive width of 10 mm shown in Figure 35. This tape is symmetric which causes a gap between the edge of the adhesive and the foil of 2 mm to ensure that no adhesive will be squeezed out of the bonding area.

### 6.3.3 Crack stopper

Crack stoppers are thin strips of foil with adhesive which will be bonded on to the surface of the membrane to prevent crack propagation through the whole membrane. The crack stoppers have the same dimensions as the tape used for the bonding of the foil sheets (14mm with 10mm adhesive) also shown in Figure 35. The positions of the crack stoppers are presented in Figure 36.

### 6.3.4 Reinforced edges

The reinforcement of the membrane edges is important to prevent the possibility of crack initiations on cut edges. Figure 36 shows the orientation and position of the joining lines, crack stoppers and reinforced edges.

Furthermore, cracks which appear on the inner area of the membrane, caused for example by micro meteorites or space debris impacts, cannot propagate throughout the sail edge. Therefore, it is ensured

that a “frame” around the sail segment stays intact. The main loads will distribute in the areas in which the reinforced edges, crack stoppers and joining tapes are present and will reduce the stress in the membrane itself.

The reinforced edges are built with the same tape used for the crack stoppers and the joining lines (14mm with 10mm adhesive) which is shown in Figure 35.

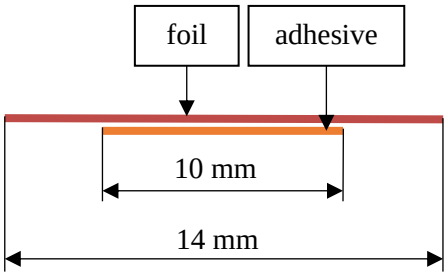


Figure 35: Adhesive tape for crack stoppers, joining line and reinforced edges.

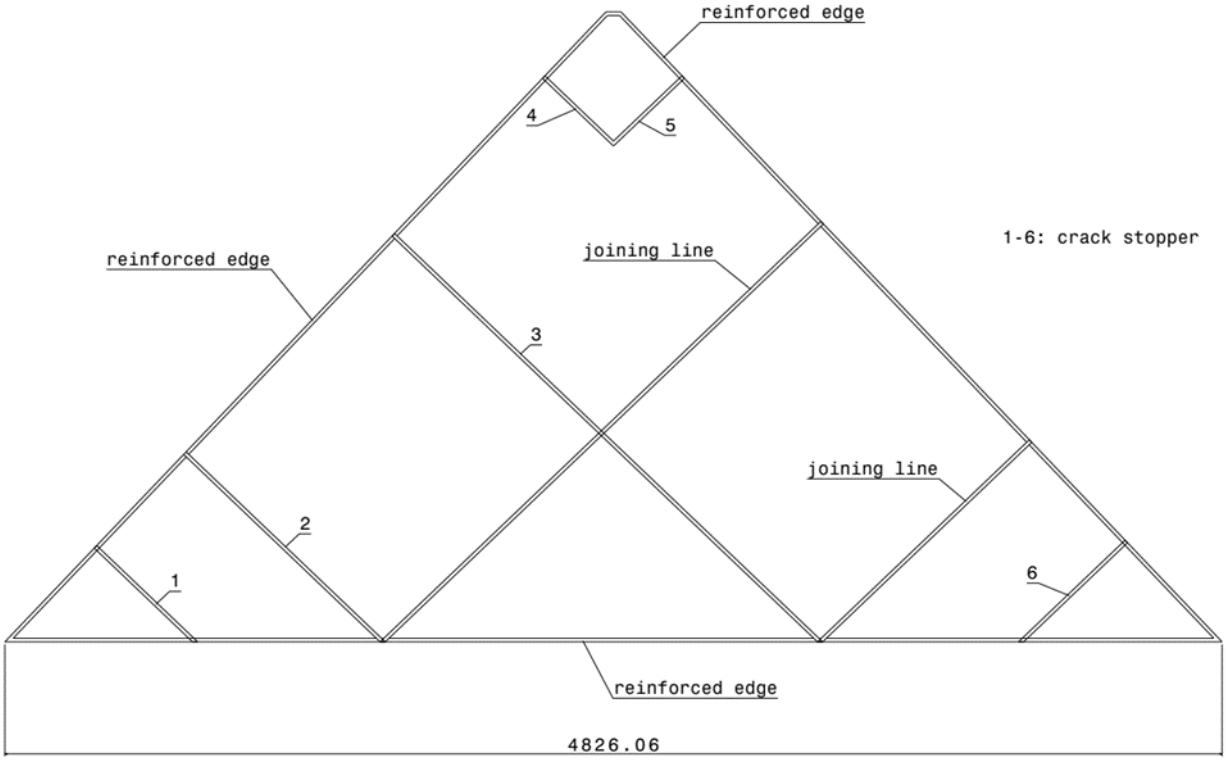


Figure 36: Sail segment with reinforced edges, crack stoppers and joining lines.

# 7 Membrane spool

As explained in Section 5 and shown in Figure 13, the sail is folded and coiled onto four spools. The spool mechanism is described in the following sections.

## 7.1 Requirements and assumptions

The following subsections lists system requirements that influence the design as well as assumptions that are specific for this component.

### 7.1.1 General system requirements

According to [20, p. 16-20], relevant system requirements that need to be considered for the design of the membrane spool are:

- „The ADEO subsystem shall withstand…" the rapid decompression during the lunch "…without any damage" (PFM-ENV4).
- "The ADEO subsystem shall be compatible with the following storage requirements: 3year storage on ground, 6 months storage during launch phase, and 15 year storage in-orbit" (PFM-ENV5).
- "The ADEO subsystem shall withstand the maximum sun illumination/eclipse of the mission in stowed and deployed configuration" (PFM-ENV6).
- "The mass of the ADEO subsystem shall be not greater than 5% of reference mission S/C" (PFM-DF2).
- "The size of the ADEO subsystem shall not be larger than 500 mm x 500 mm x 200 mm (H x W x L)" (PM-DF3). Therefore, the whole spool assembly shall have a maximum height of 150 mm (axial length) to ensure that the requirement in PFM-DF3 will be respected.
- "Unless commanded, the subsystem shall not deploy under lunch or S/C operational loads" (PFM-DF4).
- "The ADEO subsystem shall stop the dragsail deployment by itself once the booms are full deployed" (PFM-DF8).
- "The subsystem shall provide launch locks" (PFM-DF11).
- "All parts and materials used in the ADEO subsystem should be ITAR free" (PFM-DF14).
- "The ADEO subsystem shall have a first eigenfrequency of 140 Hz or higher" (PFM-DF15).
- "The ADEO subsystem shall not be vacuum sealed" (PFM-DF16).

### 7.1.2 Further assumptions

This subsection describes the subsystem assumptions of the membrane spool.

Subsystem assumptions are:

- The whole spool assembly shall be stand-alone integrate able and testable which supports a modular design of ADEO-2 and thereby AIV/AIT efforts.
- The outer diameter of the spool shall be 76 mm which is an estimation of the maximum coiling diameter of the sail based on pre-tests (see Section 7.1.3).
- The axis of the spool shall be designed as load-bearing element that supports the overall structural integrity of ADEO-2.
- Spool brakes shall prevent premature uncoiling of the sail which is necessary for the requirement in PFM-DF8.
- The coiling of the sail on-to the spool shall be possible without disassembling the spool brake for an easy integration and testing.

### 7.1.3 Pre-test for the packaging size estimation

This section shows pre-tests carried out with sail segments built in former DLR projects with a 7.6 µm Upilex-S foil coated with 100 nm aluminium on both sides. The sail segment with about 6.25 m$^2$ was coiled on a spool with an inner diameter of 35 mm with a folding width of 135 mm as shown in Figure 37. The outer diameter $D$ for this configuration is evaluated and used to extrapolate to other configurations with different inner diameters $d$ or folding width $k$.

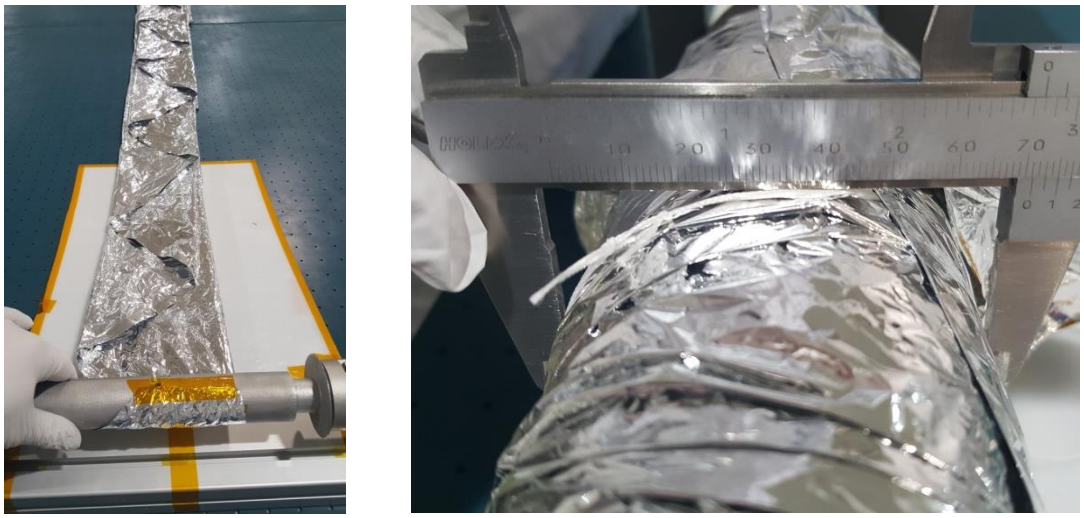

Figure 37: Folded membrane before rolling up on spool (left picture) and outer diameter of the membrane (spool) (right picture). [curtesy DLR]

The values of the minimum outer spool diameter $D$ caused by the rolled-up thickness of the membrane with different membrane fold distances $k$ and membrane thicknesses are shown in Table 3. The outer spool diameter with only the material thickness is calculated by

$$D = \sqrt{d^2 + \frac{4 \cdot V_{material}}{\pi \cdot k}} \tag{61}$$

with the measured sail membrane volume calculated with the membrane thickness $t_{foil}$ and the surface area of one sail segment $A_{norm}$. The measured sail membrane volume is

$$V_{material} = t_{foil} \cdot A_{norm} = 4.875 \cdot 10^{-5}\ \mathrm{m}^3 \quad . \tag{62}$$

Table 3: Packaging size estimation only considering the material thickness. The pre-tested design is highlighted in green.

| D [mm] | | | | | | |
|---|---|---|---|---|---|---|
| | | | k [mm] | | | |
| d [mm] | 100 | 110 | 120 | 130 | 135 | 150 |
| 20 | 31.94846284 | 31.052804 | 30.286194 | 29.62203283 | 29.322022 | 28.52723 |
| 25 | 35.29453609 | 34.48589 | 33.797242 | 33.20338581 | 32.936013 | 32.230465 |
| 30 | 38.99620851 | 38.265868 | 37.646428 | 37.11421331 | 36.875208 | 36.246418 |
| 35 | 42.96166056 | 42.299842 | 41.740311 | 41.26093587 | 41.046083 | 40.48213 |
| 40 | 47.1243491 | 46.521786 | 46.013624 | 45.57921488 | 45.38481 | 44.875415 |

The measured outer spool diameter $D_{measured}$ in the pre-test was 71.15 mm (see Figure 37, right picture). The measured volume is calculated, for the configuration, which was current during the pre-tests, as

$$V_{measured} = \frac{\pi}{4} \cdot \left( {D_{measured}}^2 - d^2 \right) \cdot k = 4.06867 \cdot 10^{-4}\ \mathrm{m}^3 \quad . \tag{63}$$

To transfer the measured outer diameter to values with different inner spool diameters, a filling factor that puts the measured volume in relation to the material volume is calculated by

$$F = \frac{V_{measured}}{V_{material}} = \frac{4.06867 \cdot 10^{-4}\ \mathrm{m}^3}{4.875 \cdot 10^{-5}\ \mathrm{m}^3} = 8.34598 \quad . \tag{64}$$

By adding the filling factor $F$ to Equation (61), the outer diameter is

$$D = \sqrt{d^2 + \frac{F \cdot 4 \cdot V_{material}}{\pi \cdot k}} \quad . \tag{65}$$

The resulting outer diameters for different configurations are given in Table 4.

Table 4: Estimated outer diameter $D$ of the sail spool for different folding width $k$ and inner diameter $d$. The current design configuration for ADEO-2 is highlighted in green.

| D [mm] | | | | | | |
|---|---|---|---|---|---|---|
| | | | k [mm] | | | |
| d [mm] | 100 | 110 | 120 | 130 | 135 | 150 |
| 20 | 74.70197705 | 71.4803557 | 68.6803306 | 66.2186668 | 65.0947194 | 62.0772925 |
| 25 | 76.19307957 | 73.0372593 | 70.2992732 | 67.8963315 | 66.8006175 | 63.8638415 |
| 30 | 77.97682588 | 74.8962032 | 72.2287188 | 69.8921442 | 68.8282101 | 65.9817418 |
| 35 | 80.03365152 | 77.0353247 | 74.4445284 | 72.1797189 | 71.15 | 68.4002211 |
| 40 | 82.34309549 | 79.4319914 | 76.9219592 | 74.7322676 | 73.7382024 | 71.0886084 |

It should be noticed that the outer diameter depends strongly on the coiling torque. The sail segment was coiled with DLR's Gossamer-1 mechanical ground support equipment (MGSE) that allows setting a constant coiling torque, here 0.105 Nm. This corresponds to 6 N coiling forces on the inner diameter of 35 mm. With this setting, the above described values were achieved. It needs to be considered that during the stowing of the sail, the radius increases. With a constant coiling torque, the force at which the membrane is pulled onto the spool decreases which leads to a less tight package in the outer coiling diameters. When increasing the torque to 0.175 Nm during the last two rotations, the outer diameter decreased around 5 mm. This corresponds to about 5 N applied on the sail coil.

Taking these estimations into account and considering some extra margin for interfaces, the spool diameter for the preliminary design is 76 mm. This mainly impacts the diameter of the flanges of the spool. Depending on the results of the bread board design and tests, this diameter can be easily adapted if necessary.

## 7.2 ADEO-2 spool design

In this section the preliminary design of the ADEO-2 sail spool assembly is described more detailed.

The assembly consists of the spool itself that is rotating with two journal bearings on an axis. The deployment, especially premature uncoiling due to elastic deformation of the membrane material, is controlled with a brake that counteracts these elastic forces. Furthermore, the spool provides the counterpart for the launch lock that is part of the Hold Down and Release Mechanism which is developed by HPS/RUAG. Figure 38 and Figure 39 provide an overview of the design.

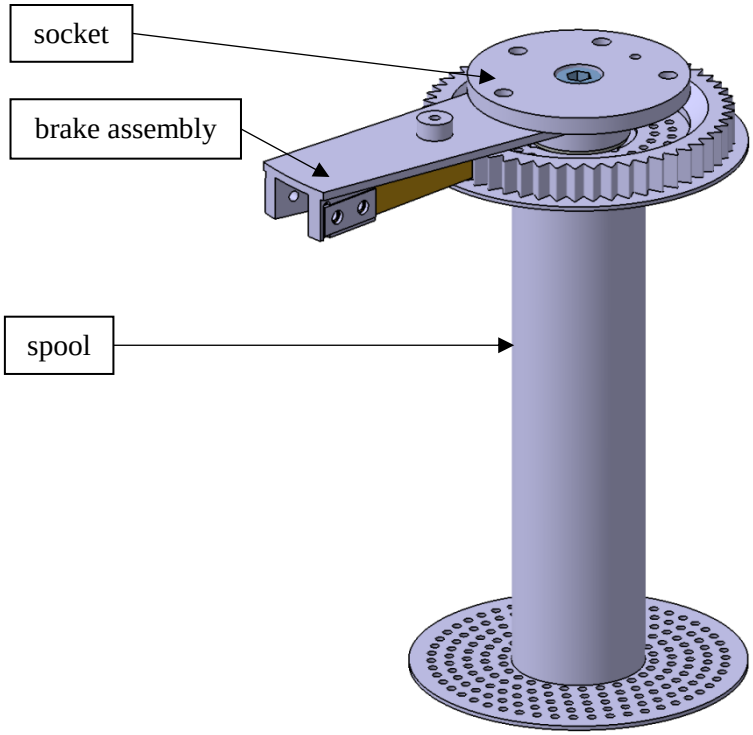


Figure 38: Membrane spool without launch lock and screws on the brake.

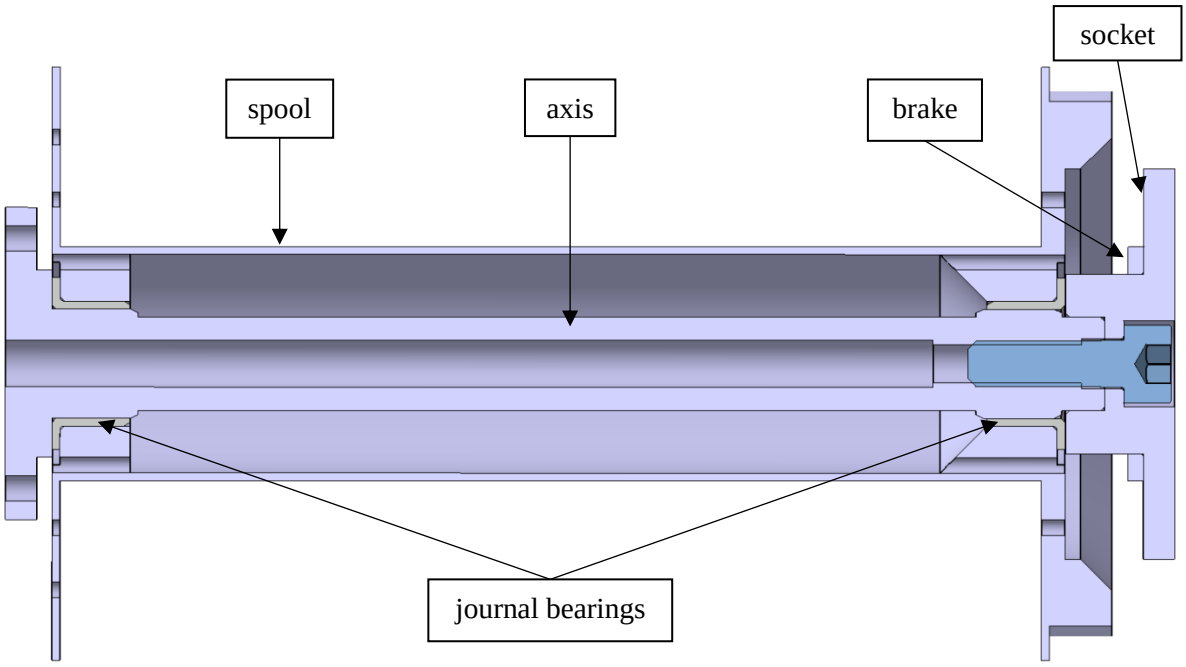

Figure 39: Sectional view of the membrane spool design with journal bearings.

The axis, socket, spool and parts of the brake are made from aluminium. The journal bearings consist of iglidur X which is a special material of the company Igus. The spring for the brake is made of copper-beryllium and the screws used in the ADEO-2 configuration are made of stainless steel. All materials can be used in the LEO environment without any issues. Thereby, requirement PFM-ENV5, presented in Section 7.1, is confirmed. The range of the thermal cycles of the membrane spool will not be as high as the temperature range of the membrane, in the deployed configuration, due to the heat capacity of the materials. The temperature during the mission will be between the calculated ones which are presented in Section 4. All above mentioned materials can be used in this temperature range. Therefore, requirement PFM-ENV6 from Section 7.1 is respected. Additionally, all used materials are ITAR free which confirms requirement PFM-DF14, shown in Section 7.1.

### 7.2.1 Spool

The spool consists of the cylinder on which the membrane is mounted and coiled as well as a gear in which a spring engages and provides thereby an oscillating brake torque. Additionally, the gear is used by a launch lock which avoids the rotation of the spool during the launch and the satellite's lifetime, required in PFM-DF4 and PFM-DF11. It will be released after the lifetime of the satellite. The spool does not have to carry any loads except the acceleration loads due to the inertia of the spool and the sail segment. In order to save mass, the complete spool with the gear is produced by Additive Layer Manufacturing. The Material is AlSi10Mg. Figure 40 and Figure 41 show the spool design.

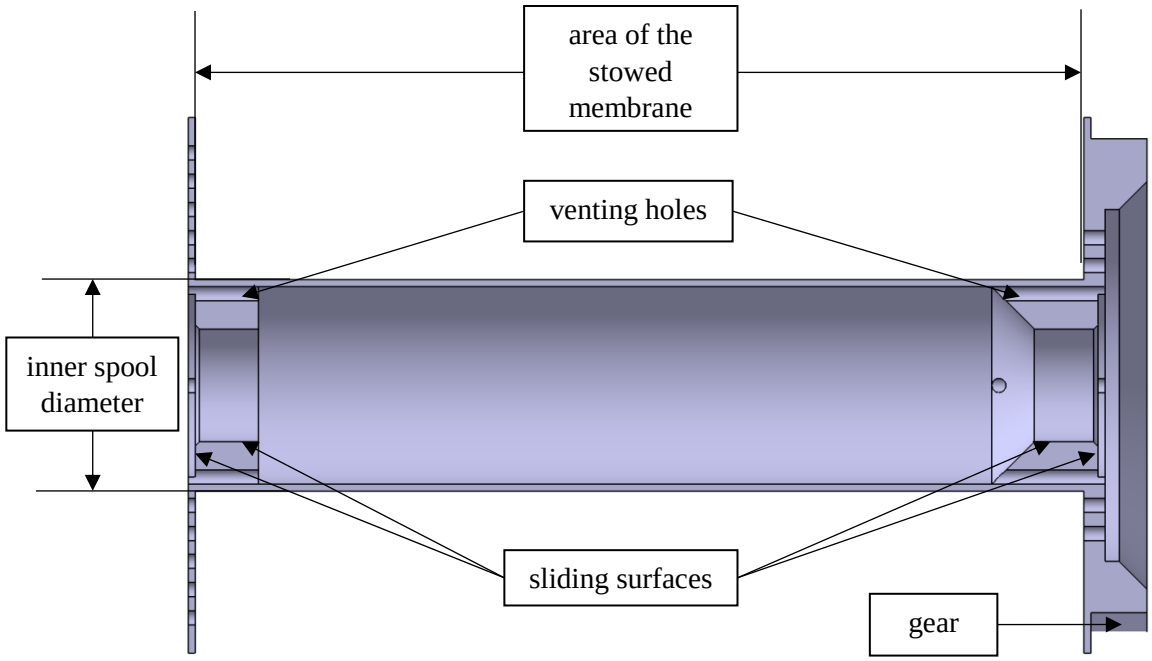


Figure 40: Sectional view of the membrane spool.

A total of eight venting holes are included to depressurize the inner area of the membrane spool assembly (requirement PFM-DF16). The sliding surfaces for the bearing will be post-processed in order to ensure tolerances and surface properties. The flanges on each side could provide additional support to the coiled segment and act as a protective cover as well as guidance during deployment. The distance which can be used has a width of 125.9 mm. To ensure that after folding and flattening the membrane fits onto this area, the membrane folding width should not be larger than 120 mm.

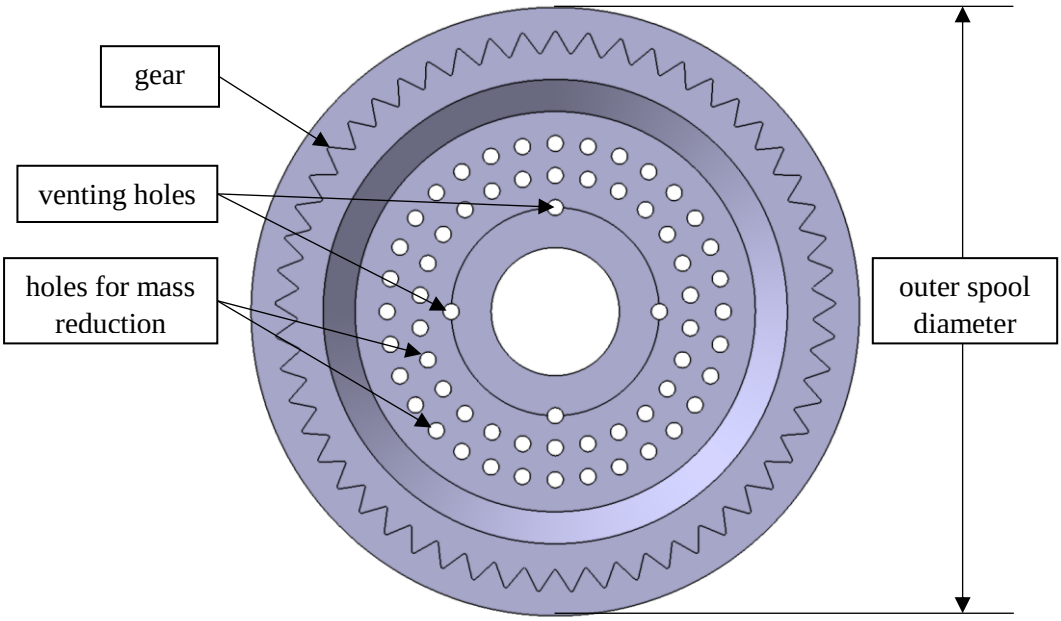


Figure 41: Top view of the membrane spool.

### 7.2.2 Axis

Figure 42 and Figure 43 show the axis assembly. The complete axis consists of two parts. Part one is called “axis” which represents the main structure of the complete axis assembly. It is a hollow cylinder with an inner thread on the left side (Figure 42). Part 2 is the socket which is presented in Figure 43. Both parts must be separated to be able to mount the bearing, spool and brake onto the axis. An M6 screw is used to install the socket after assembling the bearings and the spool. In addition, the spring holder from the brake is mounted to the socket.

The axis assembly is the main distance holder and a load path between the bottom plate and the upper part of ADEO-2. Therefore, these parts are machined out of Al7075 T6. Depending on the accommodation, the length of the spool can have very tight tolerances if required.

The socket is aligned on the axis with fitting surfaces that avoid jamming of the parts and provide a tolerance for the overall length of the axis assembly. The countersink drilling hole is designed such that an ISO 4762 – M6 screw head fits in it. The countersink is required to ensure that the screw head is not intersecting with other parts on the upper side of ADEO-2. The axis assembly is mounted on both sides with four M5 screws on the ADEO-2 structure.

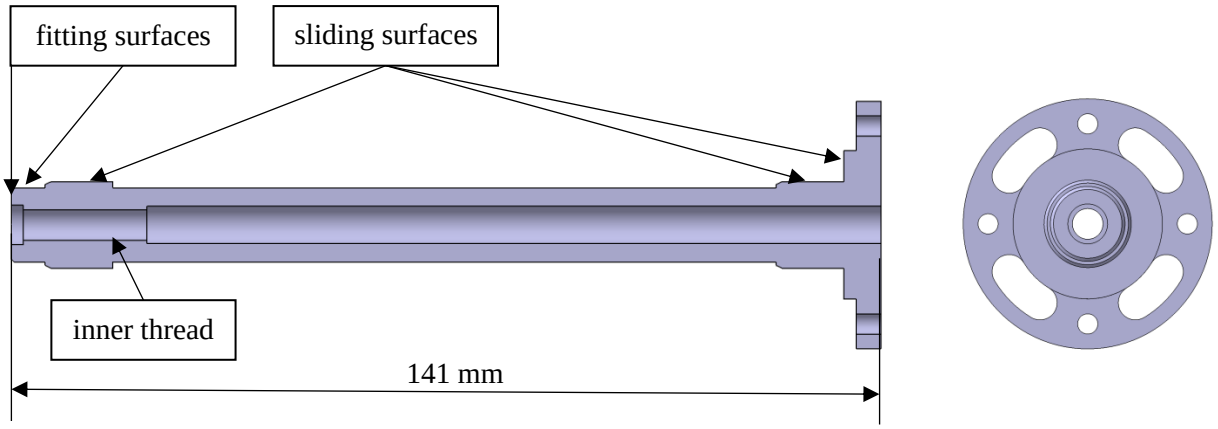


Figure 42: Sectional view (left picture) and top view (right picture) of the axis.

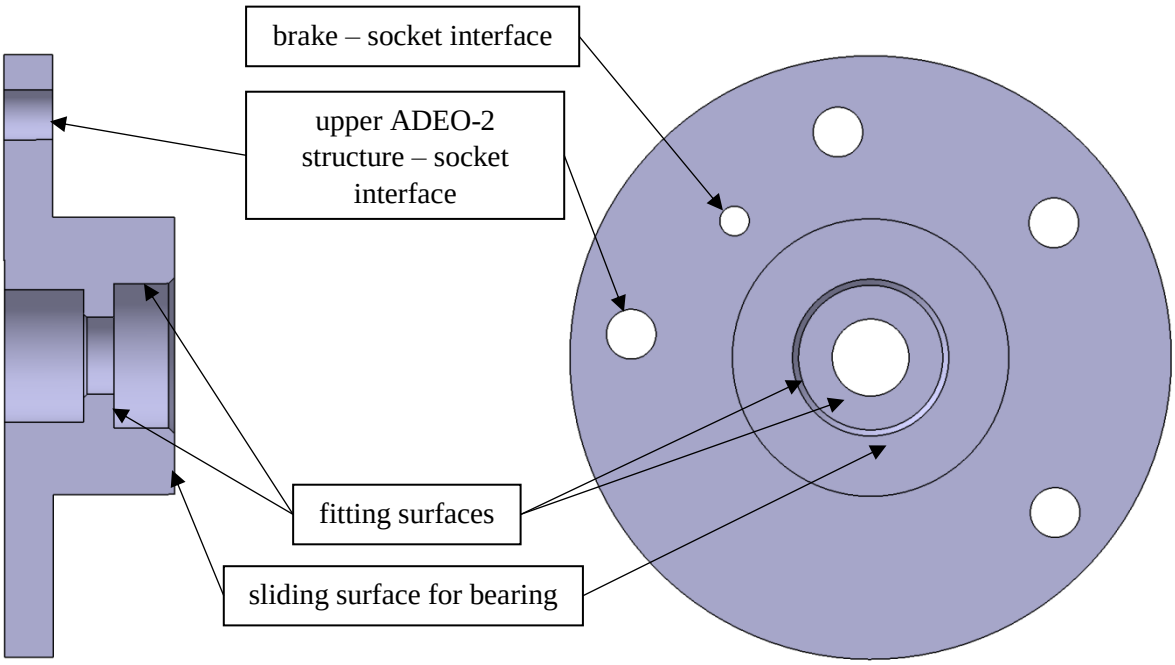


Figure 43: Sectional view (left picture) and bottom view (right picture) of the socket including description about interfaces and contact/slide surfaces.

### 7.2.3 Brake assembly

The brake is used to produce a defined torque which avoids a self-deployment due to elastic stored energy. During the deployment, this counter torque ensures a deployment which is always under tension, such that the membrane and interfaces do not have much slack and thereby reduce the risk of an entanglement with other parts. In the deployed configuration, the brake defines the position of the membrane – membrane spool interface. In case a tension load is getting higher than the brake force (e.g. due to thermo-elasticity deformation), additional interface length is released. This avoids high tension loads in the membrane which have a negative effect on crack propagation as well as high loads transferred to the booms. Figure 44 shows the whole brake assembly (without screws).

The brake is made as springs that interacts with a gear on the sail spool. In the current ADEO-2 design, the spring is mounted parallel to the engaging depth. More than one spring is used to reduce the bending stress in the material at the same general required torque which is shown in the calculation below. Two springs made of copper-beryllium are used to achieve a brake torque that is equal to the coiling torque.

The springs are mounted to a holder with M3 screws and small plates which have a better load distribution than the screws itself. Moreover, the small plates as well as the holder interact as a fixed clamping at which the bending deformation starts. The spring holder is fixed with one screw on the socket and one to the upper part of ADEO-2. Furthermore, to guarantee the right position, the huge drilling hole fits exactly on one circumference of the socket. The spring holder is machined out of Al7075 T6. Additionally, there is a through hole (M5) between the springs and the fitting hole. This hole is necessary to avoid contact to a M5 screw which fixes the socket on the upper ADEO-2 structure.

Furthermore, a bending stress calculation is made to estimate the stress in the spring of the brake. There should only be an elastically deformation to ensure at any time a defined torque interval and no risk of fractures in these plates. Furthermore, the resulting torque of the brake needs to be known to estimate the deployment forces and to evaluate if the torque is high enough to avoid a self-uncoiling of the membrane.

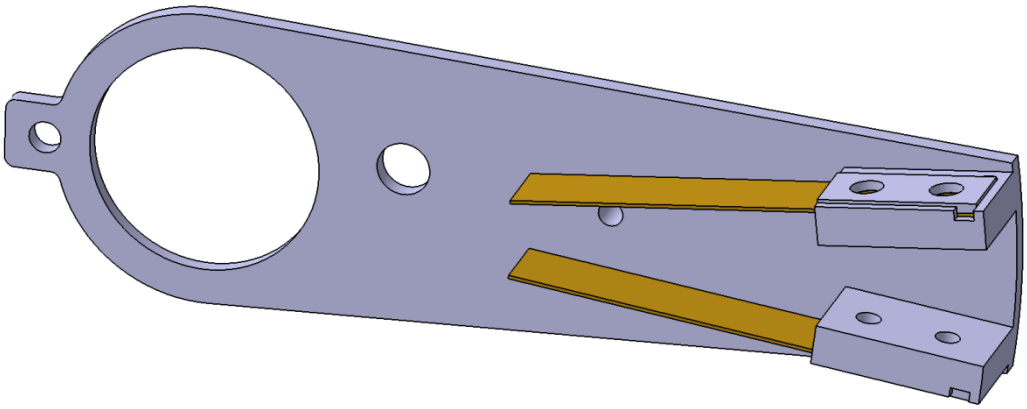

Figure 44: Brake assembly without screws.

The following Table 5 contains boundary conditions which are necessary for the brake calculation.

Table 5:Values of the brake.

| Paprameter | Symbol | Value | [Unit] |
|---|---|---|---|
| Young's modulus | $E$ | 131 | [GPa] |
| Spring width | $w_s$ | 7 | [mm] |
| Spring length | $l_{Spr}$ | 31 | [mm] |
| Spring thickness | $t_s$ | 0.3 | [mm] |
| Number of Springs | $n_s$ | 2 | |
| Spool radius (old) | $r_i$ | 17.5 | [mm] |
| Number of gear teeth | $n_z$ | 53 | |
| Gear outer radius | $R$ | 35 | [mm] |
| Gear enganging depth | $\Delta z$ | 1.5 | [mm] |

As mentioned before, the springs are made of copper-beryllium. According to [15], the material has a Young's modulus of about 131 GPa, shown in Table 5. The spring length is just the length which can bend. An additional length is added to fix these springs on the spring holder.

First, the minimum required torque is calculated to prevent that the brake is too weak and the spool would unroll the sail to a certain undefined state. Furthermore, if the brake is too strong, the deployment forces would be too high which can damage the membrane and the booms.

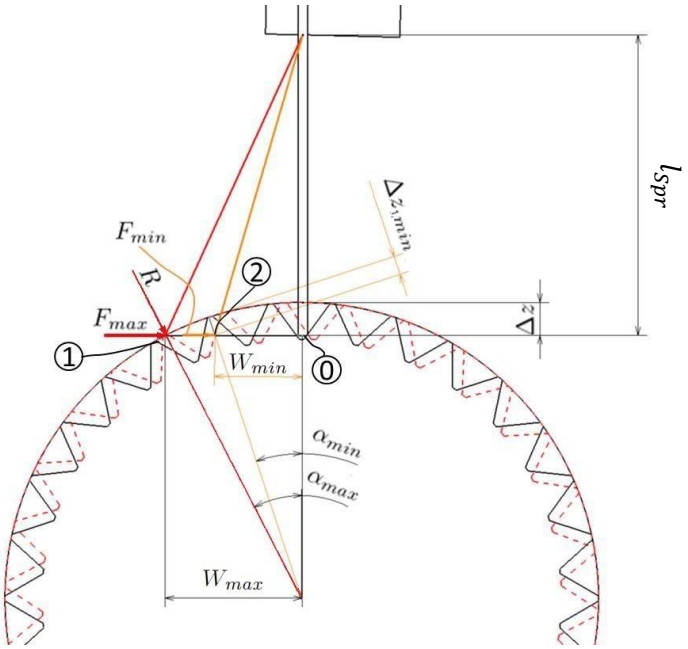


Figure 45: Simplified geometry of the brake, consisting of a spring that engages a gear. The red dashed line represents the position at which the spring snaps back to the next gear tooth. [16]

The measured force $F_{measured}$ with which the membrane is rolled onto the spool at the start of the stowing process is 6.06 N (measured during coiling tests). With the inner spool radius $r_i$ of 17.5 mm the coil torque $T_{coil}$ is calculated by

$$T_{cal} = F_{measured} \cdot r_i = 0.10605 \text{ Nm} \quad . \tag{66}$$

The requirement for the torque is

$$T_{coil} < T_{b,max} \quad . \tag{67}$$

Additionally, the spring forces and the resulting torque needs to be determined. The following equations, used for the spring force and torque calculation, are based on Figure 45 and [16]. The geometrical values necessary for the torque calculation are:

$$\alpha_{max} = cos^{-1}\left(\frac{R - \Delta z}{R}\right) = 0.29383 \text{ rad} \quad , \tag{68}$$

$$u_{max} = R \cdot \alpha_{max} = 10.28390 \text{ mm} \quad , \tag{69}$$

$$p_G = \frac{2 \cdot \pi \cdot R}{n_z} = 4.14927 \text{ mm} \quad , \tag{70}$$

$$u_{min} = u_{max} - p_G = R \cdot \alpha_{min} = 6.13463 \text{ mm} \quad , \tag{71}$$

$$\alpha_{min} = 0.17528 \text{ rad} \quad , \tag{72}$$

$$W_{min} = \tan(\alpha_{min}) \cdot (R - \Delta z) = 5.93260 \text{ mm} \quad , \tag{73}$$

$$W_{max} = \sqrt{R^2 - (R - \Delta z)^2} = 10.13657 \text{ mm} \quad . \tag{74}$$

Figure 46 shows the moment of inertia of the spring which is needed for the calculation of the force.

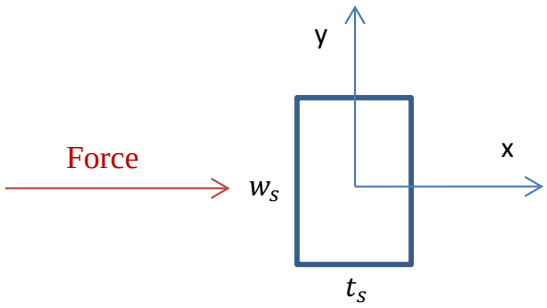


Figure 46: Description of the measurements for the moment of inertia of the spring brake.

According to [23], the moment of inertia of the spring is

$$I_y = \frac{{t_s}^3 \cdot w_s}{12} = 0.01575 \text{ mm}^4 \quad . \tag{75}$$

Finally, the forces and the momentums can be calculated as

$$F_{b,min} = \frac{3 \cdot E \cdot I_y}{{l_{Spr}}^3} \cdot W_{min} \cdot n_s = 2.46526 \text{ N} \quad , \tag{76}$$

$$F_{b,max} = \frac{3 \cdot E \cdot I_y}{{l_{Spr}}^3} \cdot W_{max} \cdot n_s = 4.21220 \text{ N} \quad , \tag{77}$$

$$\Delta z_{min} = R - \frac{R - \Delta z}{\cos(\alpha_{min})} = 0.97875 \text{ mm} \quad , \tag{78}$$

$$R_{min} = R - \Delta z_{1,min} = 34.02125 \text{ mm} \quad , \tag{79}$$

$$T_{b,min} = R_{min} \cdot F_{b,min} = 0.08387 \text{ Nm} \quad , \tag{80}$$

$$T_{b,max} = \text{R} \cdot F_{b,max} = 0.14743 \text{ Nm} \quad . \tag{81}$$

The requirement from Equation (67) is confirmed with these values. Furthermore, the friction is not included in the calculation. The friction increases the torque which is an additional safety.

The next step is to investigate the stress of the spring. It is important that the spring blade stays in the elastic range. This is taken into consideration by

$$R_{p0,2} \geq S_F \cdot \sigma_{b,max} \quad . \tag{82}$$

$S_F$ is the safety factor which compares the stresses of the springs $\sigma_{b,max}$ to the yield strength of the material $R_{p0,2}$. The modulus of resistance against bending is calculated as

$$W_{by} = \frac{w_s \cdot {t_s}^2}{6} = 0.105 \text{ mm}^3 \quad . \tag{83}$$

The maximum bending moment for each spring is given by

$$M_{b,max} = \frac{F_{b,max} \cdot l_{Spr}}{n_s} = 0.06529 \text{ Nm} \quad . \tag{84}$$

In conclusion, the maximum bending stress caused by the brake is calculated as

$$\sigma_{b,max} = \frac{M_{b,max}}{W_{by}} = 621.801 \text{ MPa} \quad . \tag{85}$$

The maximum bending stress is under the yield strength which is between 1100 MPa and 1380 MPa [15]. As a result, two springs are used to reduce the stress in the springs and to avoid plastic deformations. The calculated safety factor is at least

$$S_F = \frac{R_{p,0.2}}{\sigma_{b,max}} = 1.7691 \quad . \tag{86}$$

The maximum deployment force $F_{d,max}$ is influenced by the maximum brake torque $T_{b,max}$ and the minimum coiling diameter $r_{i,min}$, which is reached by the end of the deployment, on the sail spool and is calculated as

$$F_{d,max} = \frac{T_{b,max}}{r_{i,min}} = 9.829 \text{ N} \tag{87}$$

Due to the decreasing coiling diameter of the membrane spool, the deployment force is increasing during the deployment process to $F_{d,max}$. The resulting deployment force should be low enough to avoid cracks in the membrane and interfaces and high enough to span the sail without much slag.

### 7.2.4 Bearing

Journal bearings are used to allow a rotation of the spool on the axis. They are made of iglidur X because of the high temperature resistant range (-100°C to 250°C [24]). Figure 47 shows the different sliding surfaces of the journal bearing. There are always two vertical and horizontal sliding surfaces to ensure that all axial and radial forces can be supported by these bearings and to ensure a redundancy of the bearing. Igus is one of the companies which produce such standardized journal bearings, but they are normally pressed in a housing. This would prevent the redundancy of the sliding surfaces. Therefore, customized journal bearings are manufactured for ADEO-2.

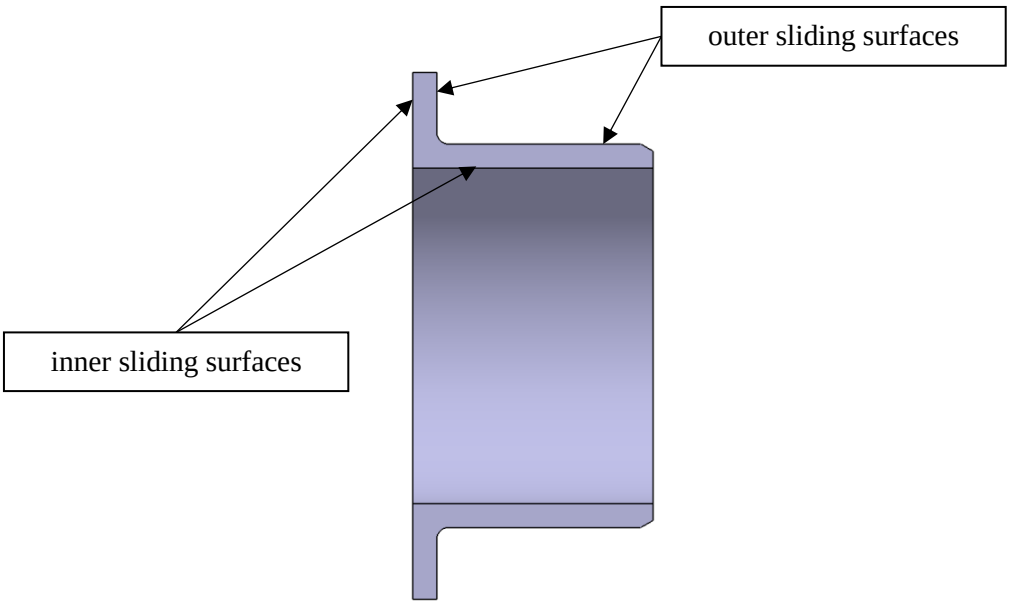


Figure 47: Sectional view of the journal bearing.

## 7.3 Tolerance analysis

The tolerance analysis covers three different cases:

- bearing of the sail spool
- spring engaging into gear
- total tolerance of the membrane spool assembly

### 7.3.1 Bearing tolerance of the membrane spool

The radial and axial position differences between the journal bearings of the axis shall not lead to a clamping of the spool rotation.

#### 7.3.1.1 Radial tolerances of a single journal bearing

The influence of the diameter tolerances for one side of the bearing have been investigated in order to ensure functionality of the assembled parts. The tolerances which must be considered for the bearing tolerance chain in radial orientation, shown in Figure 48, are:

- the diameters, $d_{B,a}$ and $d_{B,i}$, of the journal bearing
- the axis diameter $d_A$
- the spool sliding surface diameter $d_S$

- $d_{B,a} = 16\ h9 = 16^{0}_{-0.043}$
- $d_{B,i} = 14\ F9 = 14^{+0.059}_{+0.016}$
- $d_A = 14\ d9 = 14^{-0,05}_{-0.093}$
- $d_S = 16\ D10 = 16^{+0.12}_{+0.05}$

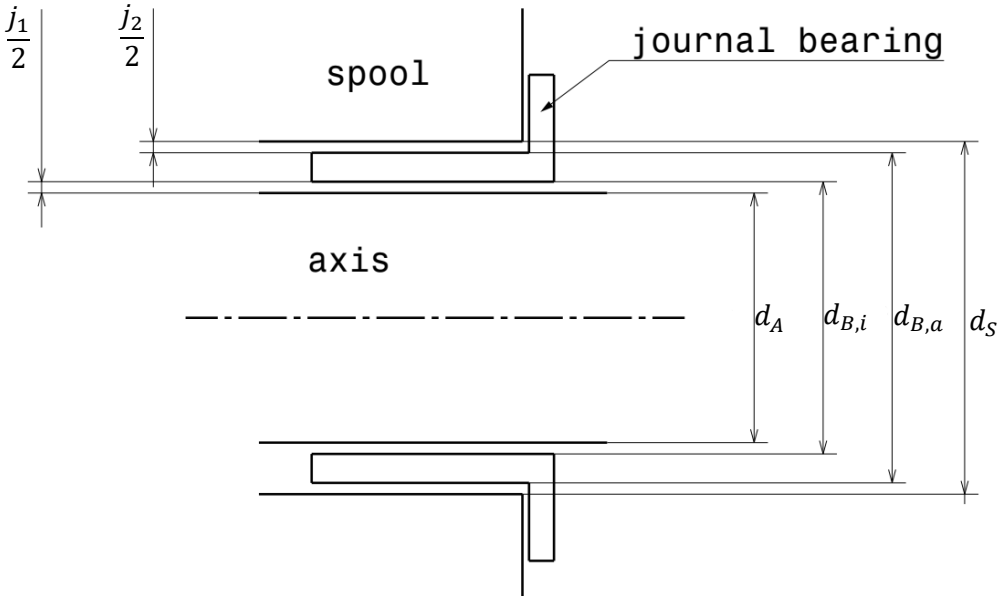


Figure 48: Diameters with tolerances between axis, journal bearing and spool.

These dimensions show that each part will fit into the next larger part. The smallest clearance $j_{min}$ at one bearing joint of the axis (without any concentrically tolerances), which is the result of the combination of the single tolerances, is calculated as

$$j_{min} = j_{1,min} + j_{2,min} \quad , \tag{88}$$

$$j_{1,min} = d_{B,i,min} - d_{A,max} = 0.066 \text{ mm} \quad , \tag{89}$$

$$j_{2,min} = d_{S,min} - d_{B,a,max} = 0.05 \text{ mm} \quad , \tag{90}$$

$$j_{min} = d_{B,i,min} - d_{A,max} + d_{S,min} - d_{B,a,max} = 0.116 \text{ mm} \quad . \tag{91}$$

$j_{1,min}$ is the minimum clearance between axis and journal bearing. The minimum clearance between the journal bearing and the spool is $j_{2,min}$. Furthermore, the maximum radial clearance $j_{max}$ of the bearing is calculated to ensure a well-functioning bearing without jamming. The maximum clearance is

$$j_{max} = d_{B,i,max} - d_{A,min} + d_{S,max} - d_{B,a,min} = 0.315 \text{ mm} \quad . \tag{92}$$

According to the low revolution speed and small amount of revolutions, this maximum clearance which is high compared to general journal bearings clearances should not affect to a problem.

#### 7.3.1.2 Definition of the concentric tolerances of the axis and spool

The sum of the concentric tolerances of the spool and the axis shall not exceed $t_{min}$. Therefore, the concentric tolerance of the spool $j_3$ and the concentric tolerance of the axis $j_4$ are 0.05 mm. Both cases of the concentric tolerances are shown in Figure 49 and Figure 50.

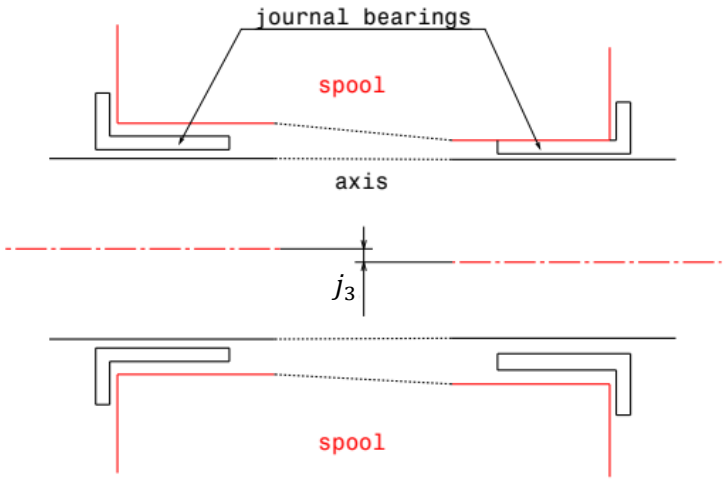


Figure 49: Concentric tolerance of the sliding surfaces of the spool which have contact to the bearing.

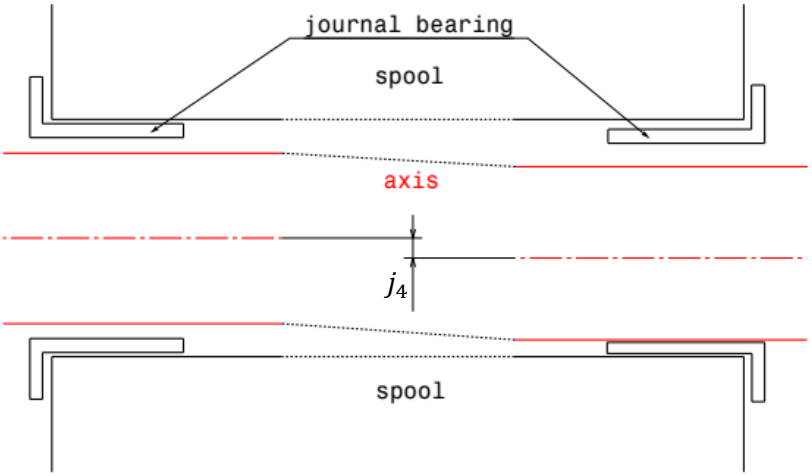


Figure 50: Concentric tolerance of the sliding surfaces of the axis which have contact to the bearing.

The subtraction of $j_3$ and $j_4$ from $j_{min}$ results in a minimum clearance of 0.016 mm, which is considered to be sufficient.

#### 7.3.1.3 Definition of the axial tolerances of the spool assembly

The values and tolerances of the axis, $l_{A1}$ and $l_{A2}$, spool $l_S$, bearing $l_{Be}$ and socked $l_{So,1}$ lengths are:

- $l_{A1} = 141^{+0.15}_{+0.05}$
- $l_{A2} = 6^{+0.02}_{-0.02}$
- $l_{So,1} = 5^{+0.02}_{-0.02}$
- $l_S = 127.9^{0}_{-0.1}$
- $l_{Be} = 1^{+0.02}_{-0.02}$

An additional clearance $j_5$ of 0.1 mm between the right bearing and socket is included as presented in Figure 51.

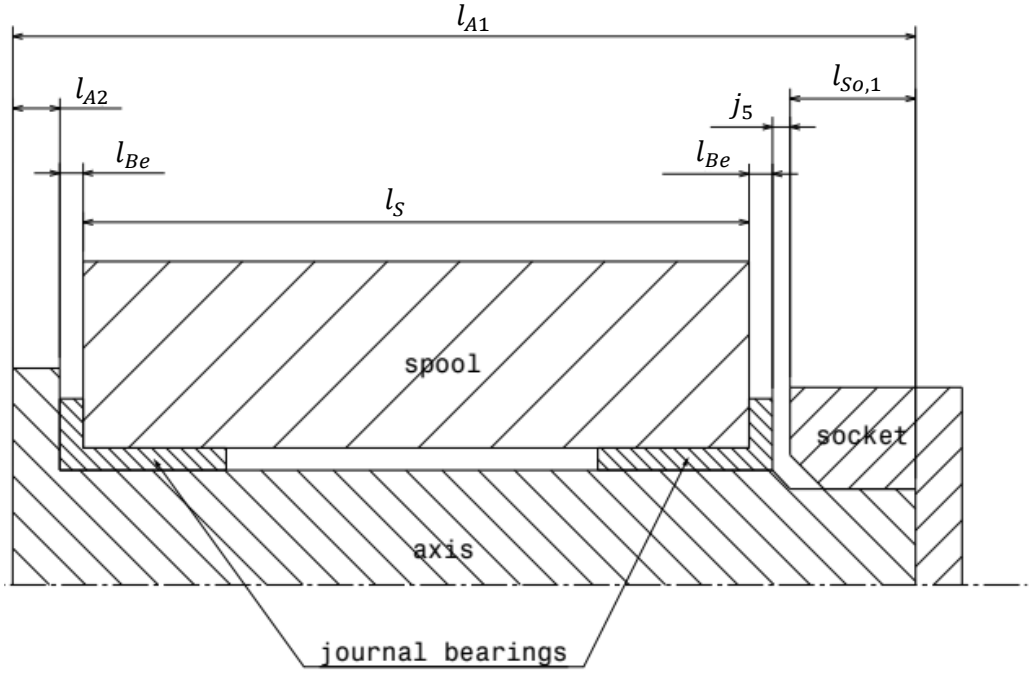


Figure 51: Axial tolerance chain lengths.

The tolerances of the axis, spool, bearing and socket shall not completely eliminate this clearance. Equation (93) shows the minimum clearance which is

$$j_{min} = l_{A1,min} - l_{A2,max} - 2 \cdot l_{Be} - l_{So,1,max} - l_{S,max} = 0.07 \text{ mm} \quad . \tag{93}$$

On the other hand, the spring of the spool brake shall not have contact to the spool shoulder next to the gear as a result of a too large axial travel of the spool. The allowable travel is lower than 1 mm. The maximum travel is given by the clearance of the tolerance chain, which is calculated as

$$j_{max} = l_{A,max} - l_{A2,min} - 2 \cdot l_{Be} - l_{So,1,min} - l_{S,min} = 0.43 \text{ mm} \quad . \tag{94}$$

The maximum gap in axial orientation between these parts is smaller than the required 1 mm. This clearance is acceptable concerning the function of the bearing.

#### 7.3.1.4 Thermo-elasticity analysis of the bearing

The thermal expansion and contraction must be considered for the radial tolerance in the bearing section. The axial position is not investigated in detail because the most material consists of aluminium which results in nearly the same thermal expansion coefficient on each part. The iglidur X bearing material thickness in axial direction is 2 mm. This small value does not change much compared to the clearance values mentioned in Subsection 7.3.1.3.

The aluminium from the axis and spool has a lower thermal expansion coefficient compared to the iglidur X from the bearing. Therefore, the diameters of the bearing increase/decrease faster by changing the temperature than the diameters of the axis and spool. It is assumed that the temperature in the parts varies between -100°C and +100°C and all parts have the same temperature. Thereby, temperature gradients are not considered. It is investigated if the bearing has enough clearance in this temperature range. According to [25] and [26], the thermal expansion coefficient of aluminium varies concerning

different sources between $2.31 \cdot 10^{-5}\ \left[\frac{1}{\mathrm{K}}\right]$ and $2.38 \cdot 10^{-5}\ \left[\frac{1}{\mathrm{K}}\right]$. Therefore, it is set to an average value. The thermal expansion coefficients of aluminium (*Al*) and iglidur X (*IX*) [24] are determined as:

- $\alpha_{T,Al} = 2.34 \cdot 10^{-5}\,\frac{1}{\mathrm{K}}$
- $\alpha_{T,IX} = 5 \cdot 10^{-5}\,\frac{1}{\mathrm{K}}$

Furthermore, the general equation for the thermal expansion/compression is

$$d_{+/-} = d_0 \cdot (1 + \alpha_T \cdot \Delta T) \quad . \tag{95}$$

The initial temperature (no thermo-elastic deformation) considered is 20°C. Therefore, the negative temperature change $\Delta T^-$ is -120 K and the positive $\Delta T^+$ is 80 K. This analysis is made with the minimum clearance to consider the worst-case.

The diameters of the axis $d_{0A}$, spool $d_{0S}$ and bearing $d_{0B,a}$ and $d_{0B,i}$ at 20°C are:

- $d_{0A} = 13.95$ mm
- $d_{0S} = 16.05$ mm
- $d_{0B,a} = 16$ mm
- $d_{0B,i} = 14.016$ mm

The values of these diameters with the thermal influence are

for $\Delta T^+$:

- $d_{A+} = 13.9761$ mm
- $d_{S+} = 16.08$ mm
- $d_{B,a+} = 16.064$ mm
- $d_{B,i+} = 14.0721$ mm

and for $\Delta T^-$:

- $d_{A-} = 13.9108$ mm
- $d_{S}-= 16.0049$ mm
- $d_{B,a-} = 15.904$ mm
- $d_{B,i-} = 13.9319$ mm

As shown in Figure 48, $j_1$ is the clearance between axis and the inner diameter of the journal bearing. The clearance between the outer diameter of the journal bearing and the spool is $j_2$. With the influence of the thermal expansion/compression the values of $j_1$ and $j_2$ are

for $\Delta T^+$:

- $j_{1+} = d_{B,i+} - d_{A+} = 0.096$ mm (96)
- $j_{2+} = d_{S+} - d_{B,a+} = 0.016$ mm (97)

and for $\Delta T^-$:

- $j_{1-} = d_{B,i-} - d_{A-} = 0.0211$ mm (98)
- $j_{2-} = d_{S-} - d_{B,a-} = 0.1009$ mm (99)

The clearances in the thermal expansion and compression are positive, which underlines a well functioned bearing up to 100°C and down to -100°C. Furthermore, the maximum and minimum temperature for the bearing function is determined. If the temperature increases or decreases to a certain point, the iglidur X reaches geometry values of other parts (axis or spool). This is caused by the thermal expansion coefficient of iglidur X which is about two times higher than the one of aluminium. At this point only the redundancy gets lost in the bearing system. One of two sliding surfaces is always intact according to the temperature change. If the redundancy should not get lost ($j_{1,min}$= 0 mm), the maximum negative temperature change $\Delta T^-$ is

$$\Delta T^- = \frac{d_{0B,i} - d_{0A}}{d_{0A} \cdot \alpha_{Al} - d_{0B,i} \cdot \alpha_{T,IX}} = -176.296 \text{ K} \quad . \tag{100}$$

The minimum temperature at which the redundancy of the sliding surfaces is given is -156.296 °C. Additionally, the maximum positive temperature change $\Delta T^+$ for $j_{2,min}$= 0 mm is

$$\Delta T^+ = \frac{d_{0S} - d_{0B,a}}{d_{0B,a} \cdot \alpha_{IX} - d_{0S} \cdot \alpha_{T,Al}} = 117.805\ K \quad . \tag{101}$$

The maximum temperature at which the bearing does not lose its redundancy is 137.805 °C.

### 7.3.2 Spring engaging tolerance

A sufficient engaging depth of the spring shall be ensured.

#### 7.3.2.1 Definition of the tolerance chain

This calculation is used to ensure a defined engaging depth of the spring into the gear which influences the brake forces and the bending stress of the spring. In Figure 52 it is shown that the spring holder is mounted to the socket at its circular ring. The inner diameter of this ring $d_{SH}$ and the outer diameter of the socket $d_{So}$ are:

- $d_{SH} = 23\ H7 = 23_{0}^{+0.021}$
- $d_{So} = 23\ f7 = 23_{-0.041}^{-0.02}$

Furthermore, the distance $l_{SH}$ between the outer spring edge and the central axis of the above-mentioned diameters as well as the spring length $l_{Sp}$ and the outer gear radius $R$ are:

- $l_{SH} = 80.5_{-0.03}^{+0.03}$
- $l_{Sp} = 47_{-0.02}^{+0.02}$
- $R = 35_{-0.1}^{+0.1}$

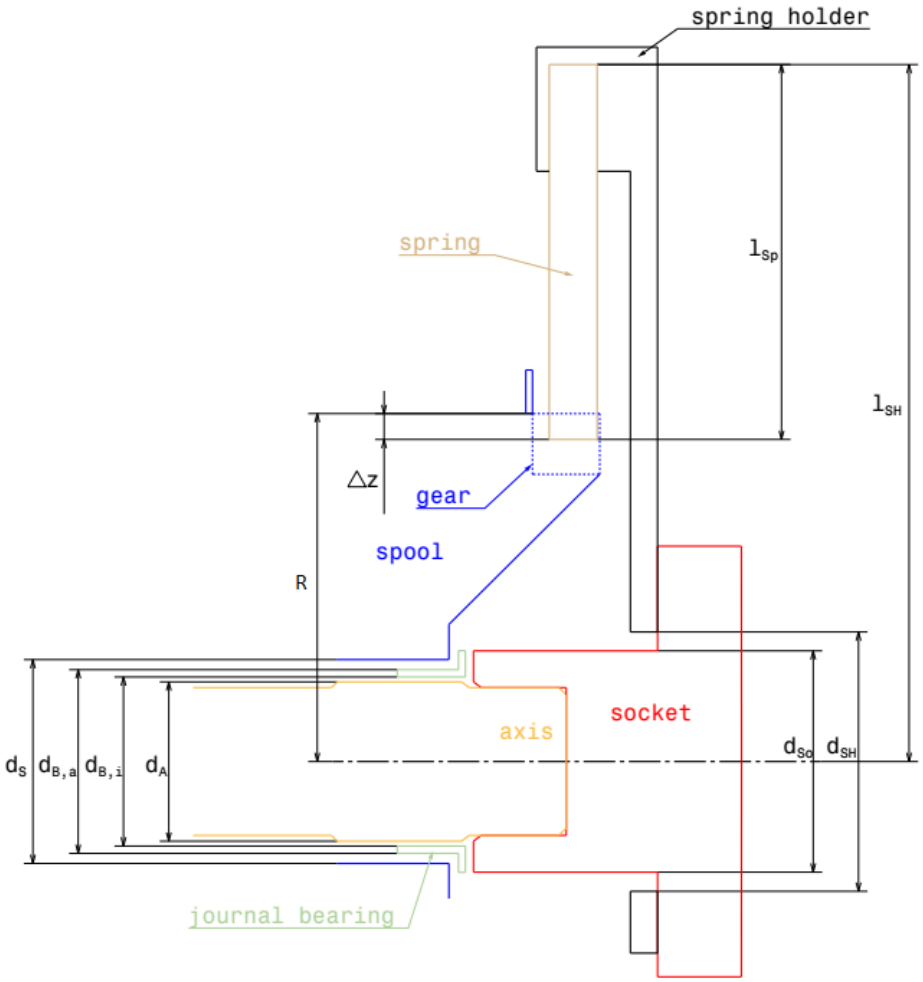


Figure 52: Tolerance chain between socket, spring holder, spring and gear.

With these values of the maximum $\Delta z_{max}$ and minimum $\Delta z_{min}$ engaging depth is calculated by

$$\Delta z_{max} = R_{max} - (l_{SH,min} - l_{Sp,max}) + \frac{d_{SH,max} - d_{So,min}}{2} + \frac{d_{S,max} - d_{B,a,min} + d_{B,i,max} - d_{A,min}}{2} = 1.8385 \text{ mm} \quad , \tag{102}$$

$$\Delta z_{min} = R_{min} - (l_{SH,max} - l_{Sp,min}) - \frac{d_{SH,max} - d_{So,min}}{2} - \frac{d_{S,max} - d_{B,a,min} + d_{B,i,max} - d_{A,min}}{2} = 1.1615 \text{ mm} \quad . \tag{103}$$

In conclusion, the gear engaging depth is

$$\Delta z = 1.5^{+0.3385}_{-0.3385} \text{mm} \quad .$$

The contribution of the spring length tolerances has been investigated for the brake torque estimation but did not have significant influence.

#### 7.3.2.2 Thermo-elastic analysis of the spring engaging tolerance

The geometric changes and the resulting engaging depth of the spring into the gear regarding the thermal expansion is investigated in the following subsection. For this calculation the maximum and minimum engaging depth is used, employing Equations (102) and (103) and the length changes depending on the temperature according to Equation (95). The maximum and minimum engaging depth with thermal influence is calculated by

$$\begin{aligned}\Delta z_{max} &= \left(R_{max} - l_{SH,min}\right) \cdot \left(1 + \alpha_{T,Al} \cdot \Delta T\right) + l_{Sp,max} \cdot \left(1 + \alpha_{T,CuBe} \cdot \Delta T\right) \\ &+ \frac{\left(d_{SH,max} - d_{So,min}\right) \cdot \left(1 + \alpha_{T,Al} \cdot \Delta T\right)}{2} \\ &+ \frac{\left(d_{S,max} - d_{A,min}\right) \cdot \left(1 + \alpha_{T,Al} \cdot \Delta T\right) + \left(d_{B,i,max} - d_{B,a,min}\right) \cdot \left(1 + \alpha_{T,IX} \cdot \Delta T\right)}{2}\end{aligned} \quad (104)$$

$$\begin{aligned}\Delta z_{min} &= \left(R_{min} - l_{SH,max}\right) \cdot \left(1 + \alpha_{T,Al} \cdot \Delta T\right) + l_{Sp,min} \cdot \left(1 + \alpha_{T,CuBe} \cdot \Delta T\right) \\ &- \frac{\left(d_{SH,max} - d_{So,min}\right) \cdot \left(1 + \alpha_{T,Al} \cdot \Delta T\right)}{2} \\ &- \frac{\left(d_{S,max} - d_{A,min}\right) \cdot \left(1 + \alpha_{T,Al} \cdot \Delta T\right) + \left(d_{B,i,max} - d_{B,a,min}\right) \cdot \left(1 + \alpha_{T,IX} \cdot \Delta T\right)}{2}\end{aligned} \quad (105)$$

The same temperature range is used like in the thermal analysis of the bearing in Subsection 7.3.1.4. Therefore, the positive temperature change $\Delta T^+$ is 80 K and the negative $\Delta T^-$ is -120 K. An additional temperature expansion coefficient of the Copper-Beryllium spring $\alpha_{T,CuBe} = 1.75 \cdot 10^{-5}\ \left[\frac{1}{\mathrm{K}}\right]$ [15] is necessary for the calculation. With the influence of the thermal expansion/compression the values of $\Delta z_{max}$ and $\Delta z_{min}$ are

for $\Delta T^+$:

- $\Delta z_{max+} = 1.818$ mm
- $\Delta z_{min+} = 1.144$ mm

and for $\Delta T^-$:

- $\Delta z_{max-} = 1.870$ mm
- $\Delta z_{min-} = 1.188$ mm

To consider the worst-case, the maximum engaging depth of 1.870 mm and the minimum of 1.144 mm is used in further calculations. Both values are used in the Equations from (67) to (85) for the spring torque from Section 7.2.3 to investigate critical torque changes. Table 6 shows the values of the mentioned parameters.

Table 6: Maximum and minimum engaging depth including their influence of the brake torque and the bending stress of the spring.

| Engaging depth [mm] | Minimum torque [Nm] | Maximum torque [Nm] | Required torque [Nm] | Bending stress [MPa] |
|---|---|---|---|---|
| 1.870 | 0.09930 | 0.16416 | 0.10605 | 692.389 |
| 1.144 | 0.06670 | 0.12908 | | 544.432 |

The maximum torque is higher than the required torque which confirms the requirement stated through Equation (67). Therefore, the brake is functioning as expected.

### 7.3.3 Total tolerance of the membrane spool assembly

#### 7.3.3.1 Definition of the tolerance chain

The total tolerance in axial length needs to be known to ensure that the membrane spool can be integrated into the ADEO-2 subsystem. Therefore, three values with their tolerances based on the axis assembly needs to be known. The socked drilling hole depth $l_{So,1}$ as well as the axis length $l_{A1}$ have the same values which are used in Section 7.3.1.3. Figure 53 shows the values for the tolerance chain. The value which is not used before is:

- $l_{So,2} = 14^{+0.1}_{-0.1}$ (ISO 2768 f)

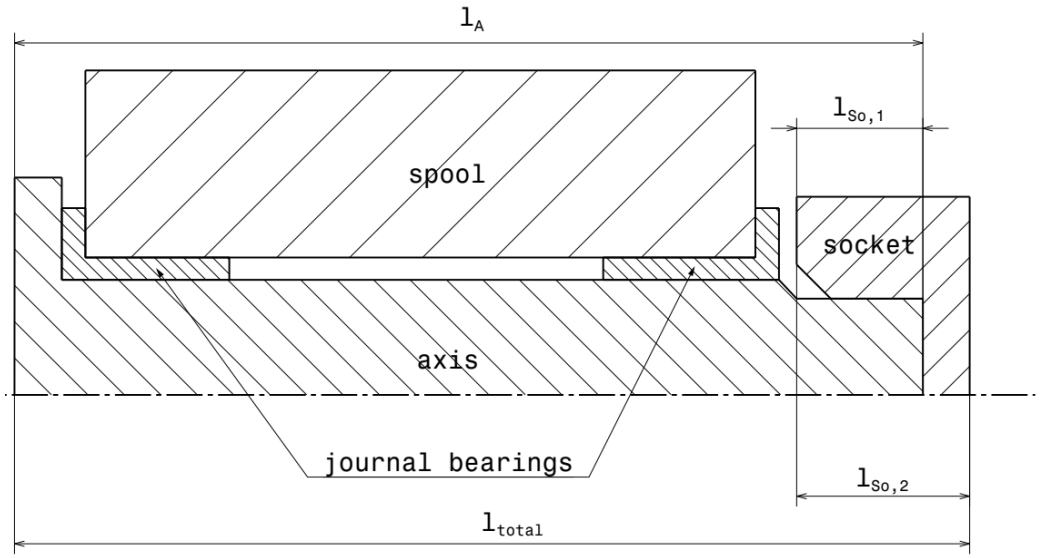


Figure 53: Modell of the membrane spool with all needed values for the total tolerance.

The tolerance chain is

$$l_{total} = l_{A1} + l_{So,2} - l_{So,1} \quad . \tag{106}$$

Additionally, the maximum and minimum membrane spool length is calculated by

$$l_{total,max} = l_{A1,max} + l_{So,2,max} - l_{So,1,min} = 150.27 \text{ mm} \quad , \tag{107}$$

$$l_{total,min} = l_{A1,min} + l_{So,2,min} - l_{So,1,max} = 149.93 \text{ mm} \quad . \tag{108}$$

Finally, the total membrane spool length is

$$l_{total} = 150^{+0.27}_{-0.07} \text{ mm} \quad .$$

#### 7.3.3.2 Thermo-elastic analysis of the total tolerance

The thermal changes influence the total tolerance of the membrane spool. Based on Equation (95), (107) and (108), the maximum length $l_{total,max}$ and minimum length $l_{total,min}$ of the membrane spool is calculated by

$$l_{total,max} = \left(l_{A1,max} + l_{So,2,max} - l_{So,1,min}\right) \cdot (1 + \alpha_{Al} \cdot \Delta T) \quad , \tag{109}$$

$$l_{total,min} = \left(l_{A1,min} + l_{So,2,min} - l_{So,1,max}\right) \cdot (1 + \alpha_{Al} \cdot \Delta T) \quad . \tag{110}$$

The temperature changes $\Delta T^+$ and $\Delta T^-$ and the thermal expansion coefficient $\alpha_{Al}$ are based on the values shown in Subsection 7.3.1.4. The maximum and minimum lengths of the membrane spool assembly are

for $\Delta T^+$:

- $l_{total,max+} = 150.551$ mm
- $l_{total,min+} = 150.211$ mm

and for $\Delta T^-$:

- $l_{total,max-} = 149.848$ mm
- $l_{total,min-} = 149.509$ mm

To consider the worst-case, only the highest and lowest value is used. Therefore, the total length of the membrane spool assembly with thermal influence is

$$l_{total} = 150^{+0.551}_{-0.491} \text{ mm} \quad .$$

These tolerances must be considered in the counterpart design of the ADEO-2 system.

## 7.4 Mass of the membrane spool

According to requirement PFM-DF2 stated in Section 7.1 and a satellite mass of about 500 kg, the maximum mass allowed for the ADEO-2 subsystem is 25 kg. During the preliminary design the maximum spool mass of about 700 g was determined. The mass of the used parts and the total mass of one membrane spool including the membrane segment and interfaces is presented in Table 7.

Table 7: Mass calculation of the membrane spool assembly.

| Part | Amount | Mass [g] per part |
|---|---|---|
| Spool | 1 | 111 |
| Bearing | 2 | 1 |
| Axis | 1 | 46 |
| Socket | 1 | 28 |
| Spring Holder | 1 | 15 |
| Spring | 2 | 1 |
| Spring Holder Plate | 2 | 1 |
| M6x20 | 1 | 10 |
| M3x5 | 5 | 1 |
| Sail + Interface foil | 1 | 110 |
| Total mass | | 331 |

The total mass of the membrane spool assembly is very low compared to the estimated maximum mass. This is achieved by a thin membrane and an Additive Layer Manufacturing of the spool part which reduces the amount of parts and mass. This mass is calculated without the screws which connect the membrane spool to the ADEO-2 system. All in all, the required mass limit is not exceeded.

## 7.5 Eigenfrequency of the ADEO-2 subsystem

For the preliminary design of the ADEO-2 system a modal analysis has been implemented by the company HPS on system level. This analysis included the sail and sail spool design as presented here. The first eigenfrequency is 221 Hz caused by the brake spring. According to (requirement, PFM-DF15), the minimum eigenfrequency shall be 140 Hz or higher. This is important in order to reduce the interaction between the ADEO-2 subsystem and possible launchers. This requirement is confirmed. Furthermore, the spring brake frequency has almost no influence onto the subsystem because of very low mass. The first eigenfrequency which includes more than 10 % effective mass of ADEO-2 is 304 Hz which is more than two times higher compared to the required eigenfrequency. Therefore, sail and spool are also compliant to the system level eigenfrequency requirements.

# 8 Summary and Outlook

In this work, a drag sail design with focus on the membrane and its deployment mechanism is presented. The main goal of a drag sail is to decrease the deorbit time of objects which are flying in LEO like for example disused satellites, bigger space debris parts or upper rocket stages. This is provided by the increasing effective surface area rectangular to the flight direction. This generates a higher drag force. With the higher drag force, the altitude of an object which is flying in LEO is decreasing faster than without drag sail. Such a device can also be used to increase the allowable altitude (at launch) and/or the mass of satellites without increasing the deorbit time, as it is generally agreed on keeping the deorbit time below 25 years. Additionally, the drag sail is a passive deorbit device. After its deployment no further actions are required.

In the ADEO-2 project, a drag sail is designed which should be mounted on the antiram direction of a satellite. According to Section 2, it follows the ADEO-1 project in which a first design was tested on breadboard level. This model was verified in various tests like vibration, shock, thermal vacuum and deployment tests. The results of the designing and testing are used as background knowledge in the ADEO-2 project.

Investigations of the deorbit time and the passive stabilization are presented in Section 3.1 considering the configuration of ADEO-2. The analysis shows that the deorbit process takes about 16 years. This is just a rough estimation because of many simplifications that are made, like considering an average medium solar activity during the deorbit time and a sail that is always rectangular to the flight direction without any tumbling. This calculation was more important in order to evaluate the passive stabilization properties of the satellite with the drag sail. As shown in Section 3.2, the pyramidal shape does not lead to a stabilization of the satellite in altitude above 450 km. This is caused by the low density of the atmosphere and with that a low aerodynamical torque. According to the deorbit characteristic in Section 3.1, the satellite spents nearly the whole deorbit time, except a view months, above the altitude of 450 km. This underlines the design of ADEO-2 which does not have a pitch angle in the sail and therefore a flat membrane surface which is ideally orientated rectangular to the flight direction. When including the tumbling of the satellite, the deorbit time would rise to about 32 years. To decrease this duration the start orbit is limited to a maximum altitude of 728 km presented in Section 3.2 and considering a fixed satellite mass and sail surface.

This work describes the designing of the ADEO-2 membrane and membrane spool. The ADEO-2 subsystem consists of one boom spool, located in the centre, and four membrane spools, positioned around the boom spool, at which the membrane is rolled onto shown in Figure 54. On the boom spool all four booms are coiled. These booms are deployed by a motor and through a boom support guide. The membrane is divided in four segments. Each segment is triangle shaped and folded zig-zag, parallel to the triangle height and is than coiled on one spool shown in Section 5. The segments are connected to the boom via an interface which can transfer deployment and tension loads. Therefore, during the deployment of the boom, which is at the end of the satellite's lifetime, the membrane segments are pulled off the membrane spool. The interfaces are folded and are parallel to the folding lines in the stowed configuration of the ADEO-2. During the deployment of the membrane, the boom – membrane interfaces unfold itself. To ensure an always tensioned sail, the baseline for the interface length, in the deployed version, and with that the design of the sail segment, are the interface lengths in the stowed configuration of ADEO-2 as presented in Section 6.2. The position of the membrane spool in the ADEO-2 accommodation is another baseline which influences the interface lengths in the stowed configuration and thereby the whole sail segment design shown in 6.3. The fully deployed sail is shown in Figure 55.

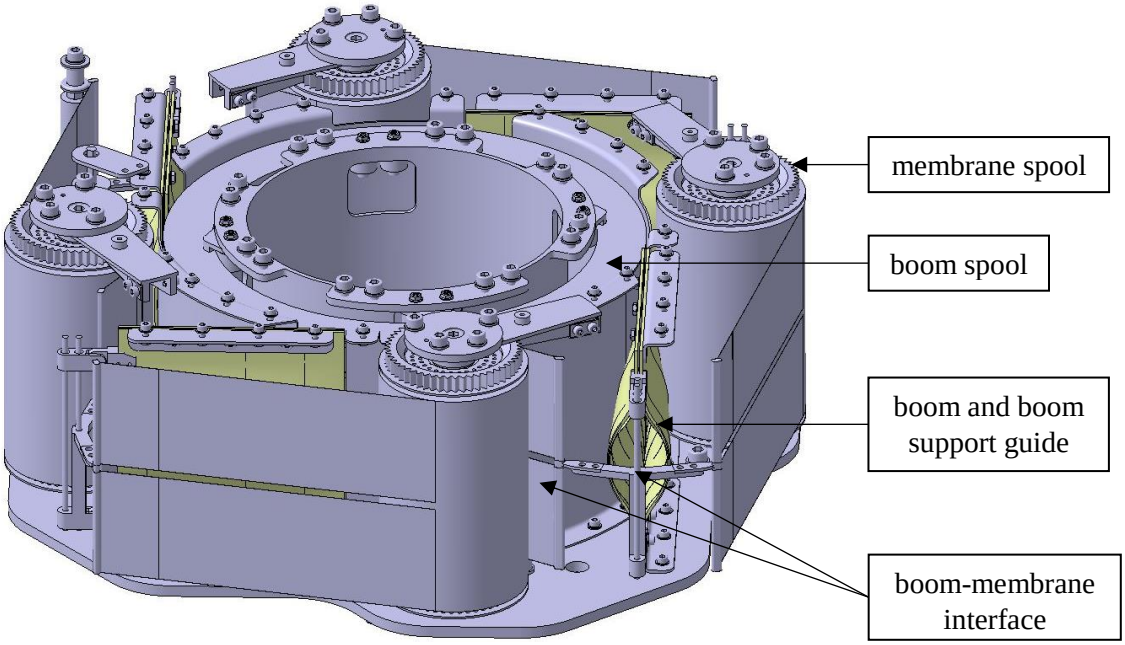


Figure 54: Stowed ADEO-2 configuration without top plate.

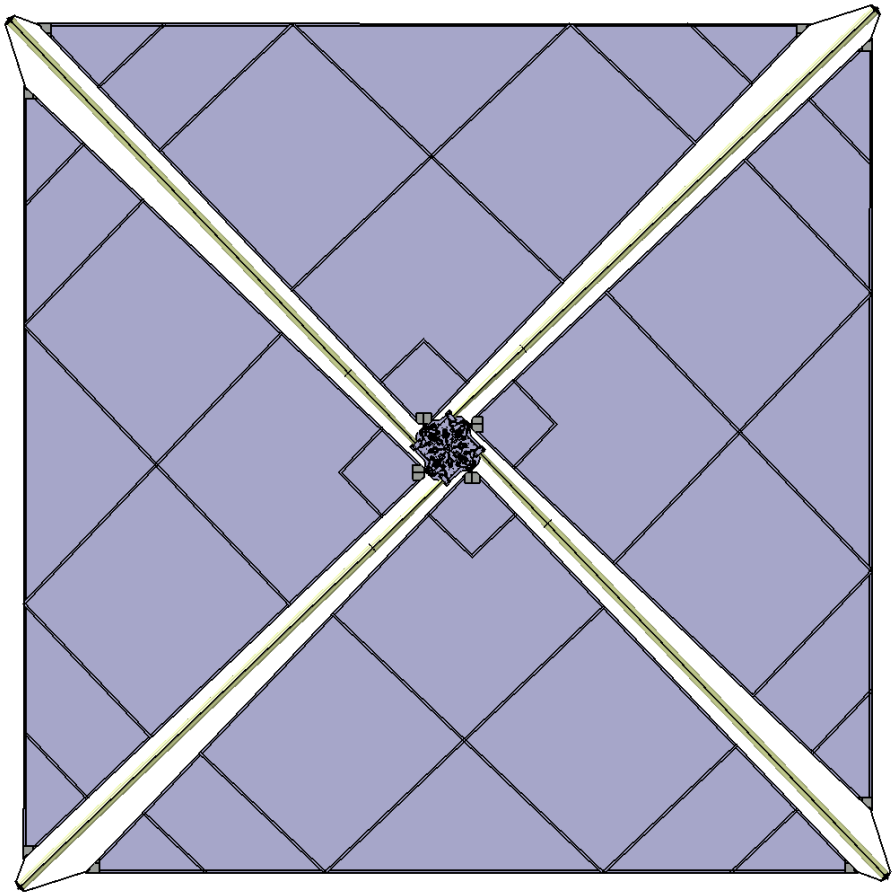

Figure 55: Preliminary ADEO-2 design.

The whole ADEO-2 assembly must withstand the environmental conditions for 15 years in stowed and 25 years in deployed configuration. According to Section 4, the membrane is made of Kapton, a polyimide, with a thickness of 7.6 µm. This polyimide is covered on both sides with a 100 nm thick layer of aluminium. This combination of materials should withstand the ATOX and VUV radiation as

well as the high temperature cycles and range. One membrane segment consists of three membrane stripes, presented in Section 6.3, caused by the manufacturable size of the foil given by the supplier Sheldahl. These stripes are glued together via joining lines which are additional foil stripes with an adhesive underneath. To avoid crack propagation through the whole membrane segment, crack stoppers are used which have the same design as the joining lines. The edges of the membrane segment are reinforced to guarantee that, in case of a crack, the membrane segment does not fall apart. The interfaces between boom and membrane as well as between membrane spool and membrane are made out of the same foil material as the membrane but with a thickness of 76 µm as shown in Section 6.3.

According to Section 7.2, the membrane spools consist of an axis assembly with two parts (axis and socket), screwed together with a M6 screw. Two journal bearings are needed which allow the rotation of the spool part, on which the membrane is coiled onto. The spool part has a gear on one side which is used by the brake assembly and the launch lock. The launch lock blocks the rotation of the spool during lunch and lifetime of the satellite. It will be released at the end of the satellite's lifetime. The brake generates a torque to prevent the membrane from uncoiling and to ensure an always tensioned interface between boom and membrane in the stowed and deployed configuration as well as during the deployment. The brake calculation is made, to investigate the torque, generated by the two copper-beryllium springs. According to Section 7.2.3, the torque is high enough to prevent that the membrane is uncoiling off the spool. Important is the consideration of the bending stress of the spring. The configuration in ADEO-2 prevent high bending forces using two thin springs. The reduction of the spring thickness reduces the bending force and stress in each spring but increases the number of springs to get the required brake torque.

To estimate the size of the spool part, a packaging size calculation is made in Section 7.1. By considering the design and extra thickness of the interfaces, the outer spool diameter was set to 76 mm.

The membrane spool is mainly made of aluminium, except the bearings which are out of iglidur X and the springs which are made of copper-beryllium.

According to Section 7.3, various tolerance chains and thermal investigations are made. As a result, the membrane spool can be used in the given thermal interval which is about +/- 100°C without losing the redundancy of the sliding surfaces of the bearing. The clearances are high enough to guarantee the rotation of the spool part on the axis but not too high which avoids jamming or clamping of parts. Furthermore, the tolerances, caused by manufacturing and thermal expansion/compression, of the engaging depth of the spring into the gear are investigated. This clearance is considered as not critical and without losing the functionality of the brake. A total clearance calculation of the membrane spool is made for the integration of the membrane spool assembly into the ADEO-2 subsystem.

The next step in the ADEO-2 project will be the breadboard design. The described parts of the membrane spool will be mostly produced by external suppliers and integrated in the integration laboratory at DLR in Bremen. The membrane, supplied by Sheldahl, will be cut in the required sizes and bonded together with the joining lines. Additionally, the crack stoppers and reinforced edges will be integrated on the membrane as well as the interfaces. When everything is assembled together and the membrane segments are folded and stowed onto the membrane spools, several tests will be made like deployment tests under atmosphere and in vacuum with thermal influence as well as vibration tests. Furthermore, a life test of the ADEO-2 assembly will be carried out which consists of 14 deployments in a row. After these tests, the detailed design phase will be used to implement small changes which will be noticed during the breadboard test phase. Finally, a proto flight model will be built which is used for a first in-orbit demonstration.

"It is foreseen that the ADEO subsystem will reach TRL 7 by 2019 and through an In-Orbit Demonstration mission TRL 8 in 2019/2020. A first commercial flight of the space proven ADEO could be carried out already in 2020/2021." [8]

Another field of application can be other low orbits around planets with an atmosphere like e.g. Mars. It needs to be further investigated if this sail design can be used for “aerobraking” on other planets but there are limits. The forces cannot be very high caused by the thin membrane and light weight boom structure. The drag sail can cause less fuel consumption and a higher payload mass, but it takes a lot of time.

All in all, the drag sail is a good alternative to deorbit bigger space debris parts like satellites after their lifetime and can decrease the amount of debris flying around the Earth which would make our future space fights safer.

# Appendix

Table 8: Density of the Earth's atmosphere in various altitude for low, moderate (medium) and high solar activity (JB-2006 model). [11, pp. 138-139]

| H (km) | Low activity | Moderate activity | High activity (long term) | High activity (short term) |
|---|---|---|---|---|
| 100 | 5,31E-07 | 5,47E-07 | 5,44E-07 | 5,43E-07 |
| 120 | 2,18E-08 | 2,40E-08 | 2,45E-08 | 2,46E-08 |
| 140 | 3,12E-09 | 3,98E-09 | 4,32E-09 | 4,45E-09 |
| 160 | 9,17E-10 | 1,36E-09 | 1,54E-09 | 1,60E-09 |
| 180 | 3,45E-10 | 6,15E-10 | 7,40E-10 | 7,77E-10 |
| 200 | 1,47E-10 | 3,17E-10 | 4,10E-10 | 4,38E-10 |
| 220 | 6,96E-11 | 1,77E-10 | 2,46E-10 | 2,70E-10 |
| 240 | 3,54E-11 | 1,05E-10 | 1,56E-10 | 1,77E-10 |
| 260 | 1,88E-11 | 6,47E-11 | 1,04E-10 | 1,21E-10 |
| 280 | 1,03E-11 | 4,12E-11 | 7,12E-11 | 8,57E-11 |
| 300 | 5,86E-12 | 2,69E-11 | 5,00E-11 | 6,22E-11 |
| 320 | 3,40E-12 | 1,80E-11 | 3,59E-11 | 4,60E-11 |
| 340 | 2,02E-12 | 1,23E-11 | 2,61E-11 | 3,45E-11 |
| 360 | 1,22E-12 | 8,48E-12 | 1,93E-11 | 2,63E-11 |
| 380 | 7,46E-13 | 5,95E-12 | 1,44E-11 | 2,02E-11 |
| 400 | 4,63E-13 | 4,22E-12 | 1,09E-11 | 1,57E-11 |
| 420 | 2,92E-13 | 3,02E-12 | 8,32E-12 | 1,23E-11 |
| 440 | 1,87E-13 | 2,18E-12 | 6,40E-12 | 9,69E-12 |
| 460 | 1,21E-13 | 1,59E-12 | 4,96E-12 | 7,70E-12 |
| 480 | 8,04E-14 | 1,17E-12 | 3,87E-12 | 6,16E-12 |
| 500 | 5,44E-14 | 8,60E-13 | 3,04E-12 | 4,95E-12 |
| 520 | 3,77E-14 | 6,39E-13 | 2,40E-12 | 4,01E-12 |
| 540 | 2,68E-14 | 4,77E-13 | 1,91E-12 | 3,25E-12 |
| 560 | 1,96E-14 | 3,58E-13 | 1,52E-12 | 2,66E-12 |
| 580 | 1,47E-14 | 2,71E-13 | 1,22E-12 | 2,18E-12 |
| 600 | 1,14E-14 | 2,06E-13 | 9,82E-13 | 1,79E-12 |
| 620 | 9,10E-15 | 1,57E-13 | 7,93E-13 | 1,48E-12 |
| 640 | 7,41E-15 | 1,20E-13 | 6,43E-13 | 1,23E-12 |
| 660 | 6,16E-15 | 9,28E-14 | 5,22E-13 | 1,02E-12 |
| 680 | 5,22E-15 | 7,19E-14 | 4,25E-13 | 8,49E-13 |
| 700 | 4,50E-15 | 5,60E-14 | 3,47E-13 | 7,09E-13 |
| 720 | 3,93E-15 | 4,40E-14 | 2,84E-13 | 5,94E-13 |
| 740 | 3,48E-15 | 3,48E-14 | 2,34E-13 | 4,98E-13 |
| 760 | 3,10E-15 | 2,79E-14 | 1,92E-13 | 4,19E-13 |
| 780 | 2,79E-15 | 2,26E-14 | 1,59E-13 | 3,54E-13 |
| 800 | 2,53E-15 | 1,85E-14 | 1,32E-13 | 2,99E-13 |
| 820 | 2,30E-15 | 1,53E-14 | 1,10E-13 | 2,54E-13 |
| 840 | 2,11E-15 | 1,28E-14 | 9,21E-14 | 2,16E-13 |
| 860 | 1,94E-15 | 1,08E-14 | 7,72E-14 | 1,84E-13 |
| 880 | 1,78E-15 | 9,27E-15 | 6,50E-14 | 1,57E-13 |
| 900 | 1,65E-15 | 8,01E-15 | 5,49E-14 | 1,35E-13 |

NOTE: Low, moderate, high long term and high short term solar and geomagenetic activities have the following meanings:
low ($F10.7 = F10.7_{avg} = 65$, $S10.7 = S10.7_{avg} = 60$, $M10.7 = M10.7_{avg} = 60$, $A_p = 0$)
moderate ($F10.7 = F10.7_{avg} = 140$, $S10.7 = S10.7_{avg} = 125$, $M10.7 = M10.7_{avg} = 125$, $A_p = 15$),
high long term ($F10.7 = F10.7_{avg} = 250$, $S10.7 = S10.7_{avg} = 220$, $M10.7 = M10.7_{avg} = 220$, $A_p = 45$)
high short term ($F10.7 = 300$, $F10.7_{avg} = 250$, $S10.7 = 235$, $S10.7_{avg} = 220$, $M10.7 = 240$, $M10.7_{avg} = 220$, $A_p = 240$)

# Literature


[1] ESA, space debris, Internet page: http://www.esa.int/Our_Activities/Operations/Space_Debris/Space_debris_by_the_numbers, (10.02.2019)

[2] Surrey Space Centre, RemoveDEBRIS, Internet page: https://www.surrey.ac.uk/surrey-space-centre/missions/removedebris, (04.03.2019)

[3] Lappas, V.; Adeli, N.; Visagie, L.; Fernandez, J.; Theodorou, T.; Steyn, W.; Peren, M.: "CubeSail: A low cost CubeSat base solar sail demonstration mission", Advances in Space Research 48.11: 1890-1901 (2011)

[4] eoPortalDirectory, NanoSail-D, Internet page: https://directory.eoportal.org/web/eoportal/satellite-missions/n/nanosail-d, (05.03.2019)

[5] The Planet Society, LightSail, Internet page: http://www.planetary.org/explore/projects/lightsail-solar-sailing/, (05.03.2019)

[6] Seefeldt, P.; Spietz, P.; Sproewitz, T. et al.: "Gossamer-1: Mission concept and technology for a controlled deployment of gossamer spacecraft", Advances in Space Research 59.1: 434-456, (2017)

[7] Sinn, T.; Seefeldt, P.; Riemer, A. et al.: "DESIGN, ANALYSIS AND TESTING OF THE ADEO PASSIVE DE-ORBIT SUBSYSTEM DEMONSTRATOR", 14th European Conference on Spacecraft Structures, Materials and Environmental Testing (ECSSMET) (2016)

[8] Sinn, T.; Tiedemann, L.; Riemer, A. et al.: "RESULTS OF THE DEPLOYABLE MEMBRANE & ADEO PASSIVE DE-ORBIT SUBSYSTEM ACTIVITIES LEADING TO A DRAGSAIL DEMONSTRATOR", 7th European Conference on Space Debris (2017)

[9] Griffin, M. D.; Feldhusen, J.: "Space Vehicle Design", American Institute of Aeronautics and Astronautics, Second Edition (2004)

[10] Larson, Wiley J.; Wertz, James R.: "Space Mission Analysis and Design", Space Technology Series, Second Edition (1998)

[11] ESA-ESTEC, ECSS-E-ST-10-04C, (status: 15.11.2008)

[12] Fortescue, P.; Stark, J.; Swinerd, G.: "Spacecraft Systems Engineering", Wiley, Third Edition (2003)

[13] Wikipedia, Solar cycle, Internet page: https://en.wikipedia.org/wiki/Solar_cycle, (15.05.2019)

[14] Seefeldt, P.: "Entwicklung eines Widerstandssegels zur Vermeidung von Raumfahrtrückstanden in niedrigen Erdorbits" (2010)

[15] Materion, Datasheet: Alloy 25 (C17200) Plate, Internet page: https://materion.com/-/media/files/alloy/datasheets/copperberyllium/ad0104_1011-alloy-25-_c17200_-plate.pdf, (26.02.2019)

[16] Seefeldt, P.; Braxmaier, C.; Rittweger, A.: "Development and Qualification of Deployable Membranes for Space Applications", Diss. Universität Bremen (2018)

[17] Martinez, I., "Radiative view factors.", Internet page: http://webserver.dmt.upm.es/~isidoro/tc3/Radiation%20View%20factors.pdf, (06.03.2019)

[18] Sheldahl, RedBook, Internet page: http://www.sheldahl.com/sites/default/files/Documents/ShieldingMaterials/RedBook.pdf, (05.03.2019)

[19] Wikipedia, Outer space, Internet page: https://en.wikipedia.org/wiki/Outer_space, (15.05.2019)

[20] Sinn, T.: “ADEO2-HPS-TN-1130_2_ADEO2 PFM Requirements”, (12.11.2018)

[21] Banks, B. A.; Backus, J. A.; Manno, M. V.; et al.:"Atomic oxygen erosion yield prediction for spacecraft polymers in low earth orbit" (2009)

[22] de Rooij, A.: "Corrosion in space." Encyclopedia of Aerospace Engineering: 1-15 (2010)

[23] maschinenbau-fh, Flächenträgheitsmoment und Widerstandsmoment eines Rechtecks berechnen, Internetpage: http://www.maschinenbau-fh.de/f_i_w_rechteck_berechnen.html, (08.04.2019)

[24] Igus, iglidur X, Internetpage: https://www.igus.de/product/72, (08.04.2019)

[25] Wikipedia, Aluminium, Internet page: https://de.wikipedia.org/wiki/Aluminium, (30.04.2019)

[26] Burde & Co., Wärmeausdehnung, Internet page: https://www.burdeco.com/wp-content/uploads/2015/10/waermeausdehnung.pdf, (30.04.2019)